Aus dem **Institut für Laboratoriumsmedizin**
Klinikum der Universität München
Direktor: Univ.-Prof. Dr. med. Daniel Teupser

und dem **Laser-Forschungslabor**
Klinikum der Universität München
Leiter: Dr. rer. biol. hum. Ronald Sroka

Fluoreszenz von Porphyrinen zur klinischen Anwendung in Diagnostik und Therapie

Dissertation
zum Erwerb des Doktorgrades der Humanbiologie
an der Medizinischen Fakultät der
Ludwig-Maximilians-Universität München

vorgelegt von
Georg Hennig
aus München
2014

Mit Genehmigung der Medizinischen Fakultät
der Ludwig-Maximilians-Universität München

Berichterstatter:	Prof. Dr. med. Michael Vogeser
Mitberichterstatter:	Prof. Dr. med. Christian G. Chaussy Priv.-Doz. Dr. med. Thomas Herzinger apl. Prof. Dr. med. Andreas Leunig
Mitbetreuung durch den promovierten Mitarbeiter:	Dr. rer. biol. hum. Herbert Stepp
Dekan:	Prof. Dr. med. Dr. h. c. Maximilian Reiser, FACR, FRCR

Tag der mündlichen Prüfung: 27.03.2014

für Ann

* 15.10.1979 † 14.08.2011

INHALTSVERZEICHNIS

Inhaltsverzeichnis **5**
Abstract **7**
Zusammenfassung **9**
Fluoreszenzspektroskopischer Nachweis von Porphyrinen **11**
Vorkommen und Funktion 11
Spektroskopische Eigenschaften 13
Klinischer Nachweis 14
Stand der Technik 14
Nichtinvasiver Nachweis von Zink-Protoporphyrin IX 14
Medizinische Aspekte und Grundlagen 14
Lichtausbreitung in Gewebe 15
Quantitativer Nachweis von Zink-Protoporphyrin IX in Blut 17
Ausblick auf nichtinvasive Messungen 19
Photodynamische Wirkung 19
Grundlagen 19
Photodynamische Therapie 19
Literatur 21
Originalmanuskripte **27**
Comparison of an accelerated weighted fluorescence Monte Carlo simulation method with reference methods in multi-layered turbid media 29
Bandwidth-variable tunable optical filter unit for illumination and spectral imaging systems using thin-film optical band-pass filters 41
Dual-wavelength excitation for fluorescence-based quantification of zinc protoporphyrin IX and protoporphyrin IX in whole blood 51
Photobleaching-based method to individualize irradiation time during interstitial 5-aminolevulinic acid photodynamic therapy 65
Danksagung **75**

Abstract

Porphyrins are vital components of every cell in the human body. Within erythrocytes, heme, iron protoporphyrin IX, in hemoglobin serves as oxygen carrier. A variety of inherited and acquired disorders of heme synthesis alter protoporphyrin IX (PPIX) concentrations in erythrocytes. Accordingly, quantitation of PPIX may aid in the diagnostic evaluation of these conditions. If iron delivery during erythropoiesis is restricted, in the last step of heme synthesis, a zinc ion may be chelated by PPIX instead of an iron ion, increasing the concentration of zinc protoporphyrin IX (ZnPP) within the erythrocyte. Because a lack of iron is the most common cause of restricted iron delivery, an elevated erythrocyte ZnPP may serve as a diagnostic indicator of iron deficiency. Unlike heme, PPIX and ZnPP are fluorescent and can be quantified by fluorescence spectroscopy. In measurements on whole blood, plasma background fluorescence interferes with porphyrin fluorescence signals. As a consequence, previous methods for erythrocyte fluorescence studies have required washing blood samples to remove plasma fluorophores before measurement.

For fluorescence spectroscopic studies, an optical instrument was designed [2] that made possible illumination of blood samples by light with a small spectral bandwidth (< 5 nm FWHM) at high intensity in the range 395 nm to 431 nm [3]. The remitted fluorescence light is measured spectrally resolved. Using this instrument, a method was developed and validated to eliminate background plasma fluorescence while retaining the characteristic fluorescence peaks of ZnPP and PPIX. The method calculates the difference between fluorescence spectra upon excitation at two different wavelengths [3]. Porphyrin concentrations are determined quantitatively in whole blood from the porphyrin fluorescence peaks, independently from the interfering background fluorescence [3].

A future clinical study aims to determine if ZnPP in erythrocytes can be quantified by noninvasive fluorescence spectroscopic measurements of oral mucosa. Critical difficulties for such noninvasive measurements include strong tissue autofluorescence and the varying optical properties and inhomogeneous, layered structure of mucosal tissue. The proposed method using two different excitation wavelengths [3] will be applied to largely eliminate the autofluorescence. For theoretical investigations of possible limitations of the proposed method applied to measurements of oral mucosa, a Monte Carlo simulation method was developed to calculate the distribution of fluorescence light in layered scattering media [1].

In addition to the diagnostic applications of quantitation of erythrocyte PPIX and ZnPP, a potential therapeutic application of PPIX fluorescence monitoring in tumor cells was developed. In photodynamic therapy (PDT) of malignant gliomas, PPIX accumulates in the brain tumor after treatment with 5-aminolevulinic acid. After illumination, the PPIX-induced phototoxic effect kills tumor cells. A limitation in the effective use of photodynamic therapy has been determination of the time required for photobleaching of the accumulated PPIX in the entire tumor volume. Fluorescence measurements to monitor therapy can be performed only with use of the implanted treatment optical fibers. Therefore, a method to monitor the progress of treatment was developed and validated by means of computer simulations. This method is based on the PPIX fluorescence recorded during treatment and can be applied even with a restricted number of measurement fibers and without knowledge of the optical properties of the tumor tissue [4].

ZUSAMMENFASSUNG

Porphyrine spielen eine wichtige Rolle im menschlichen Organismus. Häm, das Eisen-Protoporphyrin IX, dient an Hämoglobin gebunden in Erythrozyten als Sauerstofftransporter. Angeborene oder erworbene Störungen der Hämsynthese können zu einer erhöhten Konzentration von Protoporphyrin IX (PPIX) in den Erythrozyten führen. Eine Messung der PPIX-Konzentration kann also bei der Diagnose einer derartigen Störung helfen. Eine erhöhte Konzentration von Zink-Protoporphyrin IX (ZnPP) in Erythrozyten wird beobachtet, wenn wegen begrenzter Verfügbarkeit von Eisen während der Erythropoiese im letzten Schritt der Hämsynthese statt des Eisenions ein Zinkion in das PPIX eingebaut wird. Eine begrenzte Verfügbarkeit von Eisen liegt vor allem bei Eisenmangel vor, so dass ZnPP als diagnostischer Marker für den Eisenmangelnachweis dienen kann. Im Gegensatz zu Häm zeigen ZnPP und PPIX Fluoreszenz, so dass diese Substanzen über fluoreszenzspektroskopische Methoden quantifiziert werden können. Bei Messungen an Vollblut beeinträchtigt allerdings die Untergrundfluoreszenz des Blutplasmas die Messung der Porphyrinfluoreszenz. Daher mussten die Blutproben bisher für fluoreszenzspektroskopische Untersuchungen gewaschen werden, um die Fluorophore im Blutplasma zu entfernen.

Für fluoreszenzspektroskopische Untersuchungen an Vollblut wurde ein Aufbau erstellt [2], der es erlaubt, Blutproben mit Licht geringer spektraler Breite (< 5 nm FWHM) bei hoher Intensität im Bereich 395 nm bis 431 nm zu beleuchten und das remittierte Fluoreszenzlicht spektral aufgelöst zu messen [3]. Es wurde eine Methode vorgeschlagen und mit diesem Aufbau validiert, mittels Berechnung der Differenz von Fluoreszenzspektren bei Anregung mit zwei verschiedenen Wellenlängen die Untergrundfluoreszenz zu eliminieren, während die charakteristischen Porphyrinfluoreszenzmaxima von ZnPP und PPIX erhalten bleiben [3]. Diese Fluoreszenzmaxima erlauben eine quantitative Aussage über die Porphyrinkonzentrationen in Vollblut, unbeeinflusst von störender Untergrundfluoreszenz [3].

In einer klinischen Studie soll zudem gezeigt werden, dass nichtinvasive fluoreszenzspektroskopische Messungen an oraler Mucosa geeignet sind, ZnPP in Erythrozyten quantitativ nachzuweisen. Die größten Probleme stellen die intensive Gewebeautofluoreszenz und die stark variierenden optischen Gewebeparameter, sowie dessen inhomogener, geschichteter Aufbau dar. Die Autofluoreszenz soll mit der vorgestellten Methode durch Anregung mit zwei verschiedenen Wellenlängen [3] rechnerisch weitgehend eliminiert werden. Um mögliche Hürden in der Anwendung dieser Methode an der oralen Mucosa theoretisch untersuchen zu können, wurde ein Verfahren entwickelt, mittels Monte-Carlo-Simulationen die Ausbreitung von Fluoreszenzlicht in geschichteten, streuenden Medien zu berechnen [1].

Neben diesen diagnostischen Anwendungen der Quantifizierung von PPIX und ZnPP in Erythrozyten wurde die PPIX-Fluoreszenzmessung an Tumorzellen auch als mögliches Instrument zum Monitoring einer therapeutischen Anwendung untersucht. Bei der photodynamischen Therapie (PDT) maligner Gliome reichert sich nach Applikation von 5-Aminolävulinsäure PPIX im Gehirntumor an, so dass mittels Beleuchtung der durch das PPIX induzierte phototoxische Effekt genutzt werden kann, um die Tumorzellen abzutöten. Ein Problem ist dabei die Bestimmung der Zeit, nach der das PPIX im gesamten Tumorvolumen ausgeblichen wurde. Allerdings stehen zur Messung nur die für die Therapie implantierten Lichtleiter zur Verfügung. Daher wurde eine Methode entwickelt und anhand von Simulationsrechnungen validiert, mit der trotz der eingeschränkten Anzahl an Messfasern und trotz der unbekannten optischen Eigenschaften des Tumorgewebes anhand der PPIX-Fluoreszenz der Behandlungsfortschritt überprüft werden könnte [4].

Fluoreszenzspektroskopischer Nachweis von Porphyrinen

Diese Dissertation wird in kumulativer Form eingereicht und besteht aus vier Originalmanuskripten [1-4]. Diese Manuskripte beschäftigen sich mit theoretischen Grundlagen und klinischen Anwendungen des fluoreszenzspektroskopischen Nachweises von Porphyrinen. Im Bereich der Diagnostik wurden Wege und Werkzeuge aufgezeigt, um Zink-Protoporphyrin IX (ZnPP) und Protoporphyrin IX (PPIX) im Blut unbeeinflusst von störender Untergrundfluoreszenz quantitativ nachzuweisen mit dem Ziel der nichtinvasiven Quantifizierung dieser Porphyrine an oraler Mucosa. Im Bereich der Therapie wurde ein Dosimetriekonzept für die interstitielle photodynamische Therapie (PDT) bei Glioblastomen vorgeschlagen, das die Fluoreszenz des mittels 5-Aminolävulinsäure induzierten PPIX zur Vorhersage des bereits ausgeblichenen Anteils PPIX während der Behandlung nutzt.

Vorkommen und Funktion

Porphyrine sind organische Moleküle und Farbstoffe, die aus vier zyklisch verbundenen Pyrrolringen zusammengesetzt sind (Tetrapyrrol) [9,10]. Sie spielen in Organismen eine wichtige Rolle. Der Komplex aus zweiwertigem Eisen (Fe^{2+}) und Protoporphyrin IX (PPIX) [10,11] wird als Häm bezeichnet, siehe Abbildung 1. Häm kommt im menschlichen Körper beispielsweise im Hämoglobin, Myoglobin, Neuroglobin, Cytoglobin und in Cytochromen vor [12,13]. Es dient proteingebunden als Sauerstofftransporter [9,10] und -speicher [10] (Hämoglobin in Erythrozyten und Myoglobin in Muskelzellen) oder fungiert als Elektronenüberträger in der Atmungskette (Cytochrome) [9]. Chlorophyll, ein weiteres Tetrapyrrol, jedoch mit zentralem Magnesiumion, dient den Pflanzen als Farbstoff, der durch Absorption von Photonen des Sonnenlichts die Photosynthese ermöglicht [9,14].

Hämoglobin, der rote Blutfarbstoff, besteht aus vier Globinketten, also vier globulären Polypeptidketten, an die je ein Hämmolekül gebunden ist [10]. Diese Bindung sorgt dafür, dass das Häm in der Lunge bei dem dort herrschenden hohen Sauerstoffpartialdruck Sauerstoffmoleküle nicht nur binden, sondern an Orten mit großem Sauerstoffbedarf bei geringerem Sauerstoffpartialdruck auch wieder abgeben kann [15]. In Muskelzellen wird der Sauerstoff an Myoglobin gebunden, weil dieses bei gleichem Sauerstoffpartialdruck eine höhere Sauerstoffaffinität als das Hämoglobin besitzt [15]. Das Hämoglobin erhöht also die Fähigkeit von Blut, Sauerstoff zu transportieren, über die physikalische Löslichkeit von Sauerstoff in Wasser hinaus.

Häm wird grundsätzlich in einer Vielzahl von Körperzellen synthetisiert [14,16], insbesondere im Knochenmark, wo die Bildung der Erythrozyten, die Erythropoiese, stattfindet [16]. Erythrozyten enthalten physiologisch je 28–33 pg Hämoglobinmoleküle [11], und insgesamt über 80% der im Körper vorkommenden Hämmoleküle [16]. Die Synthese von Häm ist in Abbildung 1 schematisch dargestellt. Aus dem Grundbaustein 5-Aminolävulinsäure (5-ALA) wird über mehrere enzymatisch regulierte Zwischenschritte PPIX gebildet. Dabei finden die in Abbildung 1 dargestellten Prozesse in den Mitochondrien statt, die ausgelassenen Zwischenschritte allerdings im Cytoplasma [9]. Durch das Enzym Ferrochelatase wird im letzten Schritt aus PPIX und Fe^{2+} das Häm gebildet. Wie in Abbildung 1 ebenfalls gezeigt ist, ist Häm nicht das einzige Porphyrin, das unter physiologischen Bedingungen in Erythrozyten vorkommt: Zink-Protoporphyrin IX (ZnPP) entsteht in Spuren im letzten Schritt der Hämsynthese, in dem katalysiert durch die Ferrochelatase [17] zweiwertiges Zink (Zn^{2+}) anstelle des Eisenions in das PPIX eingebaut wird. Das Verhältnis der ZnPP-Konzentration zur Hämkonzentration im Erythrozyten beträgt physiologisch etwa $5 \cdot 10^{-5}$, und das von PPIX ohne zentrales Metallion zu Häm etwa $5 \cdot 10^{-6}$ [3,17-19]. Eine typische absolute Anzahl Moleküle in Erythrozyten ist in Abbildung 1 ebenfalls angegeben. Die

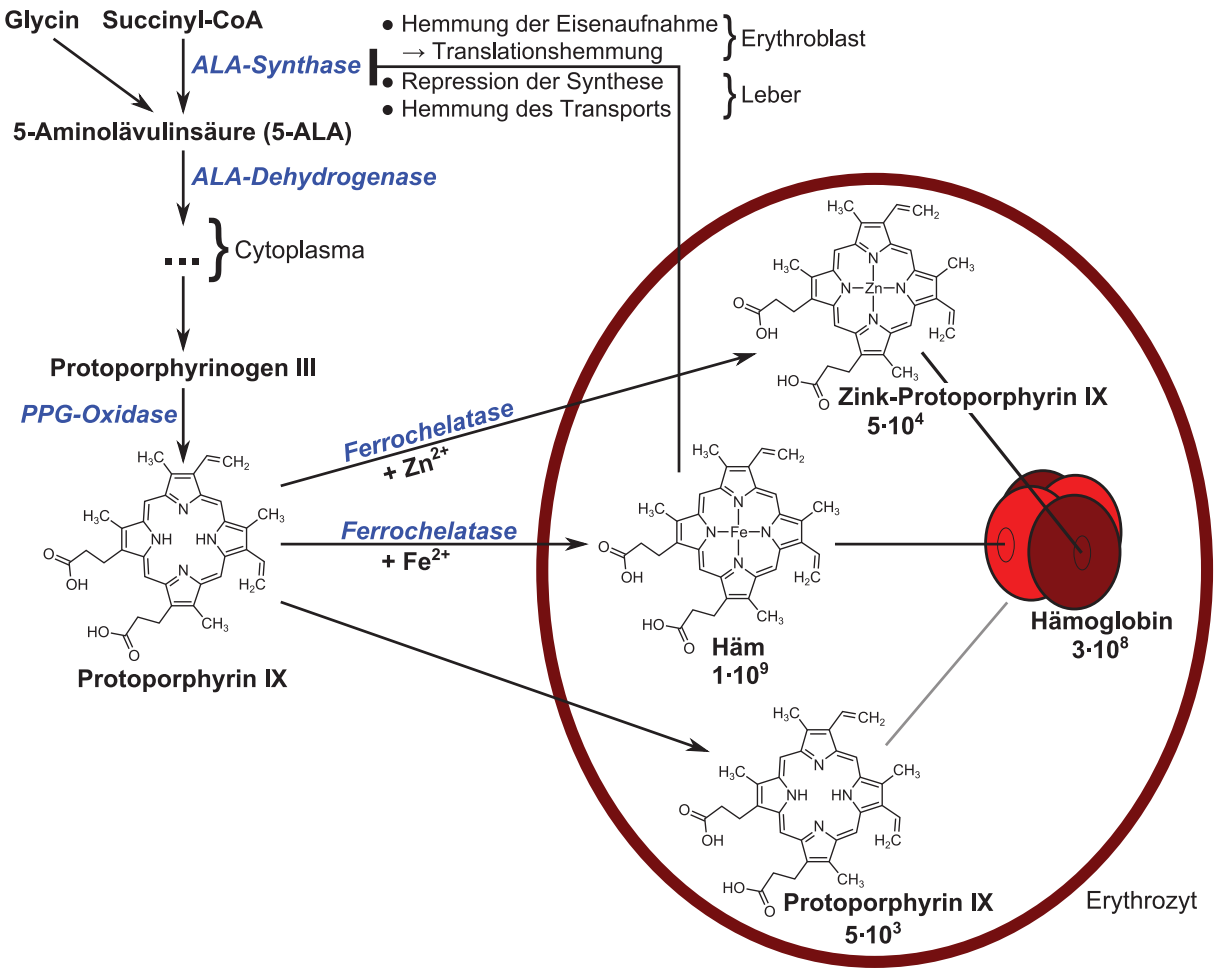

Abbildung 1. Schematische Darstellung der Häm-Synthese nach [9,17]. Enzyme sind in kursiver blauer Schrift hervorgehoben. Die Angabe der Anzahl Moleküle Häm, ZnPP und PPIX pro Erythrozyt wurden aus dem physiologischen Wert 28–33 pg Hämoglobin pro Erythrozyt [11], der molaren Masse von Hämoglobin 64,458 g/mol [25], sowie den physiologischen Werten von 50 µmol ZnPP/mol Häm und 5 µmol PPIX/mol Häm [17] berechnet.

Bindungsstelle von ZnPP an das Hämoglobinmolekül ist nicht eindeutig aufgeklärt. Es bindet entweder in dessen Bindungstaschen [20,21] oder außerhalb derselben [22]. Das „freie" PPIX ist offenbar außerhalb der Bindungstaschen an das Hämoglobinmolekül gebunden [20] und kann aus den Erythrozyten mit der Zeit ausdiffundieren [23,24].

Eine Störung der Porphyrin- und Hämsynthese durch gestörte enzymatische Aktivität in einem der Hämsyntheseschritte wird als Porphyrie bezeichnet und äußert sich häufig in der Anreicherung verschiedener Hämvorstufen [9,14]. Je nach Ort der klinischen Hauptmanifestation, nämlich Leber oder Erythrozyten, spricht man von einer hepatischen oder einer erythropoetischen Porphyrie [9]. Die hepatischen Porphyrien können in akute und chronische Porphyrien eingeteilt werden, während die erythropoetischen Porphyrien chronisch verlaufen [9]. Der klinische Nachweis erfolgt über Porphyrinvorstufen und Porphyrine in Stuhl, Urin, Plasma oder Erythrozyten [14]. Die klinisch häufigsten Porphyrien sind die *porphyria cutanea tarda* (PCT), die akute intermittierende Porphyrie (AIP) und die erythropoetische Protoporphyrie (EPP) [14].

Erhöhtes ZnPP in den Erythrozyten findet man vor allem bei sekundären Protoporphyrinämien [14], bei denen statt Fe^{2+} ersatzweise Zn^{2+} in das PPIX eingebaut wird [3,17]. Dieser ersatzweise Einbau von Zn^{2+} anstelle von Fe^{2+} findet sich insbesondere bei persistierendem Eisenmangel, chronisch entzündlichen Erkrankungen und chronischer Bleivergiftung [17]. Eine erniedrigte ZnPP-Konzentration in Erythrozyten kann ein Hinweis auf Eisenüberladung wie hereditäre Hämochromatose sein [17,26]. In Erythrozyten findet man eine PPIX-Anreicherung insbesondere bei der erythropoetischen Protoporphyrie [14,18,27], bei der der enzymatische Einbau

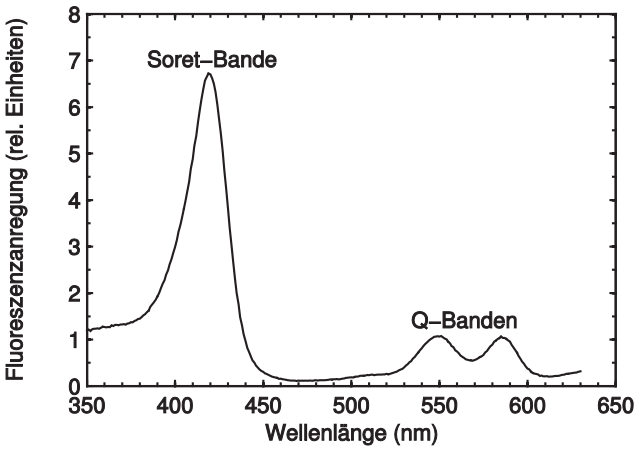

Abbildung 2. Anregungseffizienz von Zink-Protoporphyrin IX bei Emission bei 640 nm, 2 µM ZnPP gelöst in NaOH unter Zugabe von FKS.

von Eisen in das PPIX gestört ist [3,14,27]. Beim Nachweis der Porphyrinkonzentrationen in Erythrozyten ist zu beachten, dass die mittlere Lebensdauer von Erythrozyten 120 Tage beträgt [11], weshalb eine Messung der mittleren Porphyrinkonzentrationen aller Erythrozyten nicht den Zustand widerspiegeln muss, unter dem die Erythrozyten zum Zeitpunkt der Messung gebildet werden.

Die Neubildung von Häm wird unter physiologischen Bedingungen durch das Häm selbst gehemmt [9]. Dabei ist die Bildung von 5-ALA der ratenlimitierende Prozess bei der Hämsynthese [28]. Wird zu diagnostischem oder therapeutischem Zweck 5-ALA appliziert, wird diese negative Rückkopplung umgangen. In diesem Fall ist der Einbau von Fe^{2+} wegen des Überangebots von 5-ALA der ratenlimitierende Prozess und es entsteht verstärkt PPIX, welches sich in den Zellen anreichert [28]. Dieser Weg wird bei der Photodynamischen Therapie und Fluoreszenzdiagnostik mit 5-ALA benutzt, um Tumorzellen mit PPIX anzureichern und dessen Phototoxizität und Fluoreszenz zu nutzen [28].

Der Abbau von Hämoglobin erfolgt nach Phagozytose der Erythrozyten vor allem in Milz und Leber [11]. Das Eisenion des Hämmoleküls wird oxidiert, an Ferritin gebunden und größtenteils wieder der Hämsynthese zugeführt [11]. Das verbleibende Porphyrin wird über Biliverdin in wasserunlösliches Bilirubin umgewandelt [11]. Das Bilirubin wiederum wird an Albumin gebunden, in der Leber mit Glucuronsäure konjugiert und über die Galle ausgeschieden [11].

Spektroskopische Eigenschaften

Porphyrine weisen im Allgemeinen eine elektronische Absorptionsbande im blauen Spektralbereich auf, die Soret-Bande [29]. Die genaue spektrale Position hängt von der Art des Porphyrins und beispielsweise der chemischen Umgebung wie dem pH-Wert ab [29-31]. Daneben existieren Absorptionsbanden bei niedrigerer Energie und damit größerer Wellenlänge im grünen, gelben oder roten Spektralbereich, die Q-Banden [29]. Abbildung 2 zeigt beispielhaft die wellenlängenabhängige Anregungseffizienz von ZnPP bei Fluoreszenzemission um 640 nm, gelöst in NaOH, zur Nachbildung der Proteinbindung unter Zugabe von FKS (fetales Kälberserum). Die Soret-Bande liegt hier bei 419 nm, die Q-Banden bei 549 nm und 585 nm. Bei oxygeniertem Hämoglobin liegt die Soret-Bande bei 415 nm, die Q-Banden bei 541 nm und 576 nm [32].

Ein wesentlicher fluoreszenzspektroskopischer Unterschied zwischen Häm, dem Eisen-Protoporphyrin IX, und Zink-Protoporphyrin IX ist das Auftreten von starker Fluoreszenz beim ZnPP, während Häm keine Fluoreszenz zeigt [33,34]. Grundsätzlich erhöhen schwere Zentralatome bei Porphyrinen die Rate für Übergänge vom angeregten Singulettzustand in den Triplettzustand (Intersytem Crossing) beim sogenannten Schweratomeffekt [35,36], so dass gleichzeitig die Wahrscheinlichkeit für das Auftreten von Fluoreszenz sinkt [36,37]. Dagegen ist die be-

obachtbare Fluoreszenzauslöschung beim Häm gegenüber dem Auftreten von Fluoreszenz beim ZnPP in erster Linie auf die unterschiedliche Elektronenkonfiguration der zentralen Metallionen zurückzuführen. Zweiwertiges Zink (Zn^{2+}) besitzt eine volle d-Schale (Elektronenkonfiguration [Ar] $3d^{10}$), während bei zweiwertigem Eisen (Fe^{2+}) die d-Schale nicht vollständig besetzt ist (Elektronenkonfiguration [Ar] $3d^{6}$) [38]. Die ungepaarten Elektronen im Eisenion führen dabei zu einer deutlich erhöhten Rate für das Auftreten von Intersystem Crossing, was die Fluoreszenzauslöschung verursacht [36,37]. Bei Porphyrinen mit zentralen Metallionen mit abgeschlossener Elektronenschale wie beim ZnPP wird dagegen starke Fluoreszenz beobachtet [36].

Klinischer Nachweis

Stand der Technik

Der Häm- bzw. Hämoglobingehalt des Blutes wird heutzutage routinemäßig automatisiert durch Lichtabsorptionsmessungen von Blutproben quantifiziert [11]. Typische Messgeräte, beispielsweise ein Sysmex XE-5000 Hematology Analyzer (Sysmex Corporation, Kobe, Japan), bestimmen das Hämoglobin (Hb) mit einem Fehler kleiner als 1% [39]. Der Normbereich im Blut umfasst bei erwachsenen Frauen 12.3–15.3 g/dl und bei erwachsenen Männern 14.0–17.5 g/dl [11], mit zu geringen Werten bei Anämie. Bei der Ursachenfindung für eine bestehende Anämie können folgende Parameter helfen: Anzahl der Erythrozyten (RBC, *red blood cells*), mittleres Zellvolumen (MCV, *mean corpuscular volume*) der Erythrozyten, mittleres korpuskuläres Hämoglobin (MCH, *mean corpuscular hemoglobin*), Hämatokrit (Hct), Erythropoetin, Retikulozyten, Serum-Ferritin, C-reaktives Protein (CRP), Transferrinsättigung, löslicher Transferrinrezeptor, Zink-Protoporphyrin IX (ZnPP), Bilirubin, Vitamin B_6, B_{12} oder Folsäure [11].

ZnPP und PPIX im Blut bzw. in den Erythrozyten können mittels kommerziell verfügbarem CE-zertifizierten HPLC (*high performance liquid chromatography*) Kit [40] bestimmt werden. Zum quantitativen Nachweis werden die über HPLC räumlich getrennten Porphyrine der Erythrozyten mittels Fluoreszenzdetektion und Vergleich mit einem Fluoreszenzstandard quantifiziert [40,41]. Für ZnPP existiert eine weitere Methode, nämlich die Bestimmung des Verhältnisses ZnPP zu Häm mittels kommerziell verfügbarer *front-face fluorimetry*, dem Hämatofluorometer [17,42]. Dabei wird die Fluoreszenz des erythrozytengebundenen ZnPP direkt aus einer Blutprobe oder gewaschenen Erythrozyten gemessen. Bei dieser Methode wird allerdings die Fluoreszenz der gesamten Probe erfasst, so dass bei Vollblut die Untergrundfluoreszenz anderer Blutbestandteile wie Bilirubin die Messwerte verfälschen kann [3,43-47]. Dieser Störeinfluss kann durch das Entfernen der zumeist plasmagebundenen, störenden Fluorophoren aus der Probe durch Waschen der Erythrozyten weitgehend unterdrückt werden [3,17,46-49], was allerdings ein entsprechend ausgestattetes Labor mit geschultem Personal erfordert.

Nichtinvasiver Nachweis von Zink-Protoporphyrin IX

Im folgenden Abschnitt werden Verbesserungen zum Stand der Technik beim fluoreszenzspektroskopischen Nachweis von Porphyrinen vorgestellt.

Medizinische Aspekte und Grundlagen

Die ZnPP-Konzentration in Erythrozyten stellt einen Parameter zum Nachweis eines persistierenden Eisenmangels dar. Eisenmangel betrifft weltweit mehr als zwei Milliarden Menschen, sowohl in Entwicklungsländern als auch in Industrieländern, insbesondere Säuglinge, Kinder, Jugendliche sowie Frauen in gebärfähigem Alter und Schwangere. Eisenmangel kann unter anderem zu einer Anämie, einer erhöhten Anfälligkeit für Infektionskrankheiten und Beeinträchtigungen in der kindlichen Entwicklung führen. Starker Eisenmangel erhöht die Mortalität [50]. Einem persistierenden Eisenmangel kann durch Gabe von Eisenpräparaten oder Nahrungsergänzungs-

mitteln entgegengewirkt werden [50]. Eine ungezielte Gabe von Eisenpräparaten führt allerdings nicht zwangsläufig zu einer Abnahme der Mortalität [51]. In Malariagebieten wurde sogar eine Zunahme der Mortalität bei Kindern beobachtet, die Eisenpräparate ohne bestehenden Eisenmangel erhalten hatten [50,52,53]. Aus diesem Grund empfiehlt die Weltgesundheitsorganisation (WHO), dass in Entwicklungsländern Eisenpräparate nur nach einem Eisenmangelnachweis verabreicht werden sollten [53]. Dabei wird die Bestimmung der ZnPP-Konzentration in Erythrozyten als Parameter für den Eisenmangelnachweis empfohlen [53,54]. Als Herausforderung erweist sich dabei die quantitative Bestimmung des ZnPP. Noch fehlt nämlich ein feldtaugliches Gerät, das auch ohne Labor und Blutentnahme auskommt [54], wie es für HPLC oder Hämatofluorometer erforderlich ist. Insbesondere der Verzicht auf eine Blutentnahme erscheint für die Akzeptanz in der Bevölkerung unerlässlich, vor allem für die Diagnostik bei Kleinkindern.

Eine Gewebeart, die für die nichtinvasive Quantifizierung von ZnPP geeignet erscheint, ist die orale Mucosa: Sie ist leicht zugänglich, nicht pigmentiert und gut durchblutet. Durch die gute Durchblutung ist gewährleistet, dass sich eine ausreichende Anzahl Fluorophore im Probenvolumen befindet. Außerdem kann die erzeugte ZnPP-Fluoreszenz bei guter Durchblutung effizient detektiert werden, weil die Eindringtiefe des Anregungslichts im Gewebe wegen der hohen Blutabsorption nur gering ist und die ZnPP-Fluoreszenz somit nahe am Detektor entsteht. Das Hauptproblem bei der Quantifizierung der ZnPP-Fluoreszenz an Gewebe ist deren Überlagerung mit der Autofluoreszenz anderer Gewebebestandteile. In der Mundschleimhaut sind dies insbesondere Kollagene und Elastin, sowie NADH und FAD im Epithel [55]. Deren Fluoreszenzintensität ist in Gewebe um Größenordnungen stärker als die wegen der Hämabsorption äußerst schwache ZnPP-Fluoreszenz der Erythrozyten [56]. Ein weiteres Problem ist die Streuung von Anregungs- und Fluoreszenzlicht, die unbekannt ist, aber wesentlich die Eindringtiefe von Licht beeinflusst.

Lichtausbreitung in Gewebe

Für die erfolgreiche Entwicklung eines Gerätes zur nichtinvasiven Quantifizierung von ZnPP sind also unter anderem die Einflüsse von Streuung und (Blut-)Absorption auf die Lichtausbreitung in Gewebe zu untersuchen. Eine präzise Angabe der Interaktion von Licht mit Gewebe würde die Lösung der Maxwellgleichungen unter Berücksichtigung aller Gewebebestandteile mit ihren vollständigen optischen Eigenschaften liefern [57]. Da die genaue Ausgestaltung, die Position und die Eigenschaften der Gewebebestandteile nicht bekannt und anderweitig auch nicht von Interesse sind, wird die Lichtausbreitung in Gewebe gewöhnlich näherungsweise mit der Strahlungstransportgleichung beschrieben [58,59]. Dabei werden die Photonen nicht als Wellen aufgefasst, sondern nur ihre Teilcheneigenschaften betrachtet; Kohärenz, Polarisation und nichtlineare Effekte werden vernachlässigt [60]. Außerdem werden die unbekannten mikroskopischen Gewebebestandteile durch makroskopische Größen, nämlich durch Streuwahrscheinlichkeit und Absorptionswahrscheinlichkeit pro Weglänge, μ_s und μ_a, ersetzt [60]. Die Ablenkung bei einem Streuprozess wird durch die Streuwahrscheinlichkeitsdichtefunktion $p(\theta)$ beschrieben, wobei θ der Winkel zwischen Einfallsrichtung und Streurichtung ist [58]. Eine übliche Näherung ist die Henyey-Greenstein-Phasenfunktion $p(g)$ [58,59,61], bei der die Wahrscheinlichkeit der Winkelablenkung über einen einzigen Parameter, nämlich den Anisotropiefaktor g, angegeben ist [58]. Dabei bedeutet $g = 0$, dass das Photon bei einem Streuprozess in eine zufällige Richtung gestreut wird, und $g = 1$, dass es in Vorwärtsrichtung gestreut wird [58]. Gewebetypisch ist vorwärtsgerichtete Streuung mit $g \approx 0.90$, wobei auch Werte von $g = 0.70$ bis zu $g = 0.997$ vorkommen können [58,62].

Die Strahlungstransportgleichung selbst ist wegen ihrer sechs unabhängigen Variablen nur schwer lösbar [60]. Daher wird zur Beschreibung der Lichtausbreitung in Gewebe häufig die Diffusionsgleichung als Vereinfachung der Strahlungstransportgleichung verwendet [4,60]. Hierfür wird die Strahlungstransportgleichung durch eine Reihenentwicklung in Kugelflächenfunktionen ausgedrückt, die dann nach dem ersten Glied abgebrochen wird [60]. Ein vorwärtsgerichteter Streuprozess mit Streukoeffizient μ_s und Anisotropiefaktor g wird durch einen isotropen Streu-

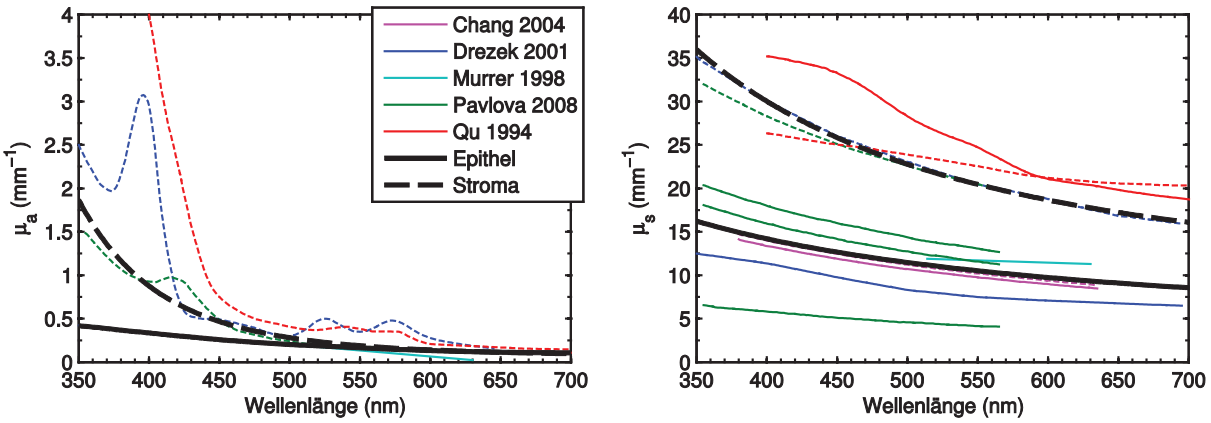

Abbildung 3. Absorptionskoeffizient μ_a (linke Grafik) und Streukoffizient μ_s (rechte Grafik) von Epithel (durchgezogene dünne Linien) und Stroma (gestrichelte dünne Linien) verschiedener Schleimhautsorten, kompiliert aus [55,68-71]. Eingezeichnet ist zusätzlich jeweils eine ausgleichende Kurve (schwarze dicke Linien). Beim Absorptionskoeffizient ist ein mehr oder weniger stark ausgeprägtes Absorptionsmaximum im Blauen erkennbar, das von der Hämoglobinabsorption des Blutes herrührt. In der ausgleichenden Kurve wurde die Blutabsorption nicht berücksichtigt.

prozess mit dem reduzierten Streukoeffizienten $\mu_s' = (1 - g)\ \mu_s$ ersetzt [60]. Die genannten optischen Parameter sind dabei im Allgemeinen ortsabhängig. Die Diffusionsgleichung ist in ihrer Gültigkeit beschränkt, insbesondere auf den Fall $\mu_a \ll \mu_s'$ und auf Orte in ausreichender Entfernung von gerichteten Lichtquellen [60]. Der Fall geringer Absorption im Vergleich zur Streuung liegt jedoch in vielen Gewebetypen vor [58].

Eine andere Möglichkeit, die Strahlungstransportgleichung zu lösen, sind Monte-Carlo-Simulationen [1,60,63,64]. Bei dieser Art der Lösung der Strahlungstransportgleichung wird die Propagation einer Vielzahl von Photonen durch Gewebe auf statistischem Weg simuliert, so dass jedes Photon einem unterschiedlichen, zufällig gewürfelten Pfad folgt, der von den optischen Gewebeparametern abhängt [1,60,63,64]. Die tatsächliche Lichtausbreitung im Gewebe wird dann durch Mittelung über sehr viele (häufig mehr als 10^8) Photonen erreicht [1,60,64]. Diese Lösung der Strahlungstransportgleichung ist exakt, besonders auch für den Fall $\mu_a \geq \mu_s'$, und ist nur durch statistische Fehler beschränkt, die durch Erhöhung der simulierten Photonenzahl reduziert werden können [1,63]. Diese Methode ist wegen ihrer Exaktheit beliebt und als Referenzmethode bei komplexen Gewebegeometrien anzusehen [65-67]. Allerdings ist sie bei großen Photonenzahlen sehr rechenzeitintensiv [1,60].

Um Lichtausbreitung in Gewebe theoretisch untersuchen zu können, ist die Kenntnis der verschiedenen optischen Parameter erforderlich. Die Bestimmung der Parameter μ_a, μ_s und g erfordert mindestens drei Messungen [58]. Da menschliches Gewebe *in vivo* ohne Verletzung des Patienten nur über dessen Oberfläche zugänglich ist und *in vivo* auch nur schlecht definierte geometrische Bedingungen vorliegen, werden in vielen Fällen Gewebestücke *ex vivo* untersucht, mit definierter Probendicke und weitgehend homogener Zusammensetzung wie es auch in den Studien, an denen der Autor beteiligt war, durchgeführt wurde [5,6,58]. Diese Methode hat den Nachteil, dass das Blut als wesentlicher Bestandteil von Gewebe zumindest teilweise fehlt. Bei Verwendung mancher Literaturwerte von optischen Parametern muss deshalb der Blutanteil zusätzlich berücksichtigt werden. Weiterhin werden starke intra- und interindividuelle Unterschiede, sowie Unterschiede zwischen verschiedenen Messmethoden beobachtet. In Abbildung 3 sind aus Literaturdaten [55,68-71] beispielhaft Absorption und Streuung von (oraler) Mucosa zusammengestellt. Die gezeigten Streukoeffizienten von Epithelgewebe unterscheiden sich nahezu um einen Faktor 10, weshalb eine präzise generelle Berechnung der Lichtausbreitung in diesem Gewebetyp unmöglich ist.

Der Anteil von Blut an Gewebe ist ebenfalls eine wenig bekannte Größe: Für (orale) Mucosa beispielsweise finden sich nur wenige Berichte über Messungen oder Schätzungen des Blutvolu-

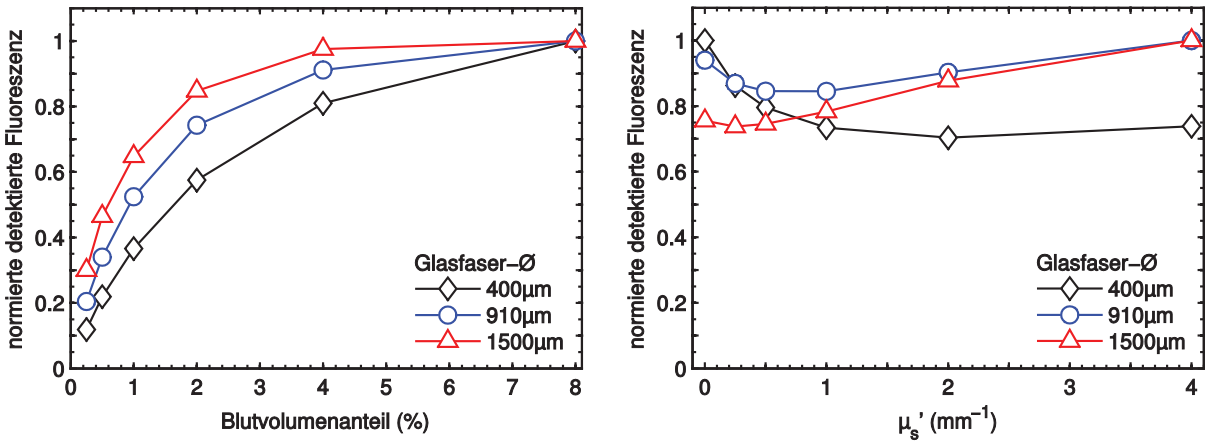

Abbildung 4. Gezeigt sind Ergebnisse von Monte-Carlo-Simulationen, die mit der vorgeschlagenen Methode [1] durchgeführt wurden. Links ist die Abhängigkeit der mittels Glasfaser gemessenen Fluoreszenzintensität von Blut in einer homogenen, streuenden Probe mit $\mu_s' = 2.0\,\mathrm{mm}^{-1}$ vom Blutvolumenanteil in dieser Probe für verschiedene Glasfaserdurchmesser gezeigt, jeweils normiert auf die maximale Intensität. Rechts ist für die gleiche simulierte Geometrie die gemessene Fluoreszenzintensität in Abhängigkeit von der Streuung bei gleichbleibendem Blutvolumenanteil von 2% dargestellt, ebenfalls normiert auf die maximale Intensität.

menanteils (BVF, *blood volume fraction*) in der Literatur [68,70,72-75], wobei die angegebenen Werte im Bereich 0.15% bis 3.6% liegen. Die niedrigsten Werte können wegen der unzulässigen Mittelung über blutleeres Epithelgewebe und die darunterliegende *Lamina propria* ausgeschlossen werden oder aufgrund unklarer Berücksichtigung von Packaging-Effekten [76]. Als wahrscheinlicher Wert kann aufgrund dieser Recherche ein Blutvolumenanteil im Bereich 0.7% bis 1.7% angenommen werden.

Sollen nun Berechnungen zur Lichtausbreitung von sichtbarem, insbesondere blauem Licht in (oraler) Mucosa durchgeführt werden, so kann die Diffusionstheorie nicht angewendet werden, da durch die hohe Blutabsorption im blauen Spektralbereich die Bedingung $\mu_a \ll \mu_s'$ nicht gilt. Daher wurde im Rahmen einer in dieser Dissertation vorgestellten Studie [1] eine Methode für Monte-Carlo-Simulationen entwickelt, mit deren Hilfe die Lichtausbreitung in geschichteten streuenden Medien (zum Beispiel oraler Mucosa) berechnet werden kann, wobei gleichzeitig Fluoreszenzlicht durch Absorption an einem oder mehreren Fluorophoren generiert und die Lichtausbreitung des Fluoreszenzlichtes ebenfalls simuliert werden kann. Dieses Verfahren verkürzt die Simulationsdauer gegenüber üblichen Monte-Carlo-Methoden erheblich, insbesondere durch die Ausnutzung der Prozessoren kostengünstiger Grafikkarten, auf denen mehr als 100 Photonenpfade gleichzeitig simuliert werden können [1].

Der Anteil von Georg Hennig an dieser Studie war die Entwicklung und Implementierung der vorgestellten Methode mit der Unterstützung von Dr. Wolfgang Beyer, die Durchführung der Simulationen und das Verfassen des Manuskriptes mit Anregungen, Korrekturen und Unterstützung durch die anderen Autoren.

In Abbildung 4 sind exemplarisch die Ergebnisse von Simulationen gezeigt, die mithilfe der vorgestellten Methode [1] durchgeführt wurden. Dabei wurde der Einfluss des Blutvolumenanteils und der Streuung auf die tatsächlich gemessene Fluoreszenzintensität untersucht. Es zeigt sich, dass bei größeren Faserdurchmessern der Einfluss des Blutvolumenanteils auf das gemessene Fluoreszenzsignal sinkt. Die kleinstmögliche Sensitivität auf Streuung hat die Glasfaser mit mittlerem Kerndurchmesser, $d = 910\,\mu\mathrm{m}$.

Quantitativer Nachweis von Zink-Protoporphyrin IX in Blut

Eine große Herausforderung bei der nichtinvasiven Quantifizierung von ZnPP ist das Untergrundsignal, das von endogenen Fluorophoren herrührt und erwartungsgemäß deutlich intensiver ist als das schwache Fluoreszenzsignal des ZnPP im Blut [56]. Daher muss das Untergrundsignal

stark verringert werden. Vielversprechende Ansätze hierfür können anhand von Vollblutproben überprüft werden. Die Autofluoreszenz im Blutplasma ist, wie oben beschrieben, ein Störfaktor, der die Anwendbarkeit des Hämatofluorometers auf Messungen an Vollblut limitiert [3]. Damit können anhand von Untersuchungen an Vollblutproben zwei Ziele erfüllt werden: die Überprüfung der Anwendbarkeit einer Methode zur Unterdrückung des Autofluoreszenzuntergrundes *in vivo*, und eine Verbesserung zum Stand der Technik beim Nachweis vom ZnPP in Vollblut. Für derartige Untersuchungen sind grundsätzlich eine Lichtquelle und eine Detektionseinheit erforderlich. Eine spektral aufgelöste Detektion ist mittels eines gekühlten CCD-Spektrometers bei hoher Effizienz möglich. Als Lichtquelle kommen kohärente und inkohärente Lichtquellen in Frage. Für die freie Wahl des Spektralbereichs des Anregungslichtes eigneten sich also durchstimmbare Laser, beispielsweise Farbstofflaser, oder aber spektral gefiltertes Licht aus einer Lichtquelle mit großer spektraler Breite. Durchstimmbare Laser können allerdings nicht eingesetzt werden, da sie zu kostspielig sind und auch wegen ihrer Größe und Anfälligkeit nicht für eine klinische Studie in Frage kommen. Handelsübliche Filtereinheiten für inkohärentes Licht wie zum Beispiel Gittermonochromatoren haben den Nachteil, dass sie bei den für den Nachweis von Porphyrinen erforderlichen geringen spektralen Bandbreiten eine geringe Transmissionseffizienz aufweisen und somit nur begrenzt für den sensitiven Nachweis geringer ZnPP-Konzentrationen geeignet erschienen.

Daher wurde im Rahmen einer in dieser Dissertation vorgestellten Studie [2] eine Filtereinheit aus durchstimmbaren Interferenzfiltern entwickelt, die in der Lage ist, bis zu einer spektralen Bandbreite von 5 nm hinab mit einer Transmissionseffizienz größer als 75% kollimiertes Weißlicht zu filtern. Sie wurde in Deutschland als Gebrauchsmuster geschützt [7] und in den USA zum Patent angemeldet [8]. Mit dieser Filtereinheit war die Beleuchtung von Proben mit einer Ausgangsleistung von 6 mW bei einer Bandbreite von 5 nm FWHM möglich [3], wobei eine Xenon-Kurzbogenlampe mit 500 W Eingangsleistung als Weißlichtquelle benutzt wurde.

Der Anteil von Georg Hennig an dieser Studie war die Erfindung der vorgestellten Filtereinheit gemeinsam mit Dr. Herbert Stepp und Prof. Gary M. Brittenham, die Entwicklung und teilweise der Aufbau der Filtereinheit, die Anleitung der durchgeführten Messungen, die Auswertung der Messergebnisse sowie das Verfassen des Manuskripts mit Anregungen, Korrekturen und Unterstützung durch die anderen Autoren.

Mithilfe der vorgestellten Lichtquelle wurde die Fluoreszenz von Blutproben in Auflichtgeometrie untersucht. Dabei zeigte sich bei Anregung um 425 nm deutliche ZnPP-Fluoreszenz um 593 nm, wobei ein Autofluoreszenzuntergrund sichtbar war. Bei Anregung um 407 nm reduzierte sich die ZnPP-Fluoreszenz bei gleich hohem Untergrund auf 23%. Zusätzlich war PPIX-Fluoreszenz um 627 nm sichtbar. Daher konnte der Untergrund durch Subtraktion der Fluoreszenzspektren bei diesen beiden Anregungswellenlängen effizient rechnerisch eliminiert werden, ohne das Messsignal, also die Porphyrinfluoreszenz, wesentlich zu reduzieren. Im Rahmen einer in dieser Dissertation vorgestellten Studie [3] wurde in Kooperation zwischen dem Laser-Forschungslabor und dem Institut für Laboratoriumsmedizin des Klinikums der Universität München gezeigt, dass die gemessenen Porphyrinfluoreszenzintensitäten die jeweiligen Porphyrinkonzentrationen quantitativ abbilden, unbeeinflusst vom Autofluoreszenzuntergrund beispielsweise durch Bilirubin im Blutplasma. Der vorgestellte Messaufbau zeigte bei Messungen an nicht verarbeitetem Blut bezüglich des ZnPP-Wertes vergleichbar gute Ergebnisse wie das kommerziell verfügbare AVIV Hämatofluorometer (Modell 206D, Aviv Biomedical, Inc., Lakewood, NJ, USA) an gewaschenen Erythrozyten und lieferte zusätzlich einen Wert für den PPIX-Anteil, der mit dem AVIV Hämatofluorometer nicht erfasst wird [3].

Der Anteil von Georg Hennig an dieser Studie war die Mitentwicklung der Methode, die Entwicklung und Optimierung des optischen Aufbaus, die Anleitung der Messungen, die Auswertung, sowie das Verfassen des Manuskriptes mit Anregungen, Korrekturen und Unterstützung durch die anderen Autoren.

Ausblick auf nichtinvasive Messungen

Die durchgeführten Messungen zeigen, dass die vorgestellte Methode grundsätzlich geeignet ist, Untergrundfluoreszenz effizient zu verringern. Daher wurde sie für die Anwendung auf die nichtinvasive Quantifizierung eines Fluorophors in Gewebe in den USA zum Patent angemeldet [8]. Ob diese Methode tatsächlich auch bei Gewebe funktioniert, ist nur im Versuch *in vivo* zu beurteilen. Monte-Carlo-Simulationen von Fluoreszenzlicht in geschichteten streuenden Medien [1] zeigen nämlich, dass der geschichtete Aufbau, insbesondere die Epithelschichten, durchaus das Messsignal beeinflusst. Aufbau und genaue stoffliche Zusammensetzung der oralen Mucosa ist patientenabhängig. Eine sichere Aussage über die Anwendbarkeit der vorgestellten Methode und Gerätschaft [2,3] ist daher derzeit nicht möglich.

Deshalb hat das Laser-Forschungslabor in Kooperation mit der Gynäkologie und dem Labor für Laboratoriumsmedizin des Klinikums der Universität München eine Studie vorbereitet, die an Müttern unmittelbar postpartal nichtinvasiv Zink-Protoporphyrin IX untersucht. In dieser Situation weisen die Probandinnen (statistisch) eine hohe Prävalenz von 48% für Eisenmangel bzw. 9% für eine Eisenmangelanämie auf [77], wobei der Eisenmangelnachweis mittels ZnPP einer Bestimmung der Parameter Hämoglobin oder Serum-Ferritin überlegen ist [78]. In dieser klinischen Studie kommt ein Gerät zum Einsatz, das sich im Vergleich zum vorgestellten Aufbau [3] im Wesentlichen dadurch unterscheidet, dass das Anregungs- und Fluoreszenzlicht über einen Lichtleiter zum Ort der Messung, der oralen Mucosa der Patientin, hin- bzw. davon weggeleitet wird. Erste Vorversuche zu dieser Studie zeigen, dass der Autofluoreszenzuntergrund um bis zu 97% reduziert werden kann, so dass das zu quantifizierende Porphyrinfluoreszenzsignal in der gleichen Größenordnung liegt wie das verbleibende Untergrundsignal. Diese vielversprechenden ersten Ergebnisse deuten darauf hin, dass ein erfolgreicher nichtinvasiver Nachweis von ZnPP an der oralen Mucosa möglich ist.

Photodynamische Wirkung

Grundlagen

Neben den vorgestellten Anwendungen zur Diagnostik werden Porphyrine auch therapeutisch bei der photodynamischen Therapie (PDT) eingesetzt. Diese beruht auf der photodynamischen Wirkung, die erstmals im Jahr 1897 durch den Doktoranden Oscar Raab und Prof. Hermann von Tappeiner in München beschrieben wurde [28,79-81]. Die photodynamische Wirkung von Porphyrinen beruht darauf, dass von Porphyrinen absorbierte Photonen nicht nur Fluoreszenz, sondern auch Intersystem-Crossing und danach in Anwesenheit von Sauerstoff einen Energieübertrag auf das Sauerstoffmolekül induzieren können [28,82,83]. Dadurch entsteht ein kurzlebiges angeregtes Singulett-Sauerstoffmolekül oder andere reaktive Sauerstoffverbindungen (*reactive oxygen species,* ROS), die mittels Oxidation Zellbestandteile schädigen [9,28,84]. Substanzen, die eine photodynamische Wirkung zeigen, werden als Photosensibilisatoren (*photosensitizers*) bezeichnet [28]. Für die photodynamische Wirkung sind also ein Photosensibilisator in unmittelbarer Nähe des zu schädigenden Gewebes, Licht bei zum Photosensibilisator passender Wellenlänge und Sauerstoff erforderlich [28].

Photodynamische Therapie

Bei der photodynamischen Therapie (PDT) wird die photodynamische Wirkung genutzt, um Gewebe gezielt zu schädigen, also direkt zu zerstören (Induzierung von Apoptose oder Nekrose) [28,83], oder indirekt zu zerstören, beispielsweise durch Auslösen einer Immunantwort [28,83] oder durch Zerstörung der Vaskularisierung des Tumors [83]. Bei der 5-ALA PDT wird durch Applikation von 5-ALA der ratenlimitierende Prozess in der Hämsynthese, nämlich die 5-ALA-Synthese, umgangen, wodurch sich PPIX besonders in den Mitochondrien anreichert [28]. Die

Anreicherung erfolgt in Tumorzellen hinreichend selektiv, insbesondere wegen der reduzierten Aktivität der Ferrochelatase in Tumorzellen [28,85], bei malignen Gliomen auch wegen der teilweisen Auflösung der Blut-Hirn-Schranke [85]. Diese selektive Anreicherung stellt einen Vorteil gegenüber der unselektiven Anreicherung bei anderen Photosensibilisatoren dar, da bei unselektiver Anreicherung das gesamte beleuchtete Gewebe geschädigt wird, weshalb die Lichtverteilung möglichst scharf auf die zu schädigende Region beschränkt werden muss. Bei der 5-ALA PDT hingegen kann wegen der selektiven Anreicherung auch über die Tumorränder hinaus beleuchtet werden, ohne gravierende Schäden im Normalgewebe zu erzeugen. Nach systemischer Applikation kann eine systemische Anreicherung allerdings zu einer gewissen generellen (Haut-)Photosensibilisierung des Patienten führen, ähnlich wie sie bei der erythropoetischen Protoporphyrie beobachtet wird [28]. Bei oberflächlicher Anwendung der 5-ALA PDT zum Beispiel auf der Haut oder in Hohlorganen wie der Blase wird diese generelle Photosensibilisierung durch topische Applikation von 5-ALA vermieden [28].

Bei der interstitiellen PDT bei malignen Gliomen [86,87] ist neben der Akkumulation des Photosensibilisators auch die suffiziente Ausleuchtung des Tumors zur Entfaltung der photodynamischen Wirkung eine Herausforderung. Hierzu werden im Tumorvolumen Lichtleiter platziert, über die die Beleuchtung erfolgt. Ein Problem bei der Anwendung der interstitiellen PDT besteht in der Messung der erzielten photodynamischen Wirkung, der Dosimetrie [28,88].

Eine präzise Berechnung bzw. Messung aller relevanten Parameter in einer sogenannten expliziten Dosimetrie ist mangels genauer Kenntnis der Sauerstoffversorgung und -verteilung, Verteilung des Photosensibilisators und Raumbestrahlungsstärke im Tumor schwierig [86,88]. Theoretische Rechnungen zur Lichtausbreitung sind wegen der großen zu erwartenden Schwankungsbreite der optischen Gewebeparameter fehlerträchtig [4,88]. So können unterschiedliche Vaskularisierung und der damit verbundene unterschiedliche Blutvolumenanteil, sowie nekrotische und damit dunkel verfärbte Tumorbereiche für stark unterschiedliche Absorption sorgen. Weiterhin kann die Absorption des Gewebes durch den Photosensibilisator selbst beeinflusst sein [88], und sich daher durch Ausbleichen des Photosensibilisators im Laufe der Therapie ändern. Außerdem ist die Geschwindigkeit des Ausbleichens des Photosensibilisators neben der Raumbestrahlungsstärke auch von der Konzentration und der Verfügbarkeit von Sauerstoff abhängig [88,89].

Ein anderer Ansatz ist die implizite Dosimetrie, bei der der Behandlungserfolg anhand nur eines einzigen Parameters festgestellt wird [88]. Im Rahmen einer in dieser Dissertation vorgestellten Studie [4] wurde ein Dosimetriekonzept entwickelt, das die detektierte Fluoreszenzintensität von PPIX im Verlauf der PDT als Parameter nutzt, weil das Ausbleichen im Behandlungsverlauf mit der erzielten Gewebeschädigung verknüpft ist. Da es bei der interstitiellen PDT, insbesondere bei Glioblastomen im Gehirn, nicht vorstellbar ist, für diese Messungen zusätzliche Lichtleiter stereotaktisch zu implantieren, musste das Dosimetriekonzept auf einige wenige Messungen mit den für therapeutische Zwecke implantierten Lichtleitern beschränkt werden. Anhand theoretischer Modellierung mittels Simulationsrechnungen wurde aufgezeigt [4], wie trotz stark variierender und unbekannter optischer Gewebeparameter mit diesen wenigen Messungen der Anteil an noch vorhandenem PPIX bestimmt werden könnte. Mit einem solchen Konzept könnte man also bereits während der PDT erfahren, ob eine weitere Beleuchtung wegen noch nicht ausgeblichenem PPIX im Tumor lohnenswert bzw. erforderlich wäre. Somit könnte letztlich eine solchermaßen individualisierte PDT gegenüber dem Standardprotokoll zu einer Verbesserung im Behandlungserfolg führen.

Der Anteil von Georg Hennig an dieser Studie war die Mitentwicklung der vorgestellten Methode mit Dr. Ann Johansson, die Durchführung der Simulationsrechnungen, sowie Unterstützung beim Verfassen des Manuskriptes.

LITERATUR

1. **G. Hennig**, H. Stepp, R. Sroka und W. Beyer, „Comparison of an accelerated weighted fluorescence Monte Carlo simulation method with reference methods in multi-layered turbid media," Appl. Opt. **52 (5)**, 1066-1075 (2013).
2. **G. Hennig**, G. M. Brittenham, R. Sroka, G. Kniebühler, M. Vogeser und H. Stepp, „Bandwidth-variable tunable optical filter unit for illumination and spectral imaging systems using thin-film optical band-pass filters," Rev. Sci. Instrum. **84 (4)**, 0431131-0431137 (2013).
3. **G. Hennig**, C. Gruber, M. Vogeser, H. Stepp, S. Dittmar, R. Sroka und G. M. Brittenham, „Dual-wavelength excitation for fluorescence-based quantification of zinc protoporphyrin IX and protoporphyrin IX in whole blood," J. Biophotonics, doi: 10.1002/jbio.201200228 (2013).
4. **G. Hennig**, H. Stepp und A. Johansson, „Photobleaching-based method to individualize irradiation time during interstitial 5-aminolevulinic acid photodynamic therapy," Photodiagnosis Photodyn. Ther. **8 (3)**, 275-281 (2011).
5. W. Y. Khoder, R. Sroka, **G. Hennig**, M. Seitz, S. Siegert, K. Zillinberg, C. Gratzke, C. G. Stief und A. J. Becker, „The 1,318-nm diode laser supported partial nephrectomy in laparoscopic and open surgery: preliminary results of a prospective feasibility study," Lasers Med. Sci. **26 (5)**, 689-697 (2011).
6. W. Y. Khoder, K. Zilinberg, R. Waidelich, C. G. Stief, A. J. Becker, T. Pangratz, **G. Hennig** und R. Sroka, „Ex vivo comparison of the tissue effects of six laser wavelengths for potential use in laser supported partial nephrectomy," J. Biomed. Opt. **17 (6)**, 068005 (2012).
7. **G. Hennig**, H. Stepp, G. M. Brittenham, T. Pongratz und M. Vogeser, „Optische Filtereinheit mit verstellbarer spektraler Transmission," 20 2012 005 809.6 (21.08.2012).
8. G. M. Brittenham, H. Stepp und **G. Hennig**, „Measurement of a Fluorescent Analyte using Tissue Excitation," WO 2013 040398 A1 (21.03.2013).
9. P. Karlson, D. Doenecke, J. Koolman, G. Fuchs und W. Gerok, *Karlsons Biochemie und Pathobiochemie* (Thieme, 2005).
10. E. J. Speckman, J. Hescheler und R. Köhling, *Physiologie* (Elsevier Health Sciences Germany, 2008).
11. M. Wick, W. Pinggera und P. Lehmann, *Clinical Aspects and Laboratory - Iron Metabolism, Anemias: Concepts in the Anemias of Malignancies and Renal and Rheumatoid Diseases* (Springer Wien, Wien, 2011).
12. C. Ekmekcioglu und W. Marktl, *Essentielle Spurenelemente: Klinik und Ernährungsmedizin* (Springer, 2006).
13. T. Hankeln, B. Ebner, C. Fuchs, F. Gerlach, M. Haberkamp, T. L. Laufs, A. Roesner, M. Schmidt, B. Weich, S. Wystub, S. Saaler-Reinhardt, S. Reuss, M. Bolognesi, D. De Sanctis, M. C. Marden, L. Kiger, L. Moens, S. Dewilde, E. Nevo, A. Avivi, R. E. Weber, A. Fago und T. Burmester, „Neuroglobin and cytoglobin in search of their role in the vertebrate globin family," J. Inorg. Biochem. **99 (1)**, 110-119 (2005).
14. U. Stölzel, T. Stauch und M. O. Doss, „Porphyrien," Der Internist **51 (12)**, 1525-1533 (2010).
15. H. R. Horton, L. A. Moran, K. G. Scrimgeour, C. Biele, J. D. Rawn und M. D. Perry, *Biochemie* (Pearson Studium, 2008).
16. S. S. Bottomley, „Erythropoietic Disorders Involving Heme Biosynthesis," in *The Porphyrin Handbook*, K. M. Kadish, K. M. Smith, und R. Guilard, Hrsg. (Academic Press, San Diego, 2003), 1-21.
17. R. F. Labbe, H. J. Vreman und D. K. Stevenson, „Zinc protoporphyrin: A metabolite with a mission," Clin. Chem. **45 (12)**, 2060-2072 (1999).

18. A. P. Orfanos, R. Guthrie, D. C. Jinks und D. W. Vollmer, „Simultaneous assay of zinc protoporphyrin and protoporphyrin IX in dried blood," Clin. Chim. Acta **181 (2)**, 213-217 (1989).
19. Y. M. Roh, K. Kim und H. Kim, „Zinc protoporphyrin IX concentrations between normal adults and the lead-exposed workers measured by HPLC, spectrofluorometer, and hematofluorometer," Ind. Health **38 (4)**, 372-379 (2000).
20. A. A. Lamola, S. Piomelli, M. G. Poh-Fitzpatrick, T. Yamane und L. C. Harber, „Erythropoietic protoporphyria and lead intoxication: the molecular basis for difference in cutaneous photosensitivity. II. Different binding of erythrocyte protoporphyrin to hemoglobin," J. Clin. Invest. **56 (6)**, 1528-1535 (1975).
21. J. J. Leonard, T. Yonetani und J. B. Callis, „Fluorescence Study of Hybrid Hemoglobins Containing Free Base and Zinc Protoporphyrin IX," Biochemistry **13 (7)**, 1460-1464 (1974).
22. R. E. Hirsch, M. J. Lin und C. M. Park, „Interaction of zinc protoporphyrin with intact oxyhemoglobin," Biochemistry **28 (4)**, 1851-1855 (1989).
23. S. Piomelli, A. A. Lamola, M. F. Poh-Fitzpatrick, C. Seaman und L. C. Harber, „Erythropoietic protoporphyria and lead intoxication: the molecular basis for difference in cutaneous photosensitivity. I. Different rates of disappearance of protoporphyrin from the erythrocytes, both in vivo and in vitro," J. Clin. Invest. **56 (6)**, 1519-1527 (1975).
24. S. Sandberg und A. Brun, „Light-induced protoporphyrin release from erythrocytes in erythropoietic protoporphyria," J. Clin. Invest. **70 (3)**, 693-698 (1982).
25. M. C. van Beekvelt, W. N. Colier, R. A. Wevers und B. G. van Engelen, „Performance of near-infrared spectroscopy in measuring local O(2) consumption and blood flow in skeletal muscle," J. Appl. Physiol. **90 (2)**, 511-519 (2001).
26. G. Metzgeroth, B. Schultheis, A. Dorn-Beineke, R. Hehlmann und J. Hastka, „Zinc protoporphyrin, a useful parameter to address hyperferritinemia," Ann. Hematol. **86 (5)**, 363-368 (2007).
27. M. Lecha, H. Puy und J. C. Deybach, „Erythropoietic protoporphyria," Orphanet J. Rare Dis. **4**, 19 (2009).
28. R. H. Pottier, B. Krammer und H. Stepp, *Photodynamic Therapy With ALA: A Clinical Handbook* (Royal Society of Chemistry, 2006).
29. P. Sweigert, Z. Xu, Y. Hong und S. Swavey, „Nickel, copper, and zinc centered ruthenium-substituted porphyrins: effect of transition metals on photoinduced DNA cleavage and photoinduced melanoma cell toxicity," Dalton Trans. **41 (17)**, 5201-5208 (2012).
30. Q. Chen und R. E. Hirsch, „A direct and simultaneous detection of zinc protoporphyrin IX, free protoporphyrin IX, and fluorescent heme degradation product in red blood cell hemolysates," Free Radic. Res. **40 (3)**, 285-294 (2006).
31. C. Raja, K. Ananthanarayanan und P. Natarajan, „Studies on the photophysical characteristics of poly(carboxylic acid)s bound protoporphyrin IX and metal complexes of protoporphyrin IX," Eur. Polym. J. **42 (3)**, 495-506 (2006).
32. S. A. Prahl, „Optical Absorption of Hemoglobin" (1999), heruntergeladen am 27.04.2010, http://omlc.ogi.edu/spectra/hemoglobin/index.html.
33. A. A. Lamola und T. Yamane, „Zinc protoporphyrin in the erythrocytes of patients with lead intoxication and iron deficiency anemia," Science **186 (4167)**, 936-938 (1974).
34. R. E. Hirsch, „Front-face fluorescence spectroscopy of hemoglobins," Methods Enzymol. **232**, 231-246 (1994).
35. A. Straßer, „Photophysik und Photochemie von Tetraphenylporphyrinkomplexen des Zirconiums und des Hafniums," Dissertation (Universität Regensburg, 2004).
36. T. P. Wijesekera und D. Dolphin, „Some preparations and properties of porphyrins," Adv. Exp. Med. Biol. **193**, 229-266 (1985).
37. M. Gouterman, „Spectra of Porphyrins," J. Mol. Spectrosc. **6 (1)**, 138-163 (1961).

38. R. E. Dickerson, H. B. Gray, H. W. Sichting und M. Darensbourg, *Prinzipien der Chemie* (Walter de Gruyter, 1988).
39. B. Dabkowski, „Hematology analyzers: an overview of what's new," CAP Today, 22-44 (2010).
40. Immundiagnostik AG, „Zinc-Protoporphyrin/Protoporpyrin HPLC Kit - Manual (preliminary)" (2011), heruntergeladen am 20.08.2012, http://www.immundiagnostik.com/fileadmin/pdf/Zink-Protoporphyrin_KC2700.pdf.
41. E. Rossi und P. Garcia-Webb, „Red cell zinc protoporphyrin and protoporphyrin by HPLC with fluorescence detection," Biomed. Chromatogr. **1 (4)**, 163-168 (1986).
42. W. E. Blumberg, J. Eisinger, A. A. Lamola und D. M. Zuckerman, „Hematofluorometer," Clin. Chem. **23 (2)**, 270-274 (1977).
43. E. Buhrmann, W. C. Mentzer und B. H. Lubin, „The influence of plasma bilirubin on zinc protoporphyrin measurement by a hematofluorimeter," J. Lab. Clin. Med. **91 (4)**, 710-716 (1978).
44. V. Karacic, D. Prpicmajic und S. Telisman, „The Relationship between Zinc Protoporphyrin (ZPP) and Free Erythrocyte Protoporphyrin (FEP) in Lead-Exposed Individuals," Int. Arch. Occup. Environ. Health **47 (2)**, 165-177 (1980).
45. P. Grandjean und J. Lintrup, „Sources of variation in fluorometry of zinc protoporphyrin in blood," Scand. J. Work. Environ. Health **7 (4)**, 311-312 (1981).
46. J. Hastka, J. J. Lasserre, A. Schwarzbeck, M. Strauch und R. Hehlmann, „Washing erythrocytes to remove interferents in measurements of zinc protoporphyrin by front-face hematofluorometry," Clin. Chem. **38 (11)**, 2184-2189 (1992).
47. R. F. Labbe, A. Dewanji und K. McLaughlin, „Observations on the zinc protoporphyrin/heme ratio in whole blood," Clin. Chem. **45 (1)**, 146-148 (1999).
48. R. B. Schifman und P. R. Finley, „Measurement of near-normal concentrations of erythrocyte protoporphyrin with the hematofluorometer: influence of plasma on "front-surface illumination" assay," Clin. Chem. **27 (1)**, 153-156 (1981).
49. P. J. Parsons, N. V. Stanton, E. W. Gunter, D. Huff, J. R. Meola und A. A. Reilly, „An Interlaboratory Comparison of Control Materials for Use with Hematofluorometers," Clin. Chem. **35 (10)**, 2059-2065 (1989).
50. M. B. Zimmermann und R. F. Hurrell, „Nutritional iron deficiency," Lancet **370 (9586)**, 511-520 (2007).
51. J. M. Tielsch, S. K. Khatry, R. J. Stoltzfus, J. Katz, S. C. LeClerq, R. Adhikari, L. C. Mullany, S. Shresta und R. E. Black, „Effect of routine prophylactic supplementation with iron and folic acid on preschool child mortality in southern Nepal: community-based, cluster-randomised, placebo-controlled trial," Lancet **367 (9505)**, 144-152 (2006).
52. S. Sazawal, R. E. Black, M. Ramsan, H. M. Chwaya, R. J. Stoltzfus, A. Dutta, U. Dhingra, I. Kabole, S. Deb, M. K. Othman und F. M. Kabole, „Effects of routine prophylactic supplementation with iron and folic acid on admission to hospital and mortality in preschool children in a high malaria transmission setting: community-based, randomised, placebo-controlled trial," Lancet **367 (9505)**, 133-143 (2006).
53. „Conclusions and recommendations of the WHO Consultation on prevention and control of iron deficiency in infants and young children in malaria-endemic areas," Food Nutr. Bull. **28 (4 Suppl)**, S621-627 (2007).
54. R. J. Stoltzfus, R. Heidkamp, D. Kenkel und J. P. Habicht, „Iron supplementation of young children: learning from the new evidence," Food Nutr. Bull. **28 (4 Suppl)**, S572-584 (2007).
55. I. Pavlova, C. R. Weber, R. A. Schwarz, M. Williams, A. El-Naggar, A. Gillenwater und R. Richards-Kortum, „Monte Carlo model to describe depth selective fluorescence spectra of epithelial tissue: applications for diagnosis of oral precancer," J. Biomed. Opt. **13 (6)**, 064012 (2008).

56. X. Chen, „Feasibility test for non-invasive detection of zinc protoporphyrin in oral mucosa and retina," Master of Science Thesis (University of California, Davis, 2009).
57. F. Voit, A. Hohmann, J. Schafer und A. Kienle, „Multiple scattering of polarized light: comparison of Maxwell theory and radiative transfer theory," J. Biomed. Opt. **17 (4)**, 045003 (2012).
58. V. V. Tuchin, „Methods and Algorithms for the Measurement of the Optical Parameters of Tissues," in *Tissue Optics - Light Scattering Methods and Instruments for Medical Diagnosis,* Ed. 2, V. V. Tuchin, Hrsg. (SPIE, Bellingham, Washington, USA, 2007), 143-256.
59. A. Welch, M. C. Gemert und W. Star, „Definitions and Overview of Tissue Optics," in *Optical-Thermal Response of Laser-Irradiated Tissue*, A. J. Welch und M. J. C. Gemert, Hrsg. (Springer Netherlands, 2011), 27-64.
60. L. V. Wang und H. Wu, *Biomedical Optics: Principles and Imaging* (Wiley, 2007).
61. L. G. Henyey und J. L. Greenstein, „Diffuse radiation in the galaxy," Astrophys. J. **93 (1)**, 70-83 (1941).
62. D. J. Faber, M. C. Aalders, E. G. Mik, B. A. Hooper, M. J. van Gemert und T. G. van Leeuwen, „Oxygen saturation-dependent absorption and scattering of blood," Phys. Rev. Lett. **93 (2)**, 028102 (2004).
63. S. A. Prahl, M. Keijzer, S. L. Jacques und A. J. Welch, „A Monte Carlo Model of Light Propagation in Tissue," SPIE Proceedings of Dosimetry of Laser Radiation in Medicine and Biology **IS 5**, 102-111 (1989).
64. L. Wang, S. L. Jacques und L. Zheng, „MCML - Monte Carlo modeling of light transport in multi-layered tissues," Comput. Methods Programs Biomed. **47 (2)**, 131-146 (1995).
65. T. Binzoni, T. S. Leung, R. Giust, D. Rufenacht und A. H. Gandjbakhche, „Light transport in tissue by 3D Monte Carlo: influence of boundary voxelization," Comput. Methods Programs Biomed. **89 (1)**, 14-23 (2008).
66. A. V. Bykov, M. Y. Kirillin und A. V. Priezzhev, „Monte Carlo Simulation of Light Propagation in Human Tissues and Noninvasive Glucose Sensing," in *Handbook of Optical Sensing of Glucose in Biological Fluids and Tissues*, V. V. Tuchin, Hrsg. (Taylor & Francis, 2010), 65-95.
67. G. Zonios und A. Dimou, „Modeling diffuse reflectance from homogeneous semi-infinite turbid media for biological tissue applications: a Monte Carlo study," Biomed. Opt. Express **2 (12)**, 3284-3294 (2011).
68. J. N. Qu, C. Macaulay, S. Lam und B. Palcic, „Optical properties of normal and carcinomatous bronchial tissue," Appl. Opt. **33 (31)**, 7397-7405 (1994).
69. L. H. Murrer, H. P. Marijnissen und W. M. Star, „Monte Carlo simulations for EndoBronchial Photodynamic Therapy: the influence of variations in optical and geometrical properties and of realistic and eccentric light sources," Lasers Surg. Med. **22 (4)**, 193-206 (1998).
70. R. Drezek, K. Sokolov, U. Utzinger, I. Boiko, A. Malpica, M. Follen und R. Richards-Kortum, „Understanding the contributions of NADH and collagen to cervical tissue fluorescence spectra: Modeling, measurements, and implications," J. Biomed. Opt. **6 (4)**, 385-396 (2001).
71. S. K. Chang, D. Arifler, R. Drezek, M. Follen und R. Richards-Kortum, „Analytical model to describe fluorescence spectra of normal and preneoplastic epithelial tissue: comparison with Monte Carlo simulations and clinical measurements," J. Biomed. Opt. **9 (3)**, 511-522 (2004).
72. G. Zonios, L. T. Perelman, V. Backman, R. Manoharan, M. Fitzmaurice, J. Van Dam und M. S. Feld, „Diffuse reflectance spectroscopy of human adenomatous colon polyps in vivo," Appl. Opt. **38 (31)**, 6628-6637 (1999).
73. R. Hornung, T. H. Pham, K. A. Keefe, M. W. Berns, Y. Tadir und B. J. Tromberg, „Quantitative near-infrared spectroscopy of cervical dysplasia in vivo," Hum. Reprod. **14 (11)**, 2908-2916 (1999).

74. P. R. Bargo, S. A. Prahl, T. T. Goodell, R. A. Sleven, G. Koval, G. Blair und S. L. Jacques, „In vivo determination of optical properties of normal and tumor tissue with white light reflectance and an empirical light transport model during endoscopy," J. Biomed. Opt. **10 (3)**, 034018 (2005).
75. A. Amelink, J. Haringsma und H. J. Sterenborg, „Noninvasive measurement of oxygen saturation of the microvascular blood in Barrett's dysplasia by use of optical spectroscopy," Gastrointest. Endosc. **70 (1)**, 1-6 (2009).
76. J. C. Finlay und T. H. Foster, „Effect of pigment packaging on diffuse reflectance spectroscopy of samples containing red blood cells," Opt. Lett. **29 (9)**, 965-967 (2004).
77. W. Kirschner, K. Friese und J. W. Dudenhausen, „Eisenmangel in der Schwangerschaft," Der Gynäkologe **44 (9)**, 8 (2011).
78. E. J. Harthoorn-Lasthuizen, J. Lindemans und M. M. Langenhuijsen, „Erythrocyte zinc protoporphyrin testing in pregnancy," Acta Obstet. Gynecol. Scand. **79 (8)**, 660-666 (2000).
79. G. Kick, G. Messer und G. Plewig, „Historische Entwicklung der Photodynamischen Therapie," Der Hautarzt **47 (8)**, 644-649 (1996).
80. O. Raab, „Ueber die Wirkung fluorescirender Stoffe auf Infusorien," Z. Biol. **39**, 524-546 (1900).
81. H. von Tappeiner, „Ueber die Wirkung fluorescierender Stoffe auf Infusorien nach Versuchen von O. Raab," Münch. Med. Wochenschr. **47**, 5-7 (1900).
82. E. G. Mik, J. Stap, M. Sinaasappel, J. F. Beek, J. A. Aten, T. G. van Leeuwen und C. Ince, „Mitochondrial PO2 measured by delayed fluorescence of endogenous protoporphyrin IX," Nat. Methods **3 (11)**, 939-945 (2006).
83. K. Pizova, K. Tomankova, A. Daskova, S. Binder, R. Bajgar und H. Kolarova, „Photodynamic therapy for enhancing antitumour immunity," Biomedical papers of the Medical Faculty of the University Palacky, Olomouc, Czechoslovakia **156 (2)**, 93-102 (2012).
84. T. Theodossiou und A. J. MacRobert, „Comparison of the photodynamic effect of exogenous photoprotoporphyrin and protoporphyrin IX on PAM 212 murine keratinocytes," Photochem. Photobiol. **76 (5)**, 530-537 (2002).
85. A. Johansson, F. Faber, G. Kniebühler, H. Stepp, R. Sroka, R. Egensperger, W. Beyer und F. W. Kreth, „Protoporphyrin IX fluorescence and photobleaching during interstitial photodynamic therapy of malignant gliomas for early treatment prognosis," Lasers Surg. Med. **45 (4)**, 225-234 (2013).
86. A. Johansson, G. Palte, O. Schnell, J. C. Tonn, J. Herms und H. Stepp, „5-Aminolevulinic acid-induced protoporphyrin IX levels in tissue of human malignant brain tumors," Photochem. Photobiol. **86 (6)**, 1373-1378 (2010).
87. A. Johansson, F. W. Kreth, W. Stummer und H. Stepp, „Interstitial Photodynamic Therapy of Brain Tumors," IEEE J. Sel. Topics Quantum Electron. **16 (4)**, 841-853 (2010).
88. B. C. Wilson, M. S. Patterson und L. Lilge, „Implicit and Explicit Dosimetry in Photodynamic Therapy: a New Paradigm," Lasers Med. Sci. **12 (3)**, 182-199 (1997).
89. K. K. Wang, W. J. Cottrell, S. Mitra, A. R. Oseroff und T. H. Foster, „Simulations of measured photobleaching kinetics in human basal cell carcinomas suggest blood flow reductions during ALA-PDT," Lasers Surg. Med. **41 (9)**, 686-696 (2009).

ORIGINALMANUSKRIPTE

Comparison of an accelerated weighted fluorescence Monte Carlo simulation method with reference methods in multi-layered turbid media

GEORG HENNIG, HERBERT STEPP, RONALD SROKA UND WOLFGANG BEYER

Applied Optics **52 (5)**, 1066–1075 (2013)

Comparison of an accelerated weighted fluorescence Monte Carlo simulation method with reference methods in multi-layered turbid media

Georg Hennig,[†,*] Herbert Stepp, Ronald Sroka, and Wolfgang Beyer

Laser-Forschungslabor, LIFE Center, Klinikum der Universität München, Marchioninistr. 23, München 81377, Germany

*Corresponding author: georg.hennig@med.lmu.de

Received 8 November 2012; revised 14 December 2012; accepted 23 December 2012;
posted 3 January 2013 (Doc. ID 179480); published 8 February 2013

Monte Carlo (MC) simulations are frequently used to simulate the radial distribution of remitted fluorescence light from tissue surfaces upon pencil beam excitation to gather information about influences of different tissue parameters. Here, the "weighted direct emission method" (WDEM) is proposed, which uses a weighted MC simulation approach for both excitation and fluorescence photons, and is compared to four other methods in terms of accuracy and speed, and using a broad range of tissue-relevant optical parameters. The WDEM is 5.2× faster on average than a fixed weight MC approach while still preserving its accuracy. Additional gain of speed can be achieved by implementing it on graphics processing units.

OCIS codes: 170.3660, 170.6280, 290.7050, 170.4580, 170.6510.

1. Introduction

Non-invasive optical measurements for diagnostic purposes are becoming increasingly popular [1]. Especially, the evaluation of the excitation and fluorescence light distribution remitted from tissue surfaces allows for diagnosis of skin alterations, such as tumors or inflammations [1–3], and the qualitative or quantitative measurement of endogenic or exogenic fluorophores [1–5], such as photosensitizers for photodynamic therapy [1,6]. The excitation and fluorescence light distribution is influenced by many factors, such as fluorophore concentration, epithelium layer thickness, and blood perfusion [2,5]. Computer simulations of excitation and fluorescence light propagation may help to understand influences of the optical parameters of the skin, which may contain information about metabolism [1] and structure [1,3], or influences of the excitation/detection geometry [4,7–9] on the amount and distribution of remitted excitation and fluorescence light.

Light propagation in tissue is frequently modeled using Monte Carlo (MC) simulations [10]. In the straightforward ("fixed weight") MC approach, the photons are absorbed as a whole [11]. Especially for highly scattering media such as tissue [12], this has the effect that most photons are absorbed before they reach regions at large distances from the light source and therefore a long simulation time is required for sufficient signal-to-noise ratio (SNR) at these distances. This problem is addressed in the "weighted" MC approach: photon bunches are simulated which carry a specific weight, which is reduced after each propagation step due to absorption instead of terminating the propagation of the photon at a single absorption event [13–15]. Therefore, the photon bunches undergo many scattering events and propagate a long distance away from the source before they are finally terminated. Their contribution to the absorbed amount of light at several places improves the SNR ratio, effectively accelerating the simulations. For further acceleration, parallel simulations of several photons are recommended. Especially,

1559-128X/13/051066-10$15.00/0

simulations on graphics processing units (GPU) have become popular, offering several hundreds of parallelized processors at consumer product price [16].

Fluorescence light emission can be incorporated into MC simulations of light propagation using different methods [7,9,11,17–21]. There are in principle two approaches. In the first approach, referred to as the "direct emission approach," fluorescence photons are generated exactly at the position where absorption of an excitation photon by a fluorophore has occurred, followed by simulation of the propagation of the fluorescence photon [7,9,11,20,21]. In the second approach, referred to as the "separated emission approach," the fluorescence light is simulated in two steps. In the first step, the excitation light distribution inside the medium is simulated. In the second step, fluorescence photons are emitted according to the absorbed excitation light distribution and their propagation is simulated [17–19].

A modification of the separated emission approach is the simulation of the light distribution implementing scattering only and scaling afterward by the appropriate absorption coefficient (excitation and emission wavelength), avoiding separate simulation of excitation and emission photon distributions. This method is referred to as "white light MC method" [19,22,23]. However, it assumes equal scattering coefficients for both the excitation and fluorescence emission wavelength [19,23] and is therefore not further considered.

The main advantages of the direct emission approach are its straightforward implementation and its accuracy, as no accuracy losses for the fluorescence photon emission distribution occur due to segmentation in volume elements as in the second approach [19,21]. The simulated fluorescence distribution converges toward the exact result for an increasing number of simulated photons. However, the SNR at regions distant from the excitation light source is typically bad because many photons are simulated which do not propagate far enough, which results in long simulation duration. In contrast, the separated emission approach is usually considerably faster; however its accuracy is limited not only by the segmentation in volume elements, but also by the finite volume considered.

In the direct emission approach, the propagation of an excitation photon can be simulated with a fixed weight MC method, and a single fluorescence photon is generated upon absorption of the excitation photon by a fluorophore [11,20,21]. The propagation of the fluorescence photon is then simulated with either a fixed weight or a weighted MC approach [11,19]. Another implementation of the direct emission approach is the simulation of the excitation photons using a weighted MC approach, and recording each place where absorption occurs, where in a second step, a fluorescence photon with appropriate weight is generated [11]. However, in this latter implementation, a large number of fluorescence photons are emitted for each excitation photon, where the precise number depends on the optical parameters and is unknown beforehand. Also, this implementation does not improve the SNR compared to the fixed weight MC simulation of the excitation photons [11].

Here, we propose the "weighted direct emission method" (WDEM), which combines the advantages of both implementations of the direct emission approach: the propagation of excitation and fluorescence photons is simulated using a weighted MC simulation approach, while emitting only a single fluorescence photon per excitation photon. It is compared with the "direct emission method" (DEM), where both excitation and fluorescence photons are simulated using a fixed weight MC method and fluorescence photons are generated upon absorption of an excitation photon by a fluorophore. The simulation methods were implemented by modifying the source code of the simulation program "MCML" (MC for multilayered media) [13,15,24], and the WDEM also by modifying the MCML's GPU equivalent "GPUMCML" [25]. Therefore, the same settings are available as in the original MCML code, such as number of layers and optical parameters, extended by the fluorophore's location and optical properties. The radially symmetric remitted fluorescence light distribution upon pencil beam excitation of multilayered turbid media was recorded, in addition to the volume absorption of excitation and fluorescence light and the remitted excitation light distribution.

These two implementations of the direct emission approach, the proposed WDEM and the DEM, are compared to three implementations of the separated emission approach. The program `mcfluor` published by Jacques [18,26] was used as a reference implementation of the "weighted separated emission method" (WSEM). In this method, the excitation light distribution is simulated using a weighted MC approach and stored in volume elements. In a second step, inside each volume element, a fixed number of fluorescence photons with appropriate weight are generated. The propagation of the fluorescence photons is also simulated using a weighted MC approach. An accelerated implementation of the separated emission approach is the "forward emission method" (FEM), which is again a modification of the MCML code. The excitation light distribution is simulated as in the WSEM using a weighted MC approach, but the fluorescence detection probability distribution for each depth is simulated as described by Swartling *et al.* [19] rather than for each volume element, thus exploiting the symmetry of the geometry. The remitted fluorescence light distribution is then calculated by a two dimensional (2D) convolution of the excitation light distribution and the fluorescence detection probability distribution for each depth [19]. An accelerated way to simulate the fluorescence detection probability distribution exploits the reversibility of photon paths, and is referred to as the "reverse method" (RM) and is also implemented by modifying the MCML code. The volume absorption of fluorescence photons, which are injected

in "reverse" direction at the point of detection (here: the surface), can be interpreted as detection probability after appropriate scaling [6,17,19]. This method avoids simulating fluorescence photons, which do not reach the detector (here: the surface), and therefore yields further acceleration. To calculate the remitted fluorescence light distribution, again a 2D convolution of the excitation light distribution and the fluorescence detection probability distribution has to be performed. However, this convolution may be very time consuming and requires a large amount of computer memory when large numbers of volume elements are used [19], and may therefore limit the gain of speed achieved by these accelerated simulation methods. Therefore, for fast 2D convolutions of radially symmetric functions the discrete Hankel transform (DHT) is used [27–29], which helps to overcome this issue.

In this study, the proposed WDEM is compared to these four different reference methods in terms of accuracy and speed over a broad range of tissue-relevant optical parameters. An overview over the implemented methods is shown in Table 1. The optimal choices for simulations, depending whether speed or accuracy is required, are identified. The WDEM is also implemented for parallelized simulations on GPU and compared to the central processing unit (CPU) implementation in terms of speed.

2. Simulation Methods and Evaluation

A. Input Parameters and Recorded Parameters

All distances are considered to be dimensionless, but can be interpreted as cm for distances and cm^{-1} for the corresponding optical parameters. A semi-infinite medium was simulated, or a layer thickness $d = 10^6$ was used for MCML derived programs, which do not implement semi-infinite media. The fluorophore was simulated within the layer depth $z \in [0, 1]$, and the relative absorption of the fluorophore at the excitation wavelength was $\mu_{a,\mathrm{fl}}/\mu_{a,x} = 0.1$ with the total absorption coefficient $\mu_{a,x}$, and the quantum efficiency of the fluorophore was set to $\gamma = 1$. Reemission of fluorescence photons upon absorption of fluorescence photons by the fluorophore itself is neglected. Excitation light photons were injected at the origin, $r = 0$ and $z = 0$, perpendicular to the surface of the medium.

For all optical parameters, the subscript "x" denotes the excitation wavelength and "m" the fluorescence emission wavelength. The refractive index of the medium was chosen wavelength-independent for both the excitation and emission wavelength, $n_{1,x} = n_{1,m} = 1.4$, and outside $n_{0,x} = n_{0,m} = 1.0$. The scattering process was simulated using the Henyey–Greenstein phase function [30], with the wavelength-independent anisotropy parameter $g_x = g_m = 0.9$ frequently used for tissue scattering [12]. Further optical properties, the absorption coefficient for excitation and emission wavelengths, $\mu_{a,x}$ and $\mu_{a,m}$, and the scattering coefficient, $\mu_{s,x}$ and $\mu_{s,m}$ were varied as shown in Table 2. A total of $2 \times 9 = 18$ sets of optical parameters (low and high scattering coefficients, "LOW" and "HIGH") were simulated, covering a broad range of tissue-relevant optical parameters [12] for distances interpreted as cm and the corresponding optical parameters as cm^{-1}. Other ranges of optical parameters, e.g., higher absorption and

Table 1. Overview of the Methods Used for the Different Simulation Methods

	Excitation	Fluorescence		
	Weighted Simulation	Weighted Simulation	Direct Emission	Convolution Necessary
DEM	no	no	yes	no
WDEM	yes	yes	yes	no
WSEM	yes	yes	no	no
FEM	yes	yes	no	yes
RM	yes	yes	no	yes

Table 2. List of the Simulation Input Optical Parameters Denoted by aa to cc, with Three Different Absorption[a,b] and Scattering Coefficients[a,c], Respectively

		aa	ab	ac	ba	bb	bc	ca	cb	cc
LOW	$\mu_{a,x}$	1.0	1.0	1.0	0.2	0.2	0.2	5.0	5.0	5.0
	$\mu_{a,m}$	0.5	0.5	0.5	0.1	0.1	0.1	2.5	2.5	2.5
	$\mu_{s,x}$	20	4	100	20	4	100	20	4	100
	$\mu_{s,m}$	15	3	75	15	3	75	15	3	75
HIGH	$\mu_{a,x}$	1.0	1.0	1.0	0.2	0.2	0.2	5.0	5.0	5.0
	$\mu_{a,m}$	0.5	0.5	0.5	0.1	0.1	0.1	2.5	2.5	2.5
	$\mu_{s,x}$	200	40	1000	200	40	1000	200	40	1000
	$\mu_{s,m}$	150	30	750	150	30	750	150	30	750

[a]The subscript "x" denotes the excitation wavelength, "m" the emission wavelength.
[b]The absorption coefficient at the excitation wavelength $\mu_{a,x}$ includes both absorption by tissue and fluorophore.
[c]Low scattering coefficients ("LOW"), high scattering coefficients ("HIGH").

scattering in the UV range, are covered as well by interpreting the distances and optical parameters as given in units different from centimeter. The fluorophore was therefore simulated up to a depth of 1 cm inside the tissue.

The remitted radius-dependent fluorescence per area, $F(r)$, was recorded independently from its angular distribution in surface elements within $r \in [0, 2]$, with a radial resolution $dr = 0.02$, i.e., a number of elements $n_r = 100$. The volume absorption $A_x(r,z)$ and $A_m(r,z)$ was recorded in ring-shaped volume elements with the same radial resolution, within a depth $z \in [0, 1]$, with a layer thickness resolution $dz = 0.02$, i.e., a number of elements $n_z = 50$. From the remitted fluorescence light $F(r)$, the total remitted fluorescence F was calculated. $F(r)$ and F were normalized to the number of injected excitation photons as in the original MCML code [13,15,24].

B. Monte Carlo Simulation Programs

An overview over the different implemented methods, which are described in detail in the following sections, is shown in Table 1.

1. Direct Emission Method

The MCML code [13,15,24] was modified to simulate the photons using a fixed weight MC approach. Excitation photon are absorbed after each propagation step with the absorption probability $P_{a,x} = \mu_{a,x}/(\mu_{a,x} + \mu_{s,x})$, where $\mu_{a,x}$ is the total absorption coefficient at the excitation wavelength, including fluorophore absorption and $\mu_{s,x}$ is the scattering coefficient.

Fluorescence emission was implemented by emitting a fluorescence photon into a randomly sampled direction upon excitation photon absorption with the fluorescence emission probability $P_{\mathrm{fl}} = \gamma \cdot \mu_{a,\mathrm{fl}}/\mu_{a,x}$, where $\mu_{a,\mathrm{fl}}/\mu_{a,x}$ is the fluorophore's relative contribution to the total absorption coefficient and γ is its quantum efficiency. The propagation of the fluorescence photon was then simulated using again a fixed weight MC approach.

2. Weighted Direct Emission Method

The excitation light distribution is simulated using the original MCML code [13,15,24]. In this method, at the endpoint of each simulated propagation step, the weight w_x of the photon is reduced by $w_{a,x}$ to take absorption into account, according to

$$w_{a,x} = \frac{\mu_{a,x}}{\mu_{a,x} + \mu_{s,x}} w_x. \tag{1}$$

In the WDEM, which is proposed in this study, fluorescence emission is implemented by converting the excitation photon after each simulation step by chance into a fluorescence photon, with an arbitrarily chosen probability P_{fl}. Therefore, only a single fluorescence photon is generated for each excitation photon that does not exit the tissue volume. This concept also allows adjusting P_{fl}. It can be expected that decreasing P_{fl} increases the propagation distance of excitation photons and improves the SNR at regions far from the source, which also increases the number of generated fluorescence photons there. On the other hand, fewer fluorescence photons are generated near the source. To compensate for this arbitrary probability P_{fl}, the fluorescence photon is initiated with the weight

$$w_{\mathrm{fl}} = w_{a,x} \frac{\gamma \cdot \mu_{a,\mathrm{fl}}}{\mu_{a,x}} \frac{1}{P_{\mathrm{fl}}}. \tag{2}$$

If no fluorescence photon is generated, the surviving excitation photon continues propagation with the weight w_x^*, which is increased compared to the original MCML code, where the photon continues propagation with the weight $w_x - w_{a,x}$, as described by

$$w_x^* = (w_x - w_{a,x}) \frac{1}{1 - P_{\mathrm{fl}}}, \tag{3}$$

to preserve the overall weight of the excitation photons, i.e., conservation of energy. With respect to the excitation photon simulation, the conversion into a fluorescence photon is similar to the survival roulette during weighted MC simulations in the original MCML code [13,15,24] with the probability P_{fl}.

The propagation of the fluorescence photons is then simulated using the original MCML code with a survival roulette threshold reduced in relation to the initial weight of the fluorescence photon.

This method was ported to GPU simulation as well, modifying GPUMCML [25] instead of the original MCML code to incorporate fluorescence light simulation.

3. Weighted Separated Emission Method

The program `mcfluor` published by Jacques [18,26] simulates the absorbed excitation light distribution $A_x(r,z)$ in a similar way as in the MCML code [13,15,24] and is used to calculate the excitation light's fluence rate $\Phi_x(r,z)$ according to [11]

$$\Phi_x(r,z) = \frac{A_x(r,z)}{V \cdot \mu_{a,x}}, \tag{4}$$

where V is the volume of the ring-shaped volume elements.

In the second step, a fixed number of fluorescence photons are emitted at a point inside each volume element into random directions (one fluorescence photon per volume element and 10^4 injected excitation photons). Their initial weight is set to $w_{\mathrm{fl}} = \Phi_x(r,z) \cdot \gamma \cdot \mu_{a,\mathrm{fl}}/\mu_{a,x}$. The propagation of the fluorescence photons is then simulated using a weighted MC approach.

4. Forward Emission Method

In this method, excitation photons are simulated using the original MCML code [13,15,24]. The absorbed fraction of excitation light $A_x(r,z)$ is recorded for the given number $n_r \cdot n_z$ of ring-shaped volume

elements with thicknesses dr and dz, and the fluence rate $\Phi_x(r,z)$ is calculated according to Eq. (4).

In the second step, the fluorescence photon detection probability distribution $P_m(r',z)$ is simulated using the original MCML code by launching a given number of photons at $r'=0$ at each depth (index $i=1,2,\ldots,n_z$) in the middle of the volume element at $z_i=(i-0.5)\cdot dz$ uniformly in all directions. The distribution of the remitted light at the surface for each source depth z_i equals the radial detection probability distribution $P_m(r',z)$ for this depth.

In the last step, the remitted fluorescence light distribution $F(r)$ is calculated by a convolution of the excitation light distribution and the detection probability distribution for each z-layer:

$$F(\bar{r})=\sum_{i=1}^{n_z}\Phi_x(\bar{r},z_i)*P_m(\bar{r'},z_i). \tag{5}$$

It is emphasized that each convolution of the sum in Eq. (5) is a convolution in 2D over $\bar{r}=(r,\phi)$ and $\bar{r'}=(r',\phi')$, with the two radially symmetric functions $\Phi_x(r)$ and $P_m(r',z)$ at each given depth z_i. The resulting remitted fluorescence light distribution is again radially symmetric, $F(r)=F(\bar{r})$. This 2D convolution can be calculated by the fast Fourier transform with high-speed proportional to $n_r^2\log_2(n_r)$ [31]. If both functions are radially symmetric functions, the convolution can also be calculated by the DHT of order zero [27,29], improving the convolution speed even further proportional to n_r^2 [32]. Therefore, the DHT was used for convolution, using the GNU scientific library (GSL, version 1.14, Free Software Foundation, Inc., Boston, Massachusetts, USA) [33], however initializing the required matrix of Bessel zeros [33] only once, which further increases the convolution speed.

5. *Reverse Method*

In the first step, the excitation light distribution is simulated in the same way as in the FEM.

In the second step, the fluorescence photon detection probability is simulated by modifying the MCML code. Due to the reversibility of the photon path, instead of simulating fluorescence photons from their origin (r,z) to the surface, the reverse propagation of the photons from the surface to their point of absorption at (r,z) is simulated [6,17,19]. To achieve this, fluorescence photons are injected at the origin O' right below the surface into the medium. The random incident angles are sampled isotropically and the initial weights of the photons are scaled according to the detector sensitivity. In the simulated geometry presented here, it follows a Lambertian distribution, because the surface acts as the detector. Additionally, the randomly sampled incident angles θ are restricted to the critical angle θ_c to respect total reflection at the surface in the forward case. The angle θ_c is calculated from the refractive index of the outside medium n_0, and the inside medium n_1, with $n_1>n_0$, according to

$$\theta_c=\sin^{-1}\frac{n_0}{n_1}. \tag{6}$$

Reflection at the surface in the forward case is taken into account for the reverse case by reducing the initial weight of the photons according to the Fresnel equations. However, again the forward case (again, in contrast to the simulated photon propagation direction) has to be considered: the reflection of each photon is calculated as if it would propagate from inside-out instead of outside-in. The absorbed light distribution of the reverse injected fluorescence photons yields the detection probability according to

$$P_m(r,z)=c_{\text{reverse}}\frac{A_m(r,z)}{V\cdot\mu_{a,m}}, \tag{7}$$

where V is the volume of the ring-shaped volume elements and the scaling factor $c_{\text{reverse}}=\frac{1}{2}(1-\cos\theta_c)$ [19] to take into account the restriction to the critical angle θ_c.

In the final step, the remitted fluorescence light is calculated in the same way as in the FEM, summing up the convolutions performed according to Eq. 5.

C. Hardware

All simulations were performed on a single core of a dual core processor (Intel Core 2 CPU at 1.86 GHz, Intel Corporation, Santa Clara, California, USA). A consumer graphic card (GeForce GTX 460, NVIDIA Corporation, Santa Clara, California, USA) with 336 cores was used for simulations on the GPU.

D. Comparison of Accuracy and Speed

To compare different methods, the total remitted fluorescence F was evaluated. The relative residual of the radial distribution of the remitted fluorescence $F(r)$ was calculated, $\text{Rel. residual}(r)=F_{\text{Method 1}}(r)/F_{\text{Method 2}}(r)-1$.

The simulation programs were executed using a MATLAB (R2010a, MathWorks, Natick, Massachusetts, USA) script. The total simulation time t_{sim} required for simulating the remitted fluorescence $F(r)$ was recorded using MATLAB's `tic` and `toc` functions. The simulation for each of the 18 sets of optical parameters was repeated 10 times and averaged, yielding the average F and $F(r)$. The SNR was calculated from the 10 simulations for each recorded surface element using the standard deviation σ of the fluorescence signal and the average $F(r)$, $\text{SNR}(r)=F(r)/\sigma\{F(r)\}$. The maximal radius, $r_{\max}$, was determined, where for all $d<r_{\max}$ and all compared methods $\text{SNR}(d)>1$ and $F(d)>0$ (i.e., at least a single photon was detected). The effective simulation time t_{eff}, i.e., the time required for the same SNR, was calculated by evaluating the minimum of $\text{SNR}(d)$ and dividing t_{sim} by this minimum SNR^2 [Eq. (8)] to take into account that the SNR is proportional to $1/\sqrt{N}$. t_{eff} was then used as a measure for the effective speed of a simulation method.

$$t_{\mathrm{eff}} = \frac{t_{\mathrm{sim}}}{\min\{\mathrm{SNR}(d)\}^2}. \quad (8)$$

Finally, the effective simulation time t_{eff} of each set of optical parameters was normalized to the corresponding effective simulation time required by the DEM, i.e., $t_{\mathrm{eff,norm}} = t_{\mathrm{eff}}/t_{\mathrm{eff,DEM}}$. The average of the normalized effective simulation times $t_{\mathrm{eff,norm}}$ was calculated for the 9 sets of optical parameters for low and high scattering coefficients (LOW and HIGH), respectively, as well as minimum and maximum, yielding the range of $t_{\mathrm{eff,norm}}$.

E. Fluorescence Emission Probabilities P_{fl} of the WDEM

Different fluorescence emission probabilities P_{fl} for the WDEM were used during simulations for each of the 18 sets of optical parameters. The probability P_{fl} was varied within the range $0.1 \cdot \mu_{a,x}/(\mu_{a,x} + \mu_{s,x}) \le P_{\mathrm{fl}} \le 10 \cdot \mu_{a,x}/(\mu_{a,x} + \mu_{s,x})$, with values from the list $P_{\mathrm{fl}} \in [0.5, 0.1, 0.05, 0.01, 0.005, 0.001, 0.0001, 0.00001]$. The optimal choice $P_{\mathrm{fl,opt}}$ for each of the 18 sets of optical parameters was the P_{fl} where the effective simulation time, t_{eff}, was minimal.

F. Comparison of CPU and GPU Based Programs

One simulation run for each of the 18 sets of optical parameters using the CPU and GPU implementation of the WDEM was executed using a MATLAB script. The absolute time required for performing this run was recorded using the `tic` and `toc` functions of MATLAB. For the GPU simulations, the number of photons was increased to reduce influences of file read and write operations on the operating time. The operating time was then normalized to the number of simulated photons, yielding the time required for CPU and GPU simulations, t_{CPU} and t_{GPU}. GPU simulations were performed with and without recording the volume absorption for comparison how it affects the simulation speed. The speed improvement of GPU simulations over CPU simulations was calculated by the ratio $t_{\mathrm{CPU}}/t_{\mathrm{GPU}}$ for each of the 18 sets of optical parameters. The average of $t_{\mathrm{CPU}}/t_{\mathrm{GPU}}$ was calculated for each of the 9 sets of optical parameters for low and high scattering coefficients (LOW and HIGH), as well as minimum and maximum, yielding the range of $t_{\mathrm{CPU}}/t_{\mathrm{GPU}}$.

3. Results

For the WDEM, the probability P_{fl} for fluorescence photon emission after excitation photon absorption can be chosen arbitrarily, and which offers the possibility to optimize the SNR at equal simulation time. For each of the 18 sets of optical parameters, the optimal choice for $P_{\mathrm{fl,opt}}$ was evaluated such that t_{eff} was minimal. In Fig. 1, the correlation between $\mu_{a,x}/(\mu_{a,x} + \mu_{s,x})$ and $P_{\mathrm{fl,opt}}$ is shown.

In Table 3, a comparison of the total fluorescence remitted through the surface layer is shown. The remitted fluorescence is given in percent of the excitation photons (=100%). In the upper panel, the results for simulations with the optical parameters with low scattering coefficients (LOW) are shown, in the lower panel the results for simulations with high scattering coefficients (HIGH). Basically, identical results are found for all simulation programs, with small deviations: deviations between the DEM, WDEM, FEM, and RM are found in the order of 0.01%. Deviations of the program `mcfluor` implementing the WSEM are larger and in the order of 0.1%.

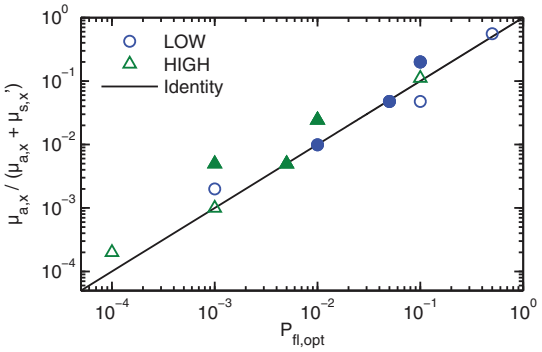

Fig. 1. (Color online) Ratio $\mu_{a,x}/(\mu_{a,x} + \mu_{s,x})$ for the 18 sets of optical parameters (with low and high scattering coefficients each, LOW and HIGH, 9 each) is plotted against the optimal fluorescence emission probability $P_{\mathrm{fl,opt}}$ for the WDEM, as well as the identity. Two overlapping points are indicated by solid symbols.

In Fig. 2, an example of $F(r)$ is shown (set of optical parameters: aa, LOW as indicated in Table 2) simulated by the WDEM, WSEM, and RM. The FEM showed perfect overlap with the RM and the DEM with the WDEM. In the lower panel, the relative residual between the two simulated $F(r)$ and $F_{\mathrm{WDEM}}(r)$ is shown, $F(r)/F_{\mathrm{WDEM}}(r) - 1$. At small distances $r < 0.1$ from the origin, systematic deviations $< 50\%$ of the WSEM, FEM and RM from the WDEM and the DEM were observed. At large distances $r > 1$, the FEM and the RM reported lower $F(r)$ (deviation $< 50\%$) than the WDEM. A similar observation was made for the other sets of optical parameters (data not shown); however in some cases, also the WSEM reported lower values (deviation $<$ 30%) than the WDEM at large distances.

To compare the speed of the different methods, the effective simulation times, normalized to the DEM, $t_{\mathrm{eff,norm}}$, were compared for each set of optical parameters. As shown in Fig. 3, only the WSEM is slower than the DEM in some cases. All other methods are faster with the RM being the fastest simulation method, followed by the FEM and the WDEM.

For low scattering coefficients (LOW), the WDEM is 4.9× faster on average than the DEM (range: 1.5× –2323×), the WSEM is 7.2× slower (range: 0.034× –50×), the FEM is 85× faster (range: 40× –2822×) and the RM is 510× faster (range: 154× –111026×). For high scattering coefficients (HIGH), the WDEM is 5.6× faster on average than the DEM (range: 2.2× –424×), the WSEM is 2.7× slower (range: 0.13× –21×), the FEM is 9.3× faster (range: 3.3× –68×) and the RM is 8027× faster (range: 1826× –77975×).

To evaluate the gain of speed achieved by the simulations on the GPU compared to the CPU, in Fig. 4,

Table 3. Total Remitted Fluorescence in Percent, Normalized to the Excitation Photons, for the Five Different Methods for 18 Different Optical Parameters[a] Denoted by aa to cc

		aa	ab	ac	ba	bb	bc	ca	cb	cc
LOW	DEM	1.67	0.97	2.27	1.85	0.80	2.02	1.11	0.90	1.71
	WDEM	1.67	0.97	2.27	1.85	0.80	2.03	1.11	0.90	1.71
	WSEM	1.70	0.97	2.31	1.68	0.64	2.02	1.19	0.99	1.80
	FEM	1.67	0.96	2.27	1.83	0.79	2.02	1.11	0.90	1.70
	RM	1.67	0.96	2.27	1.83	0.79	2.02	1.11	0.90	1.70
HIGH	DEM	2.29	2.00	1.78	1.77	2.09	1.07	2.01	1.32	2.29
	WDEM	2.29	2.00	1.79	1.77	2.09	1.07	2.01	1.32	2.28
	WSEM	2.33	2.04	1.86	1.78	2.02	1.08	2.07	1.40	2.43
	FEM	2.28	2.01	1.77	1.77	2.08	1.06	2.01	1.32	2.24
	RM	2.29	2.00	1.77	1.78	2.08	1.06	2.00	1.32	2.24

[a]As indicated in Table 2.

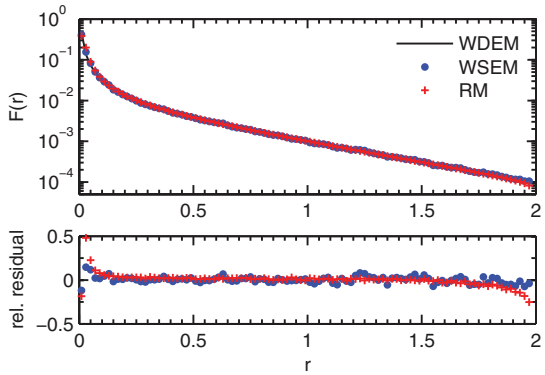

Fig. 2. (Color online) Remitted fluorescence per area $F(r)$, normalized by the number of excitation photons, for one set of optical parameters (aa, LOW, as indicated in Table 2) is shown in the upper panel. Three different methods, WDEM, WSEM, and RM are shown. The FEM is omitted as it shows a perfect overlap with the RM, and the DEM as it overlaps with the WDEM. In the lower panel, the relative residual of WSEM/WDEM and RM/WDEM is shown.

the ratio $t_{\mathrm{CPU}}/t_{\mathrm{GPU}}$ is shown for each of the 18 sets of optical parameters with and without recording the volume absorption of excitation and fluorescence light. If the volume absorption was recorded, on average, the GPU version performed for low scattering coefficients (LOW) 136× faster than the CPU version (range: 93× –177×), and for high scattering coefficients (HIGH) 164× faster (range: 111× –198×). The lowest speed improvement was found for low scattering and/or high absorption (especially ab, ca, and cb for both LOW and HIGH, as indicated in Table 2). If the volume absorption of excitation and fluorescence light was not recorded during simulation, an additional gain of speed of 1.7× (LOW) and 1.6× (HIGH) on average was found for the GPU version, resulting in an average speed improvement over the CPU version of 233× (range: 153× –287×) for low scattering coefficients (LOW) and of 262× (range: 199× –286×) for high scattering coefficients (HIGH).

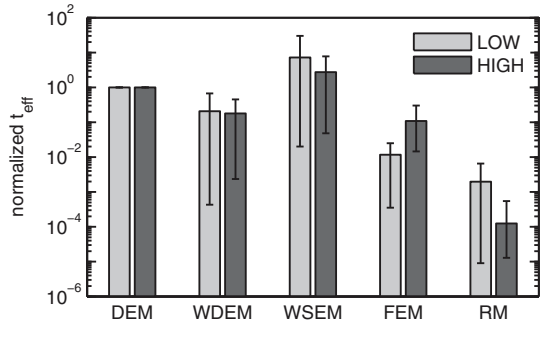

Fig. 3. Effective simulation time relative to t_{eff}(DEM) for the different methods is shown. For each method, on the left the results for low scattering coefficients (LOW) are shown, and on the right for high scattering coefficients (HIGH). Bars denote the mean simulation time, averaged over the 9 sets of optical parameters for low or high scattering coefficients (LOW and HIGH), and the error bars indicate the range. Please note the logarithmic y-axis scale.

4. Discussion

For a broad range of optical properties with low and high scattering coefficients (LOW and HIGH), the optimal choice for the probability that a fluorescence photon is emitted, $P_{\mathrm{fl,opt}}$, was identified. The correlation of $P_{\mathrm{fl,opt}}$ with $\mu_{a,x}/(\mu_{a,x}+\mu_{s,x})$ over four orders of magnitude suggest $P_{\mathrm{fl}}=\mu_{a,x}/(\mu_{a,x}+\mu_{s,x})$ as a good choice. If P_{fl} is chosen this way, as far as the generation of fluorescence photons from excitation photons is concerned, the proposed method

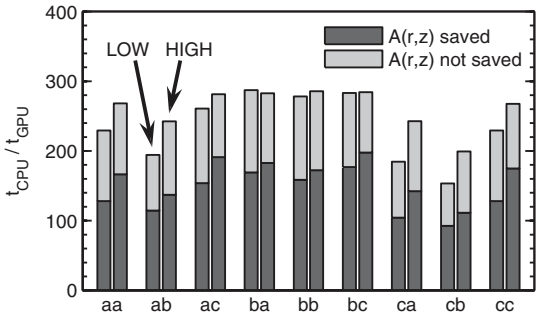

Fig. 4. Ratio of the total simulation time required by the CPU version and the GPU version is shown. The method WDEM was used to simulate fluorescence for 9 sets of optical parameters with low scattering coefficient (LOW, left bar for each set of optical parameters) and 9 sets of optical parameters with high scattering coefficient (HIGH, right bar for each set of optical parameters).

becomes similar to a modified DEM, with $P_{fl} = 1$: the excitation photons are simulated with fixed weight, and, if absorbed, continue propagation as fluorescence photons with an appropriate initial weight and are then simulated using a weighted MC simulation approach [11,19]. However, still the WDEM is preferred over this modified DEM, as both excitation and fluorescence photons are simulated using a weighted MC approach and therefore both excitation and fluorescence light distributions are simulated with improved SNR. The WDEM offers the possibility to be incorporated directly into simulation programs where a more complex geometry is simulated [16,34], as long as additional parameters such as the fluorophore distribution and optical parameters at the fluorescence wavelength can be defined.

This optimal choice of P_{fl} deviates from the expectations, as it was assumed that the adjustment of the fluorescence emission probability allowed investing more operating time in fluorescence photons generated far from the excitation source, where the low number of generated fluorescence photons reduces the SNR. However, in other problems and geometries the adjustable emission probability may find its use.

The WDEM is somewhat similar to a previously published method [7,9] where the fluorescence photons are also launched with a certain probability at each scattering event. However, this method does not aim to calculate the excitation light distribution and the published equations are valid for highly scattering media only.

Only the DEM and the WDEM show accurate results, while the other three methods, WSEM, FEM and RM, suffer from inexact fluorescence simulation due to the finite size of the volume elements. The results of the total remitted fluorescence light were similar for the DEM, WDEM, FEM and RM. Deviations <20% of the total remitted fluorescence light between the WSEM and the other four methods were found, which may be a consequence of launching the fluorescence photons at a point inside each volume element instead of using the accurate fluorescence source distribution. It can be assumed that deviations of the remitted fluorescence light distribution at small radial distances from the source are especially caused by this issue. In addition, the number of volume elements is limited, and fluorescence photons excited outside this volume are not considered. This leads to the increased deviations of the total remitted fluorescence light and of the remitted fluorescence light distribution at large distances from the source.

For a sufficiently large number of photons, the methods FEM and RM were found to yield undistinguishable results. However, both methods showed deviations from the exact methods, DEM and WDEM, when comparing the remitted fluorescence $F(r)$. In addition to the deviations also found for the WSEM, the convolution causes additional imprecisions at distances far from the source, as for the convolution, both the excitation light distribution and the detection probability are assumed to drop to zero outside the considered volume [19].

Compared to the DEM, the WDEM performed faster for all sets of optical parameters, which is assumed to originate from the weighted simulation approach. Both, the FEM and the RM are faster than the DEM for all sets of optical parameters, with the RM outperforming all other methods. Compared to the WSEM, where $n_r \cdot n_z$ fluorescence photon emission points are simulated, in the FEM the number of simulations required is reduced to the number of volume elements in z-direction, n_z, decreasing the total simulation time. The gain of speed of the RM can be explained by the fact that in this RM, only fluorescence photons that actually reach the tissue surface are simulated, avoiding unnecessarily simulated photons. This method can also be applied to more complex geometries [6], however in these cases, only the amount of fluorescence light incident on a defined detector is simulated, and not the remitted fluorescence light distribution. In this case, the convolution is replaced by a sum over the product of the excitation light distribution and the fluorescence detection probability for each volume element. Therefore, by properly defining the fluorescence photon emission from the detector, the RM can be implemented into MC simulation programs that evaluate the volume light distribution [16,34]. Finally, the WSEM is slower on average than the DEM for simulation of fluorescence light. The reason is assumed to be that the number of calculated fluorescence photons does not decrease with increasing depth of emission position, whereas these photons hardly contribute to the remitted fluorescence signal.

An overview of a comparison of the different methods, in terms of speed and accuracy, is shown in Table 4. The first column indicates qualitatively the average speed of each method for the 18 sets of optical parameters, where high speed is indicated by "++" and low speed by "−−". The second column indicates qualitatively the accuracy of each method, where only the DEM and the WDEM yield exact results ("+"). The WSEM suffers from deviations due to finite voxel size ("0"). The FEM and the RM

Table 4. Comparison of the Results for the Different Methods

	Speed[a]	Accuracy[b]
DEM	−	+
WDEM	0	+
WSEM	−−	0
FEM	+	−
RM	++	−

[a]The average speed for simulation of the remitted fluorescence light distribution for 18 different sets of optical parameters, with "++" indicating very fast and "−−" very slow simulations.

[b]The DEM and WDEM yield accurate results ("+"), the FEM and RM suffer from additional convolution imprecisions ("−") compared to the WSEM ("0").

additionally show deviations from the exact solution due to convolution imprecisions ("–").

The WDEM was implemented for simulations using CPU and GPUs. A significant speed improvement of more than two orders of magnitude was achieved when performing simulations on a low-cost consumer graphic card which is in the range reported in the literature [16,25]. Currently, consumer graphic cards are limited to single precision floating point operations, which does not significantly reduce the precision of photon propagation simulations [25]. GPU simulations can be easily used for both simulation steps used in the RM, further accelerating this method. As this is expected to yield additional acceleration by at least two orders of magnitude, the speed of the convolutions is assumed to be the limiting factor concerning the overall simulation speed. Therefore, fast convolution techniques such as the DHT for radially symmetric functions should be considered for further acceleration of simulations.

5. Conclusion

To put the whole matter into a nutshell, the WDEM is recommended for fluorescence simulations if high accuracy is required, and the RM is recommended if extremely high speed simulations have to be performed, albeit with limited accuracy. Parallelized GPU simulations on low-cost consumer graphic cards bare the potential to further increase simulation speed by at least two orders of magnitude.

Appendix A: Abbreviations

MC	Monte Carlo
CPU	Central processing units
GPU	Graphics processing unit
MCML	A Monte Carlo model of steady-state light transport in multi-layered tissues
GPUMCML	GPU port of MCML
DEM	Direct emission method
WDEM	Weighted direct emission method
WSEM	Weighted separated emission method
FEM	Forward emission method
RM	Reverse method
LOW	Set of optical parameters with low scattering coefficients
HIGH	Set of optical parameters with high scattering coefficients
GSL	GNU scientific library
DHT	Discrete Hankel transform

†This manuscript is part of the inaugural thesis of Georg Hennig to be submitted at the Medical Faculty of the Ludwig-Maximilians-Universität.

References

1. J. Hegyi, V. Hegyi, T. Ruzicka, P. Arenberger, and C. Berking, "New developments in fluorescence diagnostics," J. Dtsch. Dermatol. Ges. **9**, 368–372 (2011).
2. Y. P. Sinichkin, N. Kollias, G. I. Zonios, S. R. Utz, and V. V. Tuchin, "Reflectance and fluorescence spectroscopy of human skin *in vivo*," in *Handbook of Optical Biomedical Diagnostics*, V. V. Tuchin, ed. (SPIE, 2002), pp. 725–785.
3. I. Georgakoudi, "The color of cancer," J. Lumin. **119–120**, 75–83 (2006).
4. H. Stepp, T. Beck, W. Beyer, C. Pfaller, M. Schuppler, R. Sroka, and R. Baumgartner, "Measurement of fluorophore concentration in turbid media by a single optical fiber," Med. Laser Appl. **22**, 23–34 (2007).
5. P. A. Valdes, A. Kim, F. Leblond, O. M. Conde, B. T. Harris, K. D. Paulsen, B. C. Wilson, and D. W. Roberts, "Combined fluorescence and reflectance spectroscopy for *in vivo* quantification of cancer biomarkers in low- and high-grade glioma surgery," J. Biomed. Opt. **16**, 116007 (2011).
6. G. Hennig, H. Stepp, and A. Johansson, "Photobleaching-based method to individualize irradiation time during interstitial 5-aminolevulinic acid photodynamic therapy," Photodiagnosis Photodyn. Ther. **8**, 275–281 (2011).
7. B. W. Pogue and G. Burke, "Fiber-optic bundle design for quantitative fluorescence measurement from tissue," Appl. Opt. **37**, 7429–7436 (1998).
8. S. Avrillier, E. Tinet, D. Ettori, J. M. Tualle, and B. Gelebart, "Influence of the emission-reception geometry in laser-induced fluorescence spectra from turbid media," Appl. Opt. **37**, 2781–2787 (1998).
9. K. Vishwanath, B. Pogue, and M. A. Mycek, "Quantitative fluorescence lifetime spectroscopy in turbid media: comparison of theoretical, experimental and computational methods," Phys. Med. Biol. **47**, 3387–3405 (2002).
10. N. Metropolis and S. Ulam, "The Monte Carlo method," J. Am. Stat. Assoc. **44**, 335–341 (1949).
11. A. J. Welch, C. Gardner, R. Richards-Kortum, E. Chan, G. Criswell, J. Pfefer, and S. Warren, "Propagation of fluorescent light," Lasers Surg. Med. **21**, 166–178 (1997).
12. V. V. Tuchin, "Methods and algorithms for the measurement of the optical parameters of tissues," in *Tissue Optics—Light Scattering Methods and Instruments for Medical Diagnosis*, V. V. Tuchin, 2nd ed. (SPIE, 2007), pp. 143–256.
13. S. A. Prahl, M. Keijzer, S. L. Jacques, and A. J. Welch, "A Monte Carlo model of light propagation in tissue," Proc. SPIE **IS 5**, 102–111 (1989).
14. B. C. Wilson and G. Adam, "A Monte Carlo model for the absorption and flux distributions of light in tissue," Med. Phys. **10**, 824–830 (1983).
15. L. Wang, S. L. Jacques, and L. Zheng, "MCML—Monte Carlo modeling of light transport in multi-layered tissues," Comput. Methods Programs Biomed. **47**, 131–146 (1995).
16. Q. Fang and D. A. Boas, "Monte Carlo simulation of photon migration in 3D turbid media accelerated by graphics processing units," Opt. Express **17**, 20178–20190 (2009).
17. R. J. Crilly, W. F. Cheong, B. Wilson, and J. R. Spears, "Forward-adjoint fluorescence model: Monte Carlo integration and experimental validation," Appl. Opt. **36**, 6513–6519 (1997).
18. S. L. Jacques, "Monte Carlo simulations of fluorescence in turbid media," in *Handbook of Biomedical Fluorescence*, M. A. Mycek and B. W. Pogue, eds. (Marcel-Dekker, 2003).
19. J. Swartling, A. Pifferi, A. M. Enejder, and S. Andersson-Engels, "Accelerated Monte Carlo models to simulate fluorescence spectra from layered tissues," J. Opt. Soc. Am. A **20**, 714–727 (2003).
20. D. Arifler, R. A. Schwarz, S. K. Chang, and R. Richards-Kortum, "Reflectance spectroscopy for diagnosis of epithelial precancer: model-based analysis of fiber-optic probe designs to resolve spectral information from epithelium and stroma," Appl. Opt. **44**, 4291–4305 (2005).
21. A. A. Tanbakuchi, A. R. Rouse, and A. F. Gmitro, "Monte Carlo characterization of parallelized fluorescence confocal systems imaging in turbid media," J. Biomed. Opt. **14**, 044024 (2009).
22. A. Kienle and M. S. Patterson, "Determination of the optical properties of turbid media from a single Monte Carlo simulation," Phys. Med. Biol. **41**, 2221–2227 (1996).
23. A. Liebert, H. Wabnitz, N. Zolek, and R. Macdonald, "Monte Carlo algorithm for efficient simulation of time-resolved fluorescence in layered turbid media," Opt. Express **16**, 13188–13202 (2008).
24. S. L. Jacques and L. Wang, "(MCML) Monte Carlo for multilayered media" (1992), retrieved Jan 20, 2011, http://omlc.ogi.edu/software/mc/.

25. E. Alerstam, W. C. Lo, T. D. Han, J. Rose, S. Andersson-Engels, and L. Lilge, "Next-generation acceleration and code optimization for light transport in turbid media using GPUs," Biomed. Opt. Express **1**, 658–675 (2010).
26. S. L. Jacques, "mcsubfluor.c" (2011), retrieved Sep 22, 2011, http://omlc.ogi.edu/software/mc/mcfluor/index.html.
27. G. M. Palmer and N. Ramanujam, "Monte-Carlo-based model for the extraction of intrinsic fluorescence from turbid media," J. Biomed. Opt. **13**, 024017 (2008).
28. D. J. Cuccia, F. Bevilacqua, A. J. Durkin, F. R. Ayers, and B. J. Tromberg, "Quantitation and mapping of tissue optical properties using modulated imaging," J. Biomed. Opt. **14**, 024012 (2009).
29. N. Baddour, "Operational and convolution properties of two-dimensional Fourier transforms in polar coordinates," J. Opt. Soc. Am. A **26**, 1767–1777 (2009).
30. L. G. Henyey and J. L. Greenstein, "Diffuse radiation in the galaxy," Astrophys. J. **93**, 70–83 (1941).
31. A. Averbuch, R. R. Coifman, D. L. Donoho, M. Elad, and M. Israeli, "Fast and accurate polar Fourier transform," Appl. Comput. Harmon. Anal. **21**, 145–167 (2006).
32. H. F. Johnson, "An improved method for computing a discrete Hankel transform," Comput. Phys. Commun. **43**, 181–202 (1987).
33. "GSL—GNU scientific library—discrete Hankel transforms" (Free Software Foundation, Inc., 2010), retrieved Feb 11, 2011, http://www.gnu.org/software/gsl/manual/html_node/Discrete-Hankel-Transforms.html.
34. Q. Fang, "Mesh-based Monte Carlo method using fast ray-tracing in Plucker coordinates," Biomed. Opt. Express **1**, 165–175 (2010).

BANDWIDTH-VARIABLE TUNABLE OPTICAL FILTER UNIT FOR ILLUMINATION AND SPECTRAL IMAGING SYSTEMS USING THIN-FILM OPTICAL BAND-PASS FILTERS

GEORG HENNIG, GARY M. BRITTENHAM, RONALD SROKA,
GESA KNIEBÜHLER, MICHAEL VOGESER UND HERBERT STEPP

Review of Scientific Instruments **84 (4)**, 0431131-1–0431131-7 (2013)

Bandwidth-variable tunable optical filter unit for illumination and spectral imaging systems using thin-film optical band-pass filters

Georg Hennig,[1,a)] Gary M. Brittenham,[2] Ronald Sroka,[1] Gesa Kniebühler,[1] Michael Vogeser,[3] and Herbert Stepp[1]
[1]*Laser-Forschungslabor, LIFE Center, Klinikum der Universität München, Marchioninistr. 23, 81377 München, Germany*
[2]*Division of Pediatric Hematology, Oncology and Stem Cell Transplant, Department of Pediatrics, Columbia University College of Physicians and Surgeons, 3959 Broadway, New York, New York 10032, USA*
[3]*Institute of Laboratory Medicine, Klinikum der Universität München, Marchioninistr. 15, 81377 München, Germany*

(Received 7 March 2013; accepted 12 April 2013; published online 30 April 2013)

An optical filter unit is demonstrated, which uses two successively arranged tunable thin-film optical band-pass filters and allows for simultaneous adjustment of the central wavelength in the spectral range 522–555 nm and of the spectral bandwidth in the range 3–16 nm with a wavelength switching time of 8 ms/nm. Different spectral filter combinations can cover the complete visible spectral range. The transmitted intensity was found to decrease only linearly with the spectral bandwidth for bandwidths >6 nm, allowing a high maximum transmission efficiency of >75%. The image of a fiber bundle was spectrally filtered and analyzed in terms of position-dependency of the transmitted bandwidth and central wavelength. © *2013 AIP Publishing LLC*. [http://dx.doi.org/10.1063/1.4803003]

I. INTRODUCTION

Optical filtering is a common task in laboratory or clinical light applications such as illumination and detection systems,[1] e.g., for fluorescence spectroscopy. It is also necessary for spectral imaging,[2,3] e.g., for filtering images from fiber bundles used in endoscopy or for fluorescence microscopy. Often, it is desired to be able to quickly switch between different central wavelengths at a small spectral bandwidth, without requiring tunable lasers or other expensive equipment. Diffraction-based monochromators, e.g., Czerny-Turner type grated monochromators,[4] are commonly used for non-imaging spectrometers.[1,2] For this type of monochromator, the transmitted intensity decreases with decreasing bandwidth in a greater than linear manner that is approximately proportional to the square of the bandwidth for a given light source diameter,[1] limiting its applicability to high intensity illumination systems. For spectral imaging, diffraction-based monochromators require a scanning unit,[2] which is a limitation that can be overcome by using other filter types such as acousto-optic tunable filters,[2,5,6] linear variable optical filters,[2,5,7,8] or liquid-crystal tunable filters.[2,5,9,10] For most of these filter types, however, either bandwidth or central wavelength can be adjusted, but not both,[6,11] the tuning range of the bandwidth or central wavelength may be limited,[7,12] or the transmission characteristics depend on the position of the incident light on the filter.[7,8]

Cholesteric liquid crystals (CLCs) exhibit reflection properties that depend on the angle of incidence, polarization, electrical or magnetic field, temperature, radiation, or mechanical pressure.[13–18] CLCs were used to demonstrate optical filter units that allow for simultaneous adjustment of the central wavelength and spectral bandwidth.[15,16] The polarization-dependent reflection efficiency limits the transmission efficiency of these demonstrated filter units to less than 45%,[15,16] which may be improved by combining crystals with different polarization dependency.[16] However, for these filter units, light suppression outside the transmitted pass-band is limited.[15,16] When tuning the wavelength by the angle of incidence, the transmitted beam of light is displaced due to the reflection geometry, making optical alignment cumbersome.[15,16] This is not the case when tuning the filters by temperature adjustment[16] instead of rotating the filters. Nonetheless, temperature adjustment is time consuming and therefore yields only a slow tuning speed of 0.39 s/nm.[16]

An optical filter unit that overcomes some of these limitations uses the same concept of independent adjustment of overlapping filter pass-bands:[15,19] two commercially available thin-film optical band-pass filters in a transmission setup[12,19] are successively arranged for simultaneous adjustment of both the central wavelength and the transmission bandwidth. A single tunable thin-film filter shows a transmission efficiency of more than 90% in the pass-band,[5] whose central wavelength shifts upon rotation of the filter. The spectral bandwidth remains virtually constant and, in particular, is independent of the polarization of the transmitted light,[3,5,19] so that the transmission efficiency in the pass-band remains virtually constant as well. If two such filters are arranged successively, an independent rotation of the filters to different angles spectrally shifts the filter pass-bands against each other, and light is transmitted through the filter unit only in the spectral range where the filter pass-bands overlap. Even when tuning the filter unit to different central wavelengths with a fixed bandwidth, the two filters must be rotated independently due to the nonlinear relation between the central wavelength

a)Author to whom correspondence should be addressed. Electronic mail: georg.hennig@med.lmu.de. This paper is part of the inaugural thesis of Georg Hennig to be submitted at the Medical Faculty of the Ludwig-Maximilians-Universität.

of the transmitted pass-band and the angle of incidence, compare Eq. (1) and Fig. 3. In contrast to reflection filters,[15] no angular deviation occurs when rotating the filters, moreover preserving the fast tuning speed of the filter unit that is tuned by the angle of incidence.[15] A parallel beam shift occurs when light passes through the rotated filters,[19] which may be compensated at least partly by rotating the filters in opposite directions, so that the beam shifted by the first filter is partly shifted back by the second filter. The maximum transmission efficiency is found in the center of the spectral range where the filter pass-bands overlap. This maximum transmission efficiency equals the product of the transmission efficiencies of both filters at their respective spectral positions. Therefore, if both filters show high transmission efficiency in the overlapping pass-band, the product of the two transmission efficiencies is high and independent of the bandwidth of the overlapping spectral range. However, to achieve a very small bandwidth, only the edges of the two filter pass-bands overlap. In this case, the maximum transmission efficiency is lower. Altogether, the transmission efficiency of the filter unit can be expected to not depend on the bandwidth, as long as the minimal achievable bandwidth is not limited by the filter edge steepness. The transmitted intensity of light depends on the area under the total transmitted pass-band that decreases in this case only linearly with the optical bandwidth in contrast to diffraction-based monochromators, indicating the applicability of the filter unit to high intensity illumination systems. Additionally, the band-pass filters used in the demonstrated filter unit are, in principle, capable of filtering images without the need of scanning units.[3,12] This can be done by filtering the image in a collimated beam.[12] However, photons from different positions in the focal plane show different divergence angles in the collimated beam and therefore different angles of incidence on the rotated filters. These differences lead to different spectral shifts of the filter pass-bands, so that the filtering characteristics of the filter unit can be assumed to depend on the position of the light source within the focal plane. The remaining divergence angle of a collimated beam is smaller for a larger focal width, so that the filtering characteristics of the filter unit can also be assumed to depend on the focal width of the collimating lens.

In this study, a filter unit combining two identical tunable thin-film optical band-pass filters with their pass-bands in the green wavelength range (central wavelength tuning range: 502–561 nm) is analyzed. To evaluate its applicability to high intensity illumination systems, white light from a 1500 μm core diameter fiber is spectrally filtered by the filter unit and coupled again into a 1500 μm core diameter fiber. The transmission characteristic of one filter is compared to the filter specifications and to the transmission achieved by the complete filter unit, consisting of two identical filters. The limits of the achievable tuning range and bandwidth variation are evaluated. The limitations of the filter unit when filtering images are demonstrated by filtering the collimated beam from 7 linearly arranged 200 μm core diameter fibers, comparing collimating lenses with different focal lengths, and measuring the spectrum of the transmitted light for each fiber for different directions of rotation of the filters.

II. MATERIAL AND METHODS

A. Tunable thin-film optical band-pass filters

Two tunable thin-film optical band-pass filters (561/14 nm VersaChrome®, Semrock, Inc., Rochester, NY, USA, filter size 25.2 mm × 35.6 mm × 2.0 mm, central wavelength $\lambda_C = 561$ nm at perpendicular angle of incidence $\theta = 0°$, and the effective refractive index $n_{eff} = 1.83$), were implemented for spectral filtering. The central transmission wavelength λ_C of the filters depends on the angle of incidence θ of the light beam relative to the surface normal of the filter and on the effective refractive index n_{eff}, which is particular for the tunable band-pass filter that is used. The angular dependency of λ_C can be described[3,5] by

$$\lambda_C(\theta) = \lambda_C(0)\sqrt{1 - \frac{\sin^2\theta}{n_{eff}^2}}. \quad (1)$$

B. Experimental setup

As shown schematically in Fig. 1(a), white light from a short-arc Xe-lamp (D-Light, Karl Storz GmbH & Co. KG, Tuttlingen, Germany) was coupled into a 1500 μm core diameter fiber (NA = 0.35, Karl Storz GmbH & Co. KG, Tuttlingen, Germany), referred to as the "source fiber." The white light from the source fiber was collimated by an aspherical condenser lens (D = 22.4 mm, f = 18 mm, LINOS system, Qioptiq Photonics GmbH & Co. KG, Göttingen, Germany), referred to as "collimating lens," with a remaining divergence angle of 2.1° of the collimated beam. Then, the collimated beam of white light passed through the two tunable thin-film optical band-pass filters, with the optical axis adjusted to the

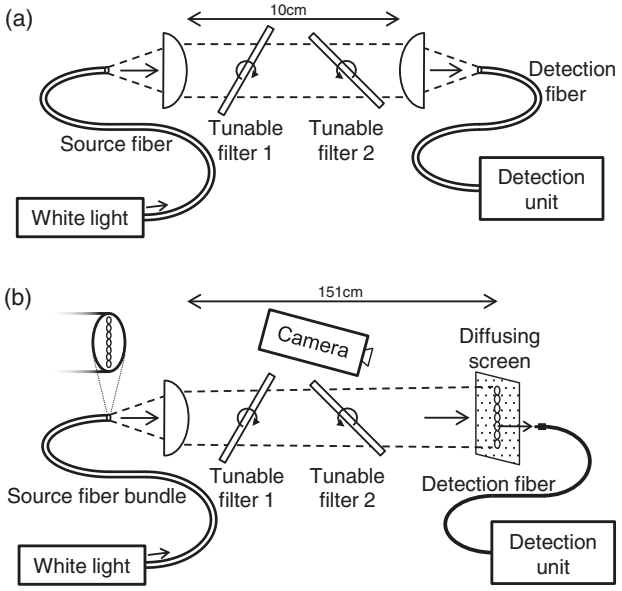

FIG. 1. Schematic of the measurement setup. (a) White light transmitted through a source fiber (1500 μm core diameter) is filtered by two independently tunable optical filters. The detection unit consists of a detection fiber (1500 μm core diameter), which is coupled into a CCD spectrometer. (b) A fiber bundle with 7 linearly arranged fibers (200 μm core diameter) served as source fiber, and the image of the fiber bundle on a diffusing screen is recorded by a camera. The spectrum of each fiber is acquired by the spectrometer.

center position of the filters. The filter mounts were coupled to two stepper motors (Nanotec Electronic GmbH & Co. KG, Landsham, Germany) so that they could be rotated individually using stepper motor controllers (SMCI32, Nanotec Electronic GmbH & Co. KG, Landsham, Germany), which were actuated by a custom interface (LabVIEW, National Instruments Corporation, Austin, TX, USA). One step equaled 1.8° with 16 microsteps per step, yielding an angular increment of 0.1125° per microstep. The time required for rotating a filter from $\theta = 0°$ to $\theta = 51°$ was 400 ms, yielding an effective response time of 8 ms/nm. Both filters could be removed independently from the filter unit to perform measurements either without or with one or two tunable filters. The filters could be rotated individually clockwise or counterclockwise, yielding rotation in opposite directions ("counter-directional") or the same direction ("equidirectional"). The parallel beam shift that occurs, when the collimated beam of light passes through the 2 mm thick filters rotated to different angles, can be estimated by theoretical considerations to be less than 200 μm for counter-directional rotation, while for equidirectional rotation, it is less than 1200 μm. After transmission through the filter unit (length: 10 cm, compare Fig. 1(a)), the filtered collimated beam of light was then focused by the "focusing lens," which was identical to the collimating lens, and focused onto a 1500 μm core diameter fiber (NA = 0.48, CeramOptec GmbH, Bonn, Germany), referred to as the "detection fiber." For spectrally resolved detection, the detection fiber was coupled into the detection unit, where the spectrum was detected by a CCD spectrometer (2048 pixel, 339-1029 nm, USB2000+, OceanOptics, Inc., Dunedin, FL, USA) with an effective spectral resolution of 2 nm.

To demonstrate the filter unit's ability to filter images, the image of a fiber bundle, consisting of 7 linearly arranged fibers (200 μm core diameter each, NA = 0.22, LightGuideOptics Germany GmbH, Rheinbach, Germany), was displayed on a reflecting diffusing screen (TiO_2 coated), which was located at a distance of 151 cm from the collimating lens, as shown schematically in Fig. 1(b). The axis along which the fibers were arranged was perpendicular to the filter rotation axis. The collimated 7 beams transmitted through the filter unit had a remaining divergence half angle of 2.6°. The image of the fiber bundle was recorded by a consumer grade camera (Ixus 970 IS, Canon, Inc., Tokyo, Japan). Additionally, the spectrum of the image of each fiber was acquired by the detection unit using a 50 μm core optical fiber (NA = 0.22, Thorlabs, Inc., Newton, NJ, USA).

To demonstrate the influence of the focal length of the collimating lens on the total transmission efficiency, the collimating lens with f = 18 mm was replaced by another aspherical condenser lens with f = 27 mm (D = 31.5 mm, LINOS system, Qioptiq Photonics GmbH & Co. KG, Göttingen, Germany), resulting in a reduced divergence half angle of 1.5° of the collimated beam.

C. Evaluation

The evaluation and graphical presentation of the recorded spectra was performed by MATLAB (R2012a, MathWorks®, Natick, MA, USA). First, a dark spectrum was subtracted from each recorded spectrum. The resulting spectrum was calibrated for the wavelength-dependent spectrometer sensitivity, yielding the calibrated "filtered spectrum." The evaluation of the transmission efficiency through one or two filters was performed by dividing the "filtered spectrum" by the spectrum of the light coupled into the detection fiber without any filter, yielding the "transmission spectrum." The maximum of this transmission spectrum was identified and is referred to as the "maximum transmission efficiency."

The evaluation of the spectral bandwidth of the transmitted pass-band was performed by first identifying the maximum intensity of the "transmission spectrum" and thereafter by iterating through the pixel values from the lowest and highest recorded wavelength towards the maximum and identifying the two spectral positions at each side of the pass-band, where the intensity was 50% of the maximum intensity, and finally by interpolating linearly between the two neighboring pixels in the spectrum. The resulting spectral width is referred to as the "spectral bandwidth" λ_{SB} (full width at half maximum, FWHM). The "central wavelength" λ_C of the transmitted pass-band was evaluated by calculating the center position between the two spectral positions at each side of the pass-band where 50% of the maximum intensity was reached. In a similar way, the edge steepness was quantified by evaluating the difference of the spectral positions, where 10% and 90% of the maximum intensity was reached, and averaging over both sides of the transmitted pass-band. The "transmitted intensity" was evaluated by calculating the sum over all pixels of the transmission spectrum within the spectral range 490–580 nm to cover the pass-band for the whole tuning range.

III. RESULTS

A. Single filter

In Fig. 2, the filtered spectrum of one filter at different filter angles θ is shown, relative to the transmitted light without any filter. The central wavelength λ_C shifts towards smaller wavelengths at increasing angles, while the spectral

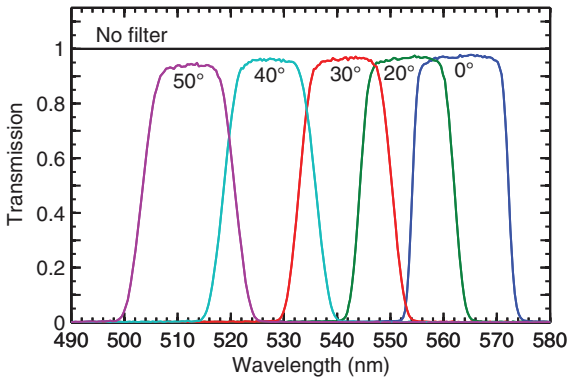

FIG. 2. The transmission spectrum, relative to the transmission without any filter, is shown for the setup in Fig. 1(a) with one tunable thin-film optical band-pass filter inserted at the filter rotation angles θ = [0°, 20°, 30°, 40°, 50°] shown below each transmission spectrum, with λ_C = [563.2 nm, 553.2 nm, 541.6 nm, 527.2 nm, 512.0 nm] and λ_{SB} = [18.1 nm, 17.8 nm, 17.6 nm, 17.4 nm, 17.5 nm].

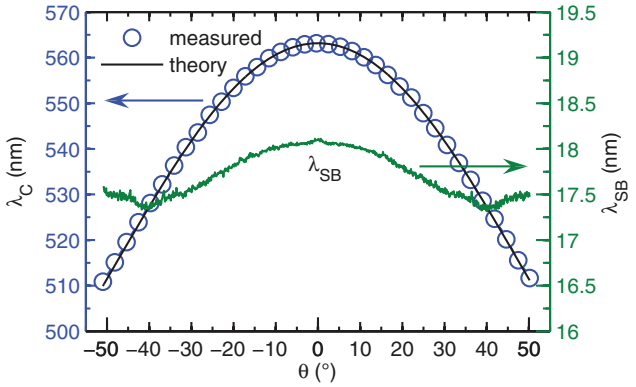

FIG. 3. The central wavelength λ_C (left y-axis) and bandwidth λ_{SB} (right y-axis) of the transmission spectrum using one tunable thin-film optical band-pass filter at different angles are shown, as well as the theoretically predicted central wavelength. The bandwidth varies only between 17.3 and 18.1 nm, while the central wavelength could be tuned between 510 nm and 563 nm.

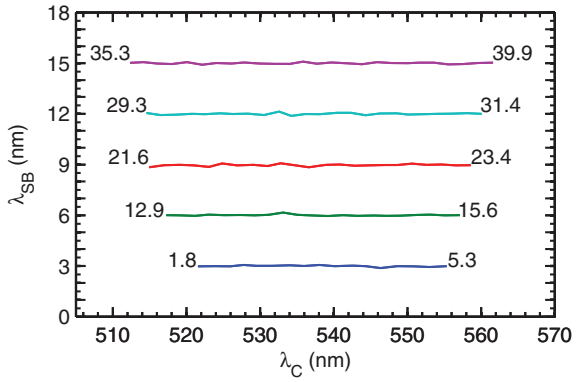

FIG. 5. The bandwidth of the transmitted light is plotted as a function of the transmitted central wavelength for five bandwidth settings, 3–15 nm (3 nm increments), demonstrating the freely adjustable central wavelength at defined bandwidth settings. The tuning range is limited by the bandwidth setting (maximum bandwidth setting range: 3 nm $\leq \lambda_{SB} \leq$ 16 nm). The transmitted intensity in arbitrary units is denoted for each bandwidth setting at the highest and lowest achievable central wavelength λ_C.

bandwidth λ_{SB} of the transmitted light remains virtually constant, although with flattened edges of the pass-band at increasing θ and decreasing λ_C (edge steepness: 2.1 nm for $\theta = 0°$, 5.3 nm for $\theta = 50°$). From the transmission spectrum, the maximum transmission efficiency was evaluated, being larger than 97% for $\theta = 0°$, and still larger than 94% for $\theta = 50°$.

The quantitative results of λ_C and λ_{SB} of the transmission pass-band of one filter at different θ are shown in Fig. 3. The measured λ_C follows the theoretical prediction of Eq. (1). By rotating the filter from $\theta = 0°$ to $\theta = 51°$, λ_C could be tuned from 563 nm to 510 nm. Angles $\theta > 51°$ could not be used, because parts of the parallel beam would have passed by the filters, which were only available in the size stated. λ_{SB} varied only by a small amount: the average bandwidth over the tuning range equaled $\lambda_{SB} = 17.7$ nm (range: 17.3–18.1 nm).

B. Two filters

The capability of the filter unit to independently adjust λ_C and λ_{SB} is illustrated in Fig. 4. The transmission spectrum

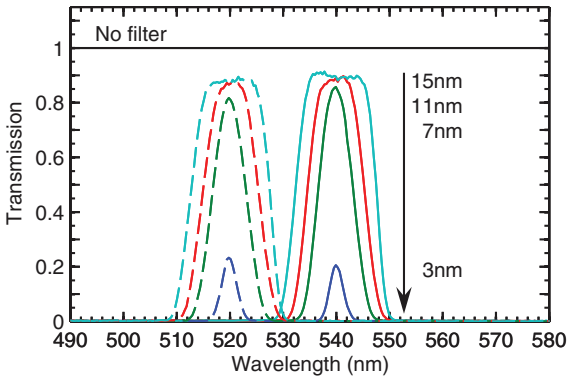

FIG. 4. The transmission spectrum with the two tunable thin-film filters is shown relative to the transmission spectrum without filters (solid black line). The two filters were rotated independently to transmit light only at the desired central wavelengths ($\lambda_C = 520$ nm and $\lambda_C = 540$ nm) with the desired bandwidths (3 nm $\leq \lambda_{SB} \leq$ 15 nm, 4 nm increments).

at 8 different angles of both filters is shown, yielding a transmitted central wavelength of 520 nm or 540 nm, at 4 different bandwidths from 3 nm to 15 nm. The maximum transmission remains nearly constant for $\lambda_{SB} \geq 9$ nm, but decreases for smaller bandwidths. For $\lambda_{SB} \geq 9$ nm, the maximum transmission efficiency was larger than 88% for $\lambda_C = 540$ nm and larger than 87% for $\lambda_C = 520$ nm, while for $\lambda_{SB} = 6$ nm, it was 81% for $\lambda_C = 540$ nm and 75% for $\lambda_C = 520$ nm.

For 5 bandwidths (3–15 nm), the bandwidth is plotted as a function of the central wavelength in Fig. 5, remaining virtually constant within the central wavelength range shown, demonstrating the ability to freely adjust the central wavelength at a given spectral bandwidth. However, the spectral tuning range of the central wavelength is limited by the bandwidth setting: the maximum rotation angle $\theta = 51°$ limits the pass-band shift of one filter to a minimal spectral position. To achieve a small total pass-band bandwidth, the other filter has to be rotated to an angle $\theta < 51°$, so that the central wavelength of the transmission pass-band of both filters increases with the bandwidth reduction, limiting the minimum achievable central wavelength at a given bandwidth. The same applies to the minimum rotation angle $\theta = 0°$, where the other filter is rotated to an angle $\theta > 0°$, decreasing the maximum achievable central wavelength at a given bandwidth. Therefore, for a bandwidth $\lambda_{SB} = 3$ nm, the tuning range was 522 nm $\leq \lambda_C \leq$ 555 nm, and for $\lambda_{SB} = 15$ nm, the range was 512 nm $\leq \lambda_C \leq$ 562 nm. Additionally, the quantitative evaluation of the transmitted intensity is shown in Fig. 5 for each bandwidth at the lowest and highest achievable central wavelength. In the bandwidth range 6 nm $\leq \lambda_{SB} \leq$ 15 nm, the transmitted intensity remains virtually constant for increased rotation angles. For the very small bandwidth $\lambda_{SB} = 3$ nm, the transmitted intensity is reduced by a factor of 3 for large rotation angles.

Finally, in Fig. 6, the transmitted intensity, i.e., the sum over all pixel values of the transmission spectrum, is plotted as a function of the bandwidth for 4 different central wavelengths, 520–550 nm. For all central wavelengths, essentially

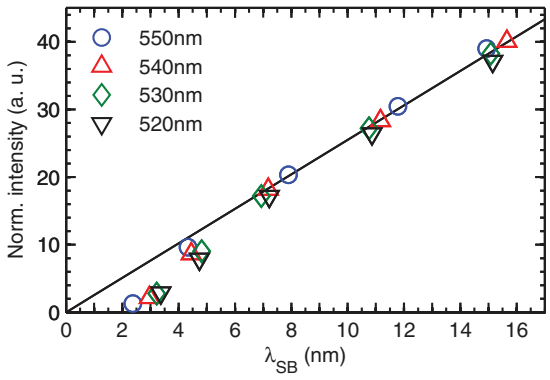

FIG. 6. The transmitted intensity, i.e., the sum over all pixel values of the transmission spectrum, is plotted as a function of the spectral bandwidth at four central wavelengths, in the range 520–550 nm. It is obvious that for a bandwidth $\lambda_{SB} > 6$ nm, the intensity increases linearly with the bandwidth, and for $\lambda_{SB} < 6$ nm with a larger slope.

the same characteristic was measured: for $\lambda_{SB} \geq 6$ nm, the intensity increases linearly with the bandwidth, while for $\lambda_{SB} < 6$ nm, the intensity drops to zero with a larger slope.

C. Fiber bundle

In Fig. 7(a), the spectrally filtered image of the fiber bundle, collimated using the collimating lens with f = 18 mm as illustrated in Fig. 1(b), is shown. The filters were set to

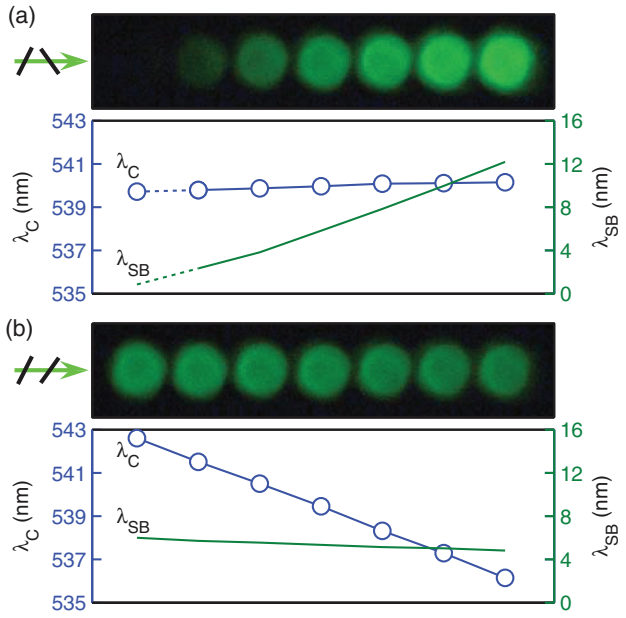

FIG. 7. The images of light transmitted through a linearly arranged fiber bundle focused onto a diffusing screen according to the setup in Fig. 1(b) is shown, for (a) counter-directional and (b) equidirectional rotating filters. The position-dependent central wavelength λ_C and bandwidth λ_{SB} of the filtered spectrum is shown for both cases. In (a), the central wavelength λ_C remained virtually constant (range: 539.8–540.1 nm), while the bandwidth λ_{SB} varied spatially (range: 2.3–12.2 nm). For the outermost left fiber, the transmitted intensity was too low for evaluation, so the bandwidth and central wavelength is indicated only by extrapolating the neighboring values. In (b), the central wavelength λ_C varied spatially (range: 542.6–536.1 nm), while the bandwidth λ_{SB} varied only by a smaller amount (range: 6.0–4.7 nm).

counter-directional rotation angles, +26.8° and −35.7°, respectively, yielding a central wavelength $\lambda_C = 540$ nm and a spectral bandwidth $\lambda_{SB} = 6$ nm for the center fiber of the fiber bundle. In the image, it is obvious that for the outermost left fiber virtually no light was transmitted, while for the outermost right fiber, the intensity was larger than for the central fiber. Below the image in Fig. 7(a), the filtered spectrum is shown for each single fiber. While λ_C remained virtually constant for all fibers (range: 539.8–540.1 nm), λ_{SB} varied spatially in the range 2.3–12.2 nm. Due to the low transmitted intensity, the first fiber was excluded from this evaluation, and is only indicated by extrapolation of the neighboring values.

In Fig. 7(b), the two filters were set to equidirectional rotation angles, +26.8° and +35.7°, respectively. Here, the intensity variations observed in the fiber images are considerably lower. However, the evaluation of the transmitted spectrum shows that, in contrast to counter-directional rotation, λ_C varied spatially (range: 542.6–536.1 nm), while λ_{SB} showed only a low variation (range: 6.0–4.7 nm). The same behavior was found for other central wavelengths of the central fiber, 520 nm, 530 nm, and 550 nm. The quantitative evaluation of the minimum and maximum central wavelength and bandwidth of the 7 fibers for counter- and equidirectional rotation and for the different central wavelengths is shown in Table I. In addition, the results of the same measurements, performed with a collimating lens with a focal length of f = 27 mm, are shown in Table I. Essentially, the following result was observed: for a decreasing central wavelength which equals an increasing rotation angle, the variations observed between the different fibers became larger, namely, bandwidth variations for counter-directional rotation and central wavelength variations for equidirectional rotation. For example, for counter-directional rotation with the central wavelength set to 520 nm for the central fiber, the bandwidth varied from 2.2 nm to 13.1 nm (=10.9 nm variation), while for the central wavelength 550 nm of the central fiber, the bandwidth varied only from 2.8 nm to 10.9 nm (=8.1 nm variation). On the other hand, for equidirectional rotation, the central wavelength varied for the 520 nm central fiber setting from 516.3 nm to 523.6 nm (=7.3 nm variation), while it varied only from 546.8 nm to 551.9 nm (=5.1 nm variation) for the 550 nm wavelength setting. When using the collimating lens with larger focal length (f = 27 mm instead of f = 18 mm), in all cases, the observed variations became smaller, namely, bandwidth variations for counter-directional rotation, and central wavelength variations for equidirectional rotation.

IV. DISCUSSION

In this study, we demonstrated a cost-effective optical filter unit that allows for fast and independent adjustment of the central wavelength in the range 522–555 nm and of the spectral bandwidth in the range 3–16 nm. Images can be filtered without requiring a scanning unit. The filter unit offers potential replacement for expensive light sources such as tunable lasers in devices where a spectral bandwidth larger than 3 nm is acceptable.

TABLE I. Minimum and maximum transmitted central wavelength λ_C and bandwidth λ_{SB} for each of the 7 fibers of the fiber bundle at different central wavelengths.

			$\lambda_C = 550$ nm[a]		$\lambda_C = 540$ nm		$\lambda_C = 530$ nm		$\lambda_C = 520$ nm	
			C[b]	E[b]	C	E	C	E	C	E
Lens 1[c]	λ_C	Min	549.6	546.8	539.8	536.1	529.9	525.7	519.8	516.3
f = 18 mm		Max	550.4	551.9	540.1	542.6	530.0	532.8	520.0	523.6
	λ_{SB}	Min	2.8	4.1	2.3	4.8	2.2	4.7	2.2	6.1
		Max	10.9	6.3	12.2	6.0	12.6	5.2	13.1	6.2
Lens 2[c]	λ_C	Min	549.6	548.6	539.7	537.9	529.8	527.8	519.9	517.7
f = 27 mm		Max	550.3	551.8	540.1	542.1	530.0	532.4	519.9	522.5
	λ_{SB}	Min	3.1	6.1	2.7	6.4	2.4	6.6	2.5	7.3
		Max	9.6	7.3	10.6	6.9	10.8	6.8	11.6	7.5

[a]Filter angles were adjusted so that the image of the central fiber showed the indicated central wavelength and a bandwidth of 6 nm for counter-directional rotation of the filters.
[b]Counter-directional rotation of the filters ("C") and equidirectional rotation of the filters ("E").
[c]For the collimating lens 1 (f = 18 mm), the first fiber was not evaluated, for the collimating lens 2 (f = 27 mm), all fibers were evaluated.

The measurements using one tunable optical band-pass filter (561/14 nm VersaChrome, Semrock, Inc., Rochester, NY, USA) show that the central wavelength can be adjusted by rotating the filter as predicted by Eq. (1). The tuning range is limited by the geometry of the filter, as the projected filter area apparent to the collimated beam of light is reduced by rotating the filter. The pass-band edges are flattened at increasing θ by 3.2 nm, which can be assumed to be due to the remaining divergence of the collimated beam of light, which has a larger influence at larger θ, because of the stronger wavelength-dependency. The filter transmission remains well above 90% for the whole tuning range, indicating a negligible influence of incident light polarization. These filters are therefore potentially useful for high-intensity illumination systems filtering unpolarized white light or for highly efficient fluorescence detection systems.

Two successively arranged optical band-pass filters were used to allow for simultaneous adjustment of the transmitted central wavelength and bandwidth, which is achieved by spectral overlap of the two pass-bands that are shifted against each other by rotating the filters independently to different angles. We showed that in the described setup, the spectral bandwidth can be freely adjusted in the range 3–16 nm, with the tuning range of the central wavelength depending on the desired bandwidth, e.g., 522–555 nm for $\lambda_{SB} = 3$ nm and 512–562 nm for $\lambda_{SB} = 15$ nm. However, when using different filter combinations, in principle the complete visible wavelength range can be covered.[5] The adjustable bandwidth range agrees well with the one reported by Jeong *et al.*,[19] where a tuning range of 4–17.4 nm was achieved, however using a point-like source instead of the 1500 μm diameter fiber used in this study. Additionally, we showed in this study that the transmitted intensity decreases only linearly with the bandwidth for $\lambda_{SB} \geq 6$ nm, thus allowing optical filtering with a high transmission efficiency >75%, which indicates that the proposed arrangement of two tunable thin-film optical band-pass filters can be used without significant transmission efficiency loss compared to the one-filter setup. Especially, for high-intensity illumination systems, the proposed filter unit is superior to commonly used diffraction based monochromators, which show a decreasing maximum transmission efficiency at decreasing bandwidth, resulting in a decrease of the transmitted intensity by the square of the bandwidth.[1] However, for $\lambda_{SB} < 6$ nm, the maximum transmission efficiency of the proposed filter unit decreases as well. This decline can be attributed to the non-perfect parallelism of the collimated beam of light, which reduces the transmission pass-band edge steepness of each filter. Consequently, the total transmission efficiency is reduced if the filter pass-bands only overlap in the spectral range of the edges, thus limiting its use for very small spectral bandwidths. This problem cannot be overcome easily, as it requires either a source with smaller diameters, e.g., point-source like,[19] which may not be available as a high intensity non-coherent light source, or a larger focal width of the collimating lens, which is also not always applicable due to the usually high numerical aperture of the source, which would then result in a low transmission efficiency. Also, the filter dimensions restrict the beam diameter and therefore the collimating lens diameter, which limits the focal length at a given numerical aperture. Due to the size of the filters and the need to independently rotate them by $\theta < 60°$, the optical length of the filter unit theoretically has a lower limit of 62 mm to avoid collision of the rotated filters, which cannot be reduced without using smaller filters which would further restrict the beam diameter. The time required for switching between different filter settings is limited by the speed of the stepper motors driving the filter rotation, and was 400 ms for switching from lowest to highest rotation angle, and accordingly less for smaller spectral shifts, with a response time of less than 8 ms/nm. The parallel beam shift occurring during the propagation of the collimated beam through the filter unit can be minimized by rotating the filters into opposite directions. By focusing the collimated beam, the large beam shift can also be eliminated.[19] In such applications, equidirectional filter rotation can be used as well.

By showing spectrally filtered images of a linearly arranged fiber bundle, Fig. 7, we demonstrated the applicability of the filter unit to filtering images. The transmitted spectrum depends on the position within the image plane, along the axis perpendicular to the rotation axis of the filters. By rotating the filters in opposite directions, the central bandwidth is constant within the image along the axis perpendicular

to the filter rotation axis, but the bandwidth varies, e.g., 2–13 nm at the constant central wavelength of 540 nm, thereby producing intensity variations within the image. In contrast, by rotating the filters in the same direction, the bandwidth and therefore the intensity remains nearly constant along this axis, but the central wavelength shifts, e.g., from 536 nm to 543 nm, while the bandwidth varies only in the range 5–6 nm. This behavior can be explained by the transmission spectrum of a single filter, Fig. 2: the non-parallel parts of the collimated beam pass through the first filter position-dependent at a larger (or smaller) angle of incidence than the filter rotation angle, which effectively shifts the transmitted spectrum to shorter (or longer) wavelengths for these non-parallel parts of the beam. If both filters are rotated in opposite directions, the transmission pass-band of the second filter is shifted in the opposite direction; if they are rotated in the same direction, the transmission pass-band of the second filter is shifted in the same direction. Therefore, for counter-directional rotation, the total transmission bandwidth narrows for the non-parallel parts of the collimated beam due to a shift of the filter pass-bands in opposite directions, and for equidirectional rotation, the central wavelength shifts due to the pass-bands' shift in the same direction. The results confirm that this effect is more pronounced for decreasing central wavelengths, which is equivalent to increasing rotation angles, because the filter pass-bands shift by a larger amount at larger angles of incidence for a constant divergence angle. Compare Fig. 3 and Eq. (1), where the slope of the central wavelength function is larger for larger filter rotation angles. By using a longer focal length of the collimating lens, e.g., 27 mm instead of 18 mm, the non-parallel parts of the beam show a smaller divergence angle, which reduces the position-dependency of the transmitted central wavelength or spectral bandwidth in the image. For an even longer focal length, f = 80 mm, Iga *et al.*[12] filtered an image in a similar setup and varied the bandwidth from 1.5 nm to 3 nm, however, without specifying the position-dependency of the bandwidth or central wavelength within the image. For imaging systems, if this problem is predominant, e.g., when using a small focal length, this problem could be addressed by using equidirectional rotation of the filters, and by successively taking pictures while sweeping the filter unit over the tuning range at the desired bandwidth. In each picture, different parts can be assumed to be associated with different central wavelengths but identical bandwidth. We hypothesize that a composite picture with defined central wavelength and bandwidth could be reconstructed from this stack of pictures. Nevertheless, a careful specification of the position-dependent transmission characteristic of the filter unit is mandatory.

V. CONCLUSION

We conclude that tunable thin-film optical band-pass filters can be used for illumination systems with high wavelength tuning speed, where high intensities at small spectral bandwidths (3–16 nm) are required, if the tuning range (e.g., 522–555 nm) is sufficient for the application or it is acceptable to replace the filters to cover the whole visible spectral range. Spectral filtering of images or fiber bundles without a scanning unit is possible, which may be useful for imaging systems like microscopes or endoscopes, but may be limited by the divergence of the collimated beam. Careful specification of the filter unit in the imaging system is recommended.

ACKNOWLEDGMENTS

The authors thank Mr. Thomas Pongratz for technical support and Mr. Sebastian Fiedler for assistance during the measurements.

[1] J. R. Lakowicz, *Principles of Fluorescence Spectroscopy* (Springer, New York, 2006), p. 27.
[2] Y. Garini, I. T. Young, and G. McNamara, Cytometry, Part A **69A**, 735 (2006).
[3] P. Prabhat, N. Anderson, and T. Erdogan, Semrock White Paper Series (Semrock, Inc., 2012), see http://www.semrock.com/spectral-imaging-with-versachrome.aspx.
[4] M. Czerny and A. F. Turner, Z. Phys. **61**, 792 (1930).
[5] T. Erdogan and L. Wang, Semrock White Paper Series (Semrock, Inc., 2010), see http://www.semrock.com/semrock-versachrome-tunable-bandpass-filters.aspx.
[6] E. Dekemper, N. Loodts, B. Van Opstal, J. Maes, F. Vanhellemont, N. Mateshvili, G. Franssens, D. Pieroux, C. Bingen, C. Robert, L. De Vos, L. Aballea, and D. Fussen, Appl. Opt. **51**, 6259 (2012).
[7] P. E. Buchsbaum and J. D. Lane, "Tunable variable bandpass optical filter," U.S. patent 6,700,690 (2 March 2004).
[8] A. Emadi, H. Wu, G. de Graaf, P. Enoksson, J. H. Correia, and R. Wolffenbuttel, Appl. Opt. **51**, 4308 (2012).
[9] S. T. Wu, Appl. Opt. **28**, 48 (1989).
[10] S. C. Gebhart, R. C. Thompson, and A. Mahadevan-Jansen, Appl. Opt. **46**, 1896 (2007).
[11] Y. H. Chen, C. T. Wang, C. P. Yu, and T. H. Lin, Opt. Express **19**, 25441 (2011).
[12] M. Iga, N. Kakuryu, T. Tanaami, J. Sajiki, K. Isozaki, and T. Itoh, Rev. Sci. Instrum. **83**, 103707 (2012).
[13] M. Mitov, Adv. Mater. **24**, 6260 (2012).
[14] S. Furumi, S. Yokoyama, A. Otomo, and S. Mashiko, Appl. Phys. Lett. **84**, 2491 (2004).
[15] Y. Huang and S. Zhang, Opt. Lett. **36**, 4563 (2011).
[16] Y. Huang and S. Zhang, Appl. Opt. **51**, 5780 (2012).
[17] A. Chanishvili, G. Chilaya, G. Petriashvili, R. Barberi, R. Bartolino, G. Cipparrone, A. Mazzulla, and L. Oriol, Appl. Phys. Lett. **83**, 5353 (2003).
[18] H. P. Yu, B. Y. Tang, J. H. Li, and L. Li, Opt. Express **13**, 7243 (2005).
[19] H. J. Jeong, J. W. Ahn, D. Do, and D. G. Gweon, Rev. Sci. Instrum. **83**, 093705 (2012).

DUAL-WAVELENGTH EXCITATION FOR FLUORESCENCE-BASED QUANTIFICATION OF ZINC PROTOPORPHYRIN IX AND PROTOPORPHYRIN IX IN WHOLE BLOOD

GEORG HENNIG, CHRISTIAN GRUBER, MICHAEL VOGESER, HERBERT STEPP, STEPHAN DITTMAR, RONALD SROKA UND GARY M. BRITTENHAM

Journal of Biophotonics, doi: 10.1002/jbio.201200228 (2013)

Early View publication on
www.wileyonlinelibrary.com
(issue and page numbers not yet assigned;
citable using Digital Object Identifier – **DOI**)

J. Biophotonics 1–11 (2013) / **DOI** 10.1002/jbio.201200228

Journal of BIOPHOTONICS

FULL ARTICLE

Dual-wavelength excitation for fluorescence-based quantification of zinc protoporphyrin IX and protoporphyrin IX in whole blood

Georg Hennig[*,1], *Christian Gruber*[1], *Michael Vogeser*[2], *Herbert Stepp*[1], *Stephan Dittmar*[1], *Ronald Sroka*[1], *and Gary M. Brittenham*[3]

[1] Laser-Forschungslabor, LIFE Center, Klinikum der Universität München, Marchioninistr. 23, 81377 München, Germany
[2] Institute of Laboratory Medicine, Klinikum der Universität München, Marchioninistr. 15, 81377 München, Germany
[3] Division of Pediatric Hematology, Oncology and Stem Cell Transplantation, Department of Pediatrics, Columbia University College of Physicians and Surgeons, 3959 Broadway, New York, NY 10032, USA

Received 28 November 2012, revised 29 January 2013, accepted 12 February 2013
Published online 4 March 2013

Key words: fluorescence, zinc protoporphyrin, protoporphyrin IX, blood, spectrum analysis

Quantification of erythrocyte zinc protoporphyrin IX (ZnPP) and protoporphyrin IX (PPIX), individually or jointly, is useful for the diagnostic evaluation of iron deficiency, iron-restricted erythropoiesis, lead exposure, and porphyrias. A method for simultaneous quantification of ZnPP and PPIX in unwashed blood samples is described, using dual-wavelength excitation to effectively eliminate background fluorescence from other blood constituents. In blood samples from 35 subjects, the results of the dual-wavelength excitation method and a reference high performance liquid chromatography (HPLC) assay were closely correlated both for ZnPP ($r_s = 0.943$, $p < 0.0001$; range 37–689 μmol ZnPP/mol heme, 84–1238 nmol/L) and for PPIX ($r_s = 0.959$, $p < 0.0001$; range 42–4212 μmol PPIX/mol heme, 93–5394 nmol/L). In addition, for ZnPP, the proposed method is compared with conventional single-wavelength excitation and with commercial front-face fluorimetry of washed erythrocytes and whole blood. We hypothesize that dual-wavelength excitation fluorimetry will provide a new approach to the suppression of background fluorescence in blood and tissue measurements of ZnPP and PPIX.

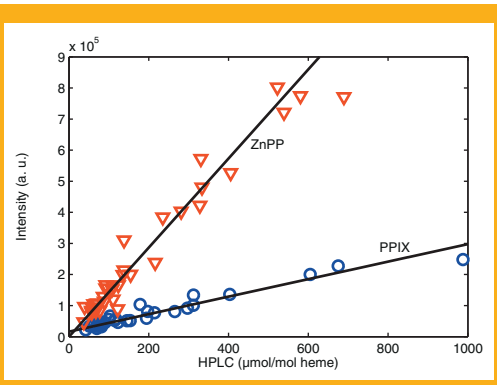

Correlation of the ZnPP/heme and PPIX/heme ratios as measured by the proposed dual-wavelength excitation method and the reference standard (HPLC), limited to the range 0–1000 μmol/mol heme.

* Corresponding author: e-mail: georg.hennig@med.lmu.de, Phone: +49 89 7095 4867, Fax: +49 89 7095 4864

Journal of BIOPHOTONICS

1. Introduction

Quantification of the non-heme protoporphyrins, erythrocyte zinc protoporphyrin IX (ZnPP) and protoporphyrin IX (PPIX), individually or jointly, is useful for the diagnostic evaluation of a variety of disorders that restrict or disrupt the biosynthesis of heme. In the terminal step in heme biosynthesis in the erythroblast, the enzyme ferrochelatase (EC 4.99.1.1) inserts ferrous iron into PPIX to produce heme [1]. Divalent iron is the preferred substrate for erythroid ferrochelatase, but divalent zinc can serve as an alternative, and small amounts of ZnPP are formed under physiological conditions [2]. In health, the non-heme protoporphyrins are present as approximately 85–95% ZnPP and 5–15% PPIX [2–4].

The concentrations of ZnPP and PPIX in erythroid cells are characteristically altered by conditions that affect the availability of ferrous iron, increase the amounts of PPIX, or diminish the enzymatic activity of ferrochelatase. Disturbances in the supply of iron for erythropoiesis are by far the most common causes of alterations in erythrocyte ZnPP. Iron deficiency, affecting more than two billion people worldwide [5, 6], decreases the delivery of iron to ferrochelatase for heme synthesis, resulting in increased formation of ZnPP [2]. In the absence of iron deficiency, disorders such as inflammation, infection and malignancy may limit the delivery of iron for erythropoiesis [7, 8], increasing erythrocyte ZnPP [9]. Even with no limitation of iron release from adequate stores, administration of erythropoiesis-stimulating agents can cause iron requirements for red cell production to exceed supply, also increasing ZnPP. A variety of genetic disorders, generally rare or uncommon, may also impair the delivery or utilization of iron for erythropoiesis [7], elevating erythrocyte ZnPP. Conversely, conditions such as hereditary hemochromatosis and some other forms of iron overload that augment the iron supply to the erythroid marrow may decrease the small amounts of ZnPP formed under physiological conditions [2, 10]. Overproduction of PPIX, resulting from a gain of function mutation in the rate-limiting erythroid-specific (ALAS2) isoform of mitochondrial 5-aminolevulinate synthase (EC 2.3.1.37), results in marked accumulation of both PPIX and ZnPP in the recently recognized X-linked dominant protoporphyria [11]. Decreased ferrochelatase enzymatic activity in erythropoietic protoporphyria also produces massive increases in erythrocyte PPIX, but without an increase in ZnPP [3, 12]. Erythrocyte PPIX may also be elevated in aminolevulinic acid dehydratase deficiency porphyria while ZnPP accumulates in congenital erythropoietic porphyria and hepatoerythropoietic porphyria [13, 14]. In the remaining forms of porphyria, erythrocyte non-heme protoporphyrins generally lie within the reference range [13]. Lead and other heavy metal intoxication [15–17] and a variety of sideroblastic [18] and inherited microcytic anemias [19] may also be responsible for alterations in erythrocyte PPIX and ZnPP. A recent study found decreased PPIX fluorescence in erythrocytes from diabetic compared to non-diabetic mice, suggesting the possible use of PPIX as a diagnostic marker for monitoring of diabetes [20]. In addition to their diagnostic utility, measurements of PPIX and ZnPP may be useful in following the effects of therapy on iron deficiency, the course of chronic disorders [9], and some forms of porphyria. For clinical diagnosis and screening, the ratios of erythroid ZnPP/heme and PPIX/heme are preferred over their absolute concentrations [2] because these proportions are independent of the circulating hemoglobin concentration.

Despite the diagnostic utility of determinations of the concentrations of ZnPP and PPIX in a variety of settings, the clinical use of these measurements has been restricted, in part by technical considerations. The reference method for their quantification, extraction and separation by high performance liquid chromatography (HPLC) [4, 10, 21, 22] requires specialized laboratory expertise and facilities. To calculate the ZnPP/heme and PPIX/heme ratios, an additional measurement of the circulating hemoglobin concentration is required. A variety of other methods for determination of both ZnPP and PPIX have been developed [3, 23–29] but, for the most part, have proven too technically demanding or cumbersome for general adoption. For measurement of ZnPP alone, a portable front-face fluorometer, the hematofluorometer [30], designed for easy use, was introduced over three decades ago and remains commercially available (AVIV Hematofluorometer, Model 206D, Aviv Biomedical, Inc., Lakewood, NJ, USA). The hematofluorometer requires only a drop of capillary or venous blood to directly measure the fluorescence light emitted by erythrocyte ZnPP. In approximation, the signal is independent of the patient hemoglobin concentration [30] and is a direct measure for the ZnPP/heme ratio [30, 31].

For screening for iron deficiency in regions endemic for malaria and other infections, the World Health Organization recommends the erythrocyte ZnPP as the preferred indicator for identifying iron-deficient children who could benefit from iron supplementation [32, 33]. An important limitation of the hematofluorometer is that the signal detected is influenced by background fluorescence of other blood constituents, such as bilirubin [16, 34–37], causing a falsely elevated ZnPP/heme ratio [35, 37–39]. Washing the erythrocytes [2, 36, 37, 39, 40] can largely eliminate such background interference, but requires anticoagulated blood obtained by venipuncture rather than a drop of capillary blood from finger puncture, an extended sample preparation time, additional laboratory facilities and trained personnel. These con-

straints have limited the use of the existing front-face hematofluorometer, especially in resource-limited settings like those in most regions with endemic malaria.

We describe an approach that can measure simultaneously both ZnPP and PPIX while effectively eliminating background fluorescence from unwashed erythrocytes. This method could be simply and cost-effectively implemented in a device for use under field conditions [33]. The fluorescence of the sample (including ZnPP, PPIX and background fluorophores) is quantified by using two excitation wavelength bands in an automated fashion, with the wavelengths chosen so that the light undergoes virtually identical absorption. In addition, the spectral separation of the two wavelengths can be small (less than 20 nm), so that the light scattering coefficients are nearly identical. As a consequence, the penetration depths of the photons at both excitation wavelengths are essentially the same, thereby exciting fluorescence from the same analyte and autofluorescence fluorophores. If the excitation efficiency of the fluorophores responsible for autofluorescence differs by only a small amount between the two excitation wavelengths, subtraction of the emission spectra excited at the two wavelengths effectively eliminates or cancels the autofluorescence. In contrast, if the analyte fluorophore exhibits a large difference in excitation efficiency between these two excitation wavelengths, the difference between the emission spectra does not eliminate the analyte fluorophore signal and will be virtually specific for the analyte fluorophore. This is the case for 425 nm (the ZnPP fluorescence excitation maximum, emission maximum at 593 nm [2, 27]) and 407 nm as a corresponding wavelength with identical oxygenized heme absorption [41], but substantially lower ZnPP excitation efficiency. Moreover, as the excitation wavelength at 407 nm approaches the PPIX excitation maximum at 397 nm [2], the emission spectrum shows a pronounced PPIX fluorescence emission peak, which is found at 627 nm [23, 27, 38, 42]. As the PPIX excitation efficiency is much lower at 425 nm, the PPIX fluorescence emission peak is not eliminated in the difference spectrum and can be evaluated along with the ZnPP signal.

The strategy of using two excitation wavelengths is potentially especially advantageous to eliminate background fluorescence, if it is intended to quantify the ZnPP fluorescence by non-invasive tissue measurements in a future application. Among the main tissue fluorophores are collagen and elastin crosslinks [43], whose fluorescence intensities are expected to exceed the ZnPP fluorescence signal remitted from tissue surfaces by two orders of magnitude. Therefore, methods for efficient suppression of background fluorescence are required for successful non-invasive ZnPP/heme ratio quantification. The standard solution for this problem would be spectral unmixing [44], using single-wavelength excitation. This approach requires detailed and accurate knowledge of the spectral shapes of the components to disentangle. Suitable characterization for tissue autofluorescence is not available because the composition and layering of contributing fluorophores and absorbers shows considerable local variations. In addition, spectral unmixing requires highly spectrally resolved detection of fluorescence emission spectra, limiting the applicability to a device for use under field conditions [33], where a cost-effective solution is required.

The goal of the present study is the quantification of the ZnPP/heme and PPIX/heme ratios from unwashed blood samples using the proposed dual-wavelength excitation approach, with comparison to the results of the reference HPLC method in a series of blood samples from control subjects and subjects with iron deficiency. From these measurements, the ZnPP/PPIX ratio is calculated for each blood sample. For the ZnPP/heme ratio alone, we further compare the dual-wavelength excitation results with (i) those of conventional single-wavelength excitation, where the emission spectrum is analyzed, and (ii) those of a commercial hematofluorometer using washed erythrocytes and whole blood. The single-wavelength excitation method is similar to the technique proposed by Gorodetsky et al. [38], who evaluated the integral of the 593 nm ZnPP peak, limited to a linear fitted fluorescence background baseline between 573 nm and 620 nm, using a spectrometer. In contrast, to facilitate implementation in an improved ZnPP/heme and PPIX/heme detection device for use under field conditions [33], the proposed methods are designed to be as simple as possible without a requirement for a spectrometer. In the proposed approach, the spectrometer can be replaced by detecting the fluorescence light with sensitive high dynamic range photodetectors through appropriate band-pass filters.

2. Material and methods

2.1 Blood samples

For comparisons of methods of protoporphyrin measurement, we used 35 residual whole blood samples remaining after completion of all clinical laboratory examinations in control subjects and patients with uncomplicated iron deficiency. All blood samples in this study were anonymized in accordance with the approved procedures of the Institutional Review Board of the Klinikum der Universität München and with the Declaration of Helsinki. Samples were obtained in EDTA-containing tubes by clinically indicated venipuncture and analyzed in the Institute of Laboratory Medicine of the Klinikum der Universi-

tät München. Analyses using front-fluorimetry were performed within 12 hours after sampling. Sample aliquots for HPLC-analyses were kept at −80 °C until analysis within 4 weeks.

2.2 Prototype spectroscopic measurement setup

2.2.1 Experimental setup

Fluorescence spectroscopic measurements were performed on diluted blood samples, with a concentration of 2% whole blood in phosphate buffered saline, PBS 1× (Dulbecco's Phosphate Buffered Saline without Ca^{2+}, Mg^{2+}, Biochrom AG, Berlin, Germany). The total sample volume was 3000 µl including 60 µl whole EDTA blood in disposable cuvettes (acrylic, size: 10 mm × 10 mm × 48 mm, ref. 67.755, Sarstedt, Nümbrecht, Germany).

For fluorescence excitation, white light from a 500 W short-arc Xe-lamp (T-Light, Karl Storz, Tuttlingen, Germany) was optically filtered in such a way that the central wavelength of the transmitted light was tunable in the blue wavelength range, 395–431 nm, while preserving the spectral bandwidth (5 nm full width/half maximum, FWHM). Light in the wavelength range 500–750 nm was suppressed with OD > 10. The filtered blue light was then reflected by a dichroic beam splitter, as shown schematically in Figure 1. The blue light beam was focused onto the cuvette sample, with a focus diameter of 2 mm. The total excitation light power was 6 mW (central wavelength 425 nm, wavelength-dependent) on the sample. The fluorescence light emitted from the sample was transmitted backwards through the beam splitter and filtered by a long-pass filter (OG515, Schott AG, Mainz, Germany), limiting the usable detection range to 520–750 nm. Finally, the fluorescence light was coupled into a cross-section converting fiber, consisting of seven 200 µm-diameter optical fibers, arranged in a circle. These fibers, linearly arranged at the other end of the fiber bundle, were coupled into a temperature regulated CCD spectrometer (detection range: 340–1022 nm, S2000-TR, Ocean Optics, Inc., Dunedin, FL, USA), yielding an effective spectral resolution of 5 nm.

Because the emission intensity of the short-arc lamp is wavelength-dependent, the intensity of the filtered light is also wavelength-dependent. In addition, the total power of the lamp may change during usage. To allow correction for wavelength- and time-dependent intensity variations, fluorescence standard measurements were performed. The fluorescence standard consisted of a 1 mm thick piece of commercially available solid polymethylmethacrylate containing Rhodamin B (1BF/RB, Starna GmbH, Pfungstadt, Germany), fixed at the wall of a cuvette.

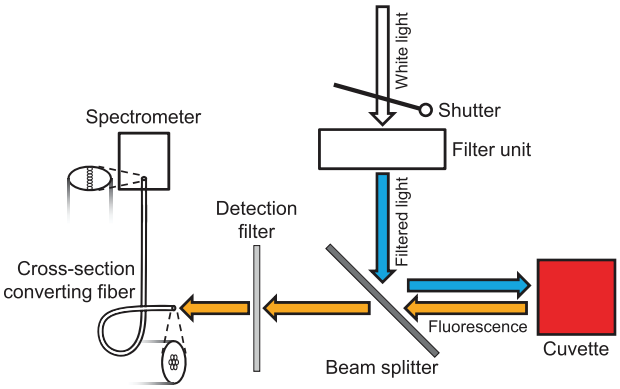

Figure 1 Schematic of the measurement setup. White light from a 500 W short-arc Xe-lamp is filtered in such a way, that the filtered light is tunable within the range 395–431 nm with a bandwidth of 5 nm (FWHM). This blue light is reflected by a beam splitter and focused on a cuvette containing the sample. The excited fluorescence light is transmitted backwards through the beam splitter, filtered by the detection filter, transmitted through a cross-section converting fiber and finally detected by a temperature-regulated CCD spectrometer.

2.2.2 Data acquisition

For all measurements, the light source was tuned to 425 nm and 407 nm (central wavelengths) with a spectral bandwidth of 5 nm FWHM. After acquiring the fluorescence emission spectra for the excitation wavelengths, a shutter was closed to prevent further illumination of the sample, and a dark spectrum was recorded with the same settings.

For the measurement of the Rhodamin B fluorescence standard, the CCD spectrometer integration time was set to 40 ms, averaging internally over 16 spectra. Including the time required for the wavelength-tuning of the filter unit and the shutter, the measurement time was 4 s. For the measurements of blood samples, which showed much dimmer fluorescence, the integration time was set to 400 ms, averaging internally over 4 spectra, resulting in a total measurement time of 10 s. The stability of the signal during measurements was verified.

2.2.3 Spectral calibration and normalization process

From all raw, uncorrected spectra $F_{\text{uncorrected}}(\lambda)$, the corresponding dark spectrum $D(\lambda)$ was subtracted. The resulting spectrum was multiplied by the factor

$C_{\text{excitation}}$ that depends on the excitation wavelength and is used to compensate for wavelength- and time-dependent variations in excitation light intensity, as well as for variations in optical adjustment. In addition, the resulting spectra were divided by the wavelength-dependent transmission of the detection filter $T_{\text{filter}}(\lambda)$, and multiplied by a wavelength-dependent factor including optical fiber transmission and spectrometer sensitivity $C_{\text{spectrometer}}(\lambda)$. These additional calibration factors allow comparing the corrected spectra $F_{\text{corrected}}(\lambda)$ to spectra that were measured using other devices, because influences of the spectral sensitivity of the detection optics and the spectrometer are compensated. The complete calibration procedure is shown in Eq. (1).

$$F_{\text{corrected}}(\lambda) = [F_{\text{uncorrected}}(\lambda) - D(\lambda)] \times \frac{C_{\text{spectrometer}}(\lambda)}{T_{\text{filter}}(\lambda)}\, C_{\text{excitation}} \quad (1)$$

To obtain $C_{\text{excitation}}$, the calibration procedures described above (dark subtraction, filter transmission, detection sensitivity calibration, except for the factor $C_{\text{excitation}}$) were first applied to the fluorescence standard measurement, $F_{\text{Rhodamin B}}(\lambda)$. Then, $C_{\text{excitation}}$ was calculated as described in Eq. (2): The reference value of the Rhodamin B fluorescence maximum from a reference measurement, $\max\{R_{\text{Rhodamin B}}(\lambda)\}$ was divided by the maximum of the Rhodamin B fluorescence measured by the prototype measurement setup, $\max\{F_{\text{Rhodamin B}}(\lambda)\}$. The reference measurement was recorded by a fluorescence spectrometer (Fluoromax-2, Jobin Yvon GmbH, Unterhaching, Germany), with excitation and detection monochromator adjusted to match excitation and detection bandwidth (5 nm FWHM) of the measurement setup.

$$C_{\text{excitation}} = \frac{\max\{R_{\text{Rhodamin B}}(\lambda)\}}{\max\{F_{\text{Rhodamin B}}(\lambda)\}} \quad (2)$$

2.3 Dual-wavelength excitation method

The proposed method for reducing the influence of background fluorescence on the detected intensity at 593 nm using two excitation wavelength bands was implemented for measurements using the prototype spectroscopic measurement setup and is referred to as the "dual-wavelength excitation method". For quantification of the ZnPP/heme ratio, one emission wavelength band, centered at 593 nm, was used. In a similar fashion, the PPIX/heme ratio was quantified by a second emission wavelength band centered at 627 nm. The method is illustrated in Figure 2, where two corrected emission spectra (F_{425} and F_{407}) of a patient blood sample (HPLC determined ZnPP/heme ratio = 333 µmol ZnPP/mol heme, 486 nmol ZnPP/L, and PPIX/heme ratio = 605 µmol PPIX/mol heme, 882 nmol PPIX/L) are shown. The central excitation wavelengths were 425 nm and 407 nm, respectively. For optimized overlap in the 520 nm–570 nm region, F_{407} was scaled by a factor 1.15. Additionally, the difference between these spectra is shown, and is referred to subsequently as a "difference spectrum". In Figure 2, the differences of the two spectra at 593 nm and at 627 nm are highlighted by arrows: as the excitation wavelength 407 nm approaches the PPIX excitation maximum at 397 nm [2] and is far off the ZnPP excitation maximum at 424 nm [2, 45], the emission spectrum F_{407} shows a pronounced PPIX fluorescence emission peak, which is found at 627 nm in accordance with the literature [23, 27, 38, 42], compared to the lower ZnPP fluorescence peak at 593 nm [2, 23, 27]. The difference in the range 520 nm–570 nm becomes nearly zero, which shows that the background fluorescence is virtually eliminated by calculating the difference spectrum.

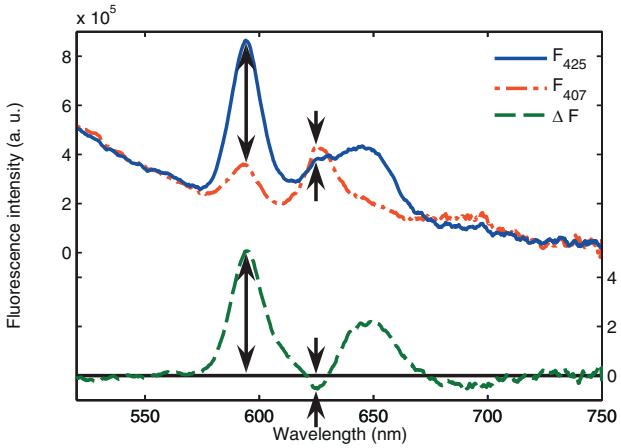

Figure 2 Two examples of corrected emission spectra, excited at 425 nm, F_{425}, and 407 nm, F_{407}, are shown (left axis description). In a shifted axis (right axis description), the difference of both spectra ("difference spectrum") ΔF is shown. In the difference spectrum, the background fluorescence is nearly reduced to zero, visible in the range 520 nm–570 nm. The double arrows indicate the differences of the fluorescence intensities at 593 nm (the emission maximum of ZnPP) and at 627 nm (the emission maximum of PPIX) in both the corrected emission spectra and the difference spectrum.

The difference spectrum was then used to evaluate both ZnPP and PPIX fluorescence. The ZnPP/heme ratio can be directly quantified by evaluating the fluorescence intensity at 593 nm (averaging over 590 nm–596 nm), as illustrated in Figure 3. In addition, a ZnPP emission spectrum is shown. It is evident that at 627 nm, a linear combination of ZnPP and PPIX fluorescence intensities yields the signal at 627 nm: the ZnPP fluorescence (positive value in the difference spectrum) and the PPIX fluorescence (negative value in the difference spectrum). Therefore,

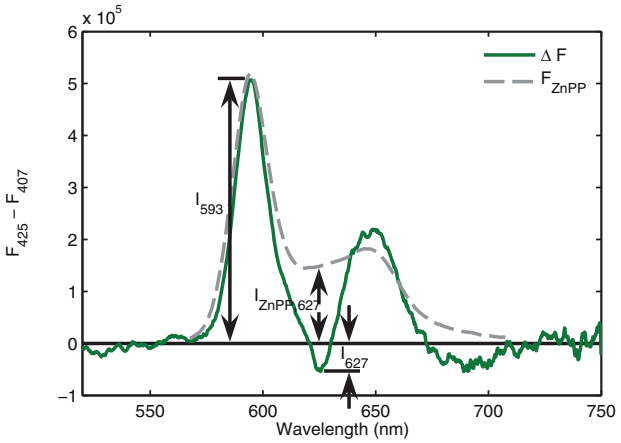

Figure 3 The example difference spectrum ΔF as shown in Figure 2 is used to illustrate the dual-wavelength excitation method. The ZnPP fluorescence emission spectrum F_{ZnPP} is also displayed. Evaluation of the peak intensity at 593 nm (double arrows, solid line, I_{593}) is used to quantify the ZnPP/heme ratio. This also serves to quantify the ZnPP fluorescence intensity at 627 nm, $I_{ZnPP,627}$ (double arrows, dashed line). The total difference between the measured intensity at 627 nm (arrows, I_{627}, may be negative) and the intensity of the ZnPP fluorescence at 627 nm, $I_{ZnPP,627}$, is then used to calculate the PPIX fluorescence at 627 nm.

a measure for the PPIX/heme ratio I_{PPIX} can be calculated according to Eq. (3): the PPIX fluorescence is the negative of the detected fluorescence at 627 nm I_{627} plus the ZnPP fluorescence intensity at 627 nm, $I_{ZnPP,627}$, which equals 1/3 of the ZnPP fluorescence intensity at 593 nm.

$$I_{PPIX} = -I_{627} + 1/3\, I_{593} \tag{3}$$

Finally, the ZnPP/PPIX ratio was calculated by dividing the ZnPP/heme and the PPIX/heme ratios, I_{ZnPP}/I_{PPIX}. As both ratios are given in arbitrary units, this calculated ZnPP/PPIX ratio is also given in arbitrary units.

2.4 Precision

Six patient blood samples were diluted 10 times each and the resulting 60 samples were measured in the prototype spectroscopic measurement setup. The precision was quantified by the standard deviation of the evaluated fluorescence intensities I_{ZnPP} and I_{PPIX}.

2.5 Commercial front-face fluorometer

An AVIV Hematofluorometer (Model 206D, Aviv Biomedical, Inc., Lakewood, NJ, USA) was used to quantify the ZnPP/heme ratio according to the manufacturer's instructions, using materials for calibration and quality assurance obtained from the manufacturer. In this commercial analyzer system, a drop of sample material is placed on a glass slide; the slide is transferred into the instrument and after few seconds the ZnPP/heme ratio is shown in units [µmol ZnPP/mol heme] on the built-in display. According to the study protocol, analyses were performed using whole blood and erythrocytes washed using normal saline solution.

2.6 HPLC

Erythrocyte ZnPP and PPIX were quantified using a commercially available and CE-labeled HPLC-kit method according to the manufacturer's instructions [46]. The method involves isocratic reversed phase chromatography and fluorescence detection (excitation 417 nm, emission 635 nm). Sample preparation includes a one-step protein precipitation with addition of an internal standard compound. Run-time is approximately 11 minutes. Lyophilized materials for calibration and quality control are part of the kit. HPLC measurements were performed in duplicate.

In a first measurement, the ZnPP and PPIX concentrations C_{ZnPP} and C_{PPIX} were determined as absolute concentrations in units of nmol/L. In a second measurement, the hemoglobin concentration C_{Heme} was determined by a Sysmex XE-5000 haematology analyzer (Sysmex Corporation, Kobe, Japan) in units of g/dL. From both measurements, C_{ZnPP} and C_{Heme}, the ZnPP/heme ratio (and in the same way, from C_{PPIX} and C_{Heme} the PPIX/heme ratio) was calculated by Eq. (4), using the hemoglobin subunit's molecular weight 64,458g/mol [47].

$$\frac{C_{ZnPP}}{C_{Heme}}\left[\frac{\mu mol}{mol}\right] = \frac{C_{ZnPP}[nmol]}{C_{Heme}[g/dL]}\frac{64,458}{10^4} = \frac{C_{ZnPP}[nmol/L]}{0.1551 \cdot C_{Heme}[g/dL]} \tag{4}$$

According to the manufacturer, the HPLC measurements using the Zinc-Protoporphyrin/Protoporpyrin HPLC Kit have an inter-assay reproducibility standard deviation of 9% (ZnPP) and 10% (PPIX), respectively [46].

2.7 Statistical evaluation

MATLAB (R2010a, MathWorks®, Natick, MA, USA) was used for statistical data evaluation. For the statistical evaluation of the correlation of two methods, a Passing-Bablok regression was calculated, including 95% confidence intervals and the Spear-

man's Rho r_s with corresponding p-value (*i.e.* test against the hypothesis of no correlation, correlation if $p < 0.05$) was calculated (MATLAB function corr). Tests for normality were performed using SigmaPlot (SigmaPlot 11, Systat Software, Inc., San Jose, CA, USA).

3. Results

Non-parametric methods were used for data evaluation because none of the presented data sets fulfilled the criteria for a normal distribution ($p < 0.001$).

3.1 Dual-wavelength excitation method

3.1.1 Measurement of the ZnPP/heme ratio

The precision of the evaluated ZnPP peak intensity of the difference spectrum was 10%, determined by measurements repeated 10 times for each of 6 patient blood samples. The correlation of the ZnPP fluorescence intensity evaluated by the dual-wavelength excitation method and the reference HPLC method is shown in Figure 4, including the Passing-Bablok regression. The error bars indicate the precision of each method. The Spearman's Rho is $r_s = 0.943$, $p < 0.0001$. The relative residuals of the measurement and the Passing-Bablok regression are shown in the lower panel, being in the range −0.49 to +0.72 with a standard deviation of 0.22.

The ZnPP/heme ratio was also quantified by evaluating solely the fluorescence spectra excited with 425 nm: The background fluorescence measured in a wavelength band centered at 573 nm was subtracted from the fluorescence intensity at the ZnPP emission maximum at 593 nm. This background-corrected ZnPP fluorescence intensity shows a similar Spearman's Rho $r_s = 0.948$, the same precision and very similar range and standard deviation of relative residuals (range: −0.46 to +0.79, standard deviation: 0.22), when correlated with the HPLC values.

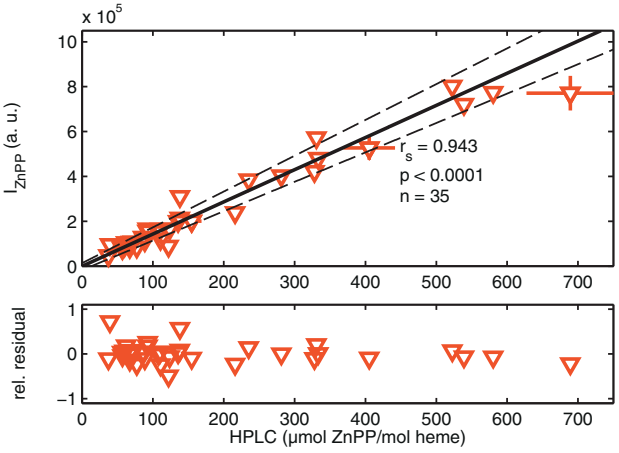

Figure 4 In the upper panel, the correlation between the measured fluorescence intensity of the difference spectrum at 593 nm evaluated by the dual-wavelength excitation method (y-axis) and the ZnPP/heme ratio (µmol ZnPP/mol heme) measured by HPLC measurements (x-axis) is shown, including error bars for three data points. In addition, the Passing-Bablok regression is shown (solid line) with 95% confidence intervals (dashed lines). The number of samples was $n = 35$, the Spearman's Rho $r_s = 0.943$ and the p-value $p < 0.0001$. In the lower panel, the relative residuals between the measurements and the Passing-Bablok regression are shown (range: −0.49 to +0.72, standard deviation: 0.22).

3.1.2 Measurement of the PPIX/heme ratio

The precision of the PPIX fluorescence intensity, calculated from the intensity of the difference spectrum at 627 nm and 593 nm using Eq. (3), was 15%, determined by measurements repeated 10 times for each of 6 patient blood samples. The Passing-Bablok regression of the PPIX fluorescence intensity evaluated by the dual-wavelength excitation method and the HPLC measurement is shown in Figure 5. The

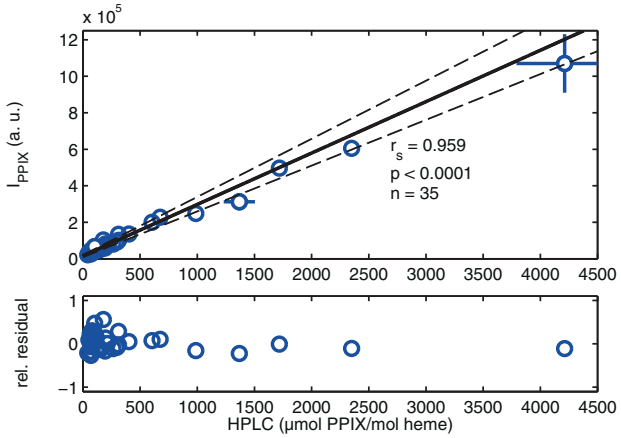

Figure 5 In the upper panel, the correlation between the measured fluorescence intensity of the difference spectrum at 627 nm evaluated by the dual-wavelength excitation method (y-axis) and the PPIX/heme ratio (µmol PPIX/mol heme) measured by HPLC measurements (x-axis) is shown, including error bars for three data points. In addition, the Passing-Bablok regression is shown (solid line) with 95% confidence intervals (dashed lines). The number of samples was $n = 35$, the Spearman's Rho $r_s = 0.959$ and the p-value $p < 0.0001$. In the lower panel, the relative residuals between the measurements and the Passing-Bablok regression are shown (range: −0.26 to +0.56, standard deviation: 0.19).

error bars indicate the precision of each method. The Spearman's Rho is $r_s = 0.959$, $p < 0.0001$. The relative residuals of the measurement and the Passing-Bablok regression are shown in the lower panel, being in the range −0.26 to +0.56 with a standard deviation of 0.19.

3.1.3 Calculation of the ZnPP/PPIX ratio

The ZnPP/PPIX ratio, calculated from the ZnPP and PPIX fluorescence intensities for each patient blood sample ($n = 35$), is shown in Figure 6. The average ZnPP/PPIX ratio was 2.74 (a.u.), with a range 0.64 to 7.91 (a.u.) and a standard deviation of 1.45 (a.u.). From the HPLC measurements, the average ZnPP/PPIX ratio was determined to be 0.90, which equals a proportion of 47% ZnPP of the total erythrocyte non-heme protoporphyrins.

3.2 Commercial front-face fluorometer

3.2.1 Measurement using washed erythrocytes

The Passing-Bablok regression between the ZnPP/heme ratio determined by the AVIV hematofluorometer on washed erythrocytes and the reference HPLC method is shown in Figure 7. The error bars indicate the precision of each method, being 9% (HPLC) [46] and 15% (hematofluorometer) [40]. The Spearman's Rho is $r_s = 0.956$, $p < 0.0001$. The relative residuals of the measurement and the Passing-Bablok regression are shown in the lower panel, being in the range −0.36 to +0.50 with a standard deviation of 0.19.

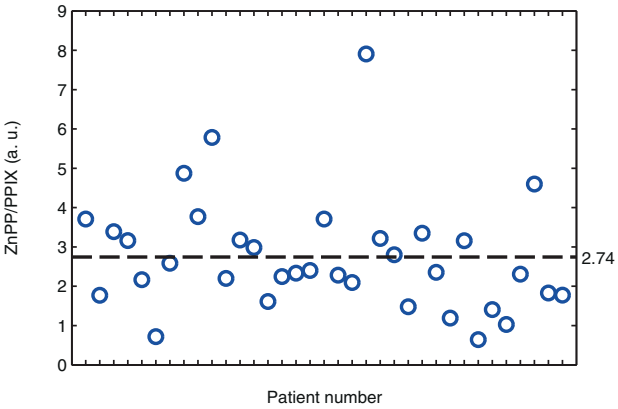

Figure 6 The ZnPP/PPIX ratio calculated from the ZnPP and PPIX fluorescence intensities as evaluated by the dual-wavelength excitation method for each patient ($n = 35$) is shown. The average ZnPP/PPIX ratio = 2.74 (a.u.) is also indicated (range: 0.64 to 7.91, standard deviation: 1.45).

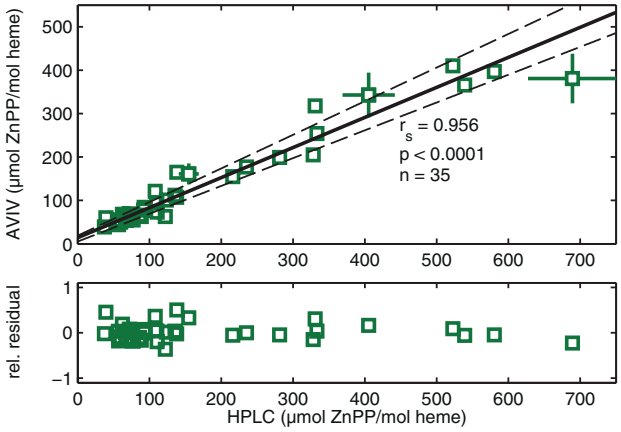

Figure 7 In the upper panel, the correlation between the ZnPP/heme ratio (µmol ZnPP/mol heme) measured by an AVIV Hematofluorometer using washed erythrocytes (y-axis) and measured by HPLC measurements (x-axis) is shown, including error bars for three data points. In addition, the Passing-Bablok regression is shown (solid line) with 95% confidence intervals (dashed lines). The number of samples $n = 35$, Spearman's Rho $r_s = 0.956$ and the p-value $p < 0.0001$. In the lower panel, the relative residuals between the measurements and the Passing-Bablok regression are shown (range: −0.36 to +0.50, standard deviation: 0.19).

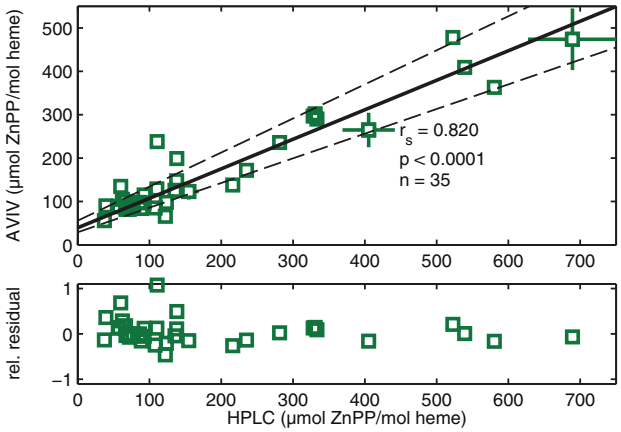

Figure 8 In the upper panel, the correlation between the ZnPP/heme ratio (µmol ZnPP/mol heme) measured by an AVIV Hematofluorometer using whole blood (y-axis) and measured by HPLC measurements (x-axis) is shown, including error bars for three data points. In addition, the Passing-Bablok regression is shown (solid line) with 95% confidence intervals (dashed lines). The number of samples $n = 35$, Spearman's Rho $r_s = 0.820$ and the p-value $p < 0.0001$. In the lower panel, the relative residuals between the measurements and the Passing-Bablok regression are shown (range: −0.46 to +1.08, standard deviation: 0.28).

3.2.2 Measurement using unprocessed whole blood

The Passing-Bablok regression between the ZnPP/heme ratio determined by the AVIV hematofluorometer on unprocessed whole blood and the reference HPLC method is shown in Figure 8. The Spearman's Rho is $r_s = 0.820$, $p < 0.0001$. The relative residuals of the measurement on unprocessed whole blood and the Passing-Bablok regression show a considerably larger range and standard deviation (range: −0.46 to +1.08, standard deviation: 0.28). A significantly larger intercept (39 μmol ZnPP/mol heme, 95% confidence interval: 29–56 μmol ZnPP/mol heme) is observed compared to the hematofluorometer measurements using washed erythrocytes (14 μmol ZnPP/mol heme, 95% confidence interval: 5–19 μmol ZnPP/mol heme).

4. Discussion

These results show that measurements of ZnPP and PPIX from unwashed blood samples using the dual-wavelength excitation method (excitation wavelength bands centered at 425 nm and 407 nm; emission wavelength bands centered at 593 nm for ZnPP/heme and at 627 nm for PPIX/heme) and by a reference high performance liquid chromatography (HPLC) assay were so closely correlated both for ZnPP ($r_s = 0.943$, $p < 0.0001$; range 37–689 μmol ZnPP/mol heme, 84–1238 nmol/L) and for PPIX ($r_s = 0.959$, $p < 0.0001$; range 42–4212 μmol PPIX/mol heme, 93–5394 nmol/L) as to be virtually interchangeable. Some blood samples showed very high PPIX levels (>1000 μmol PPIX/mol heme, >2000 nmol PPIX/L), but no adverse influence on the precision of the ZnPP/heme ratio quantification was observed. The minimal sample preparation and the ease of simultaneous measurement of both ZnPP and PPIX by the dual-wavelength excitation method potentially offer a new clinical tool for investigation of conditions that restrict or disrupt heme biosynthesis.

Changes in the amounts of ZnPP and PPIX formed during erythropoiesis are reflected in the peripheral blood only slowly because, in health, the lifespan of the red blood cell in the circulation is roughly 120 days. As a result, at steady state, newly formed erythrocytes replace senescent red blood cells and alter mean protoporphyrin concentrations at a rate somewhat less than 1% per day. Inside the erythrocyte, ZnPP binds to intact oxyhemoglobin in a nonspecific, noncovalent interaction [31] and seems to be retained throughout the lifespan [48]. By contrast, PPIX is lipophilic and passes through the red cell membrane, leaking into the plasma at a rate that is approximately proportional to the concentration of PPIX within the erythrocyte [49]. Consequently, the amounts and relative proportions of ZnPP and PPIX can provide information about the rate, course and duration of alterations in heme synthesis that may be diagnostically useful, for example, in distinguishing iron deficiency from other causes of iron-restricted erythropoiesis, hereditary from acquired conditions, and in monitoring response to therapy.

While both the single-wavelength excitation approach and the commercial front-face fluorometer using washed erythrocytes yielded comparable results for ZnPP alone, neither provided the potentially useful information available from simultaneous measurements of PPIX. Within the 35 blood samples investigated in this study, the ZnPP/PPIX ratio varied with a factor of 12.4 between the lowest and highest value. In the literature, a linear correlation between the erythrocyte ZnPP concentration and the "free" erythrocyte protoporphyrin concentration (= total amount of erythrocyte protoporphyrin, FEP) was reported, however also with large deviations from the linear regression [16, 21]. This broad variation suggests that the ZnPP/PPIX ratio indeed might provide valuable information. The HPLC measurements indicate a contribution of 47% of ZnPP to the erythrocyte non-heme protoporphyrins, which deviates from the values (85–95%) found in the older literature [2–4]. However, this may be attributed to the fact that erythrocyte porphyrin measurement has been poorly standardized to date; in particular, no external quality assessment system has been implemented for erythrocyte porphyrin determination. The present study has focused on uncomplicated iron deficiency and extension of the dual-wavelength excitation method for measurement of ZnPP and PPIX in the porphyrias and other disorders will require additional investigation.

The close correlation for ZnPP and PPIX between the dual-wavelength excitation and HPLC reference methods indicate that subtraction of the emission spectra excited at the two excitation wavelength bands (centered at 425 nm and 407 nm, respectively) was successful in eliminating the background autofluorescence of other blood constituents for both non-heme protoporphyrins. This enables a reliable measurement of ZnPP in unwashed blood samples with the same precision as the current procedure using washed erythrocytes. The precision of hematofluorometer measurements performed on unprocessed whole blood is considerably worse and washing of blood samples is recommended. Additionally, the values measured by the hematofluorometer using unwashed blood samples are systematically higher than the ones measured using washed erythrocytes (25 μmol ZnPP/mol heme higher readings on average), which agrees within the limits of

precision with the difference of 18 μmol ZnPP/mol heme found by Hastka et al. [36]. As noted in the introduction, the requirement for washing of red blood cells restricts the use of ZnPP measurements, especially in developing countries. The dual-wavelength excitation approach described here could improve field devices [33] in settings where ZnPP/heme ratio quantification is needed.

We hypothesize that the dual-wavelength excitation method also may be useful in eliminating or reducing the intense autofluorescence in tissue. Adaptation of the dual-wavelength excitation may offer an approach for non-invasive measurements of ZnPP and PPIX within erythrocytes in the microcirculation of tissues such as the oral mucosa *in vivo*.

5. Conclusion

In conclusion, dual-wavelength excitation measurements of ZnPP and PPIX from unwashed blood samples were closely correlated with determinations by a reference high performance liquid chromatography (HPLC) assay. This result indicated that subtraction of the emission spectra excited at the two excitation wavelengths, 425 nm and 407 nm, was successful in eliminating the background autofluorescence of other blood constituents for both non-heme protoporphyrins. We hypothesize that the dual-wavelength excitation approach also may be useful in eliminating or reducing autofluorescence in tissue such as the oral mucosa *in vivo*, enabling non-invasive measurements of ZnPP and PPIX.

Acknowledgements This work was financially supported, in part, by Nestec Ltd. The authors thank Mr. Hennel and Mr. Egeler for performing the HPLC and hematofluorometer measurements.

Author biographies Please see Supporting Information online.

References

[1] I. Hamza and H. A. Dailey, BBA-Mol. Cell Res. **1823**, 1617–1632 (2012).
[2] R. F. Labbe, H. J. Vreman, and D. K. Stevenson, Clin. Chem. **45**, 2060–2072 (1999).
[3] A. P. Orfanos, R. Guthrie, D. C. Jinks, and D. W. Vollmer, Clin. Chim. Acta **181**, 213–217 (1989).
[4] Y. M. Roh, K. Kim, and H. Kim, Ind. Health **38**, 372–379 (2000).
[5] M. B. Zimmermann and R. F. Hurrell, Lancet **370**, 511–520 (2007).
[6] S. R. Lynch, J. Nutr. **141**, 763s–768s (2011).
[7] L. T. Goodnough, E. Nemeth, and T. Ganz, Blood **116**, 4754–4761 (2010).
[8] M. Vogeser, K. Jacob, and R. Zachoval, Clin. Biochem. **33**, 387–391 (2000).
[9] J. Hastka, J. J. Lasserre, A. Schwarzbeck, M. Strauch, and R. Hehlmann, Blood **81**, 1200–1204 (1993).
[10] G. Metzgeroth, B. Schultheis, A. Dorn-Beineke, R. Hehlmann, and J. Hastka, Ann. Hematol. **86**, 363–368 (2007).
[11] S. D. Whatley, S. Ducamp, L. Gouya, B. Grandchamp, C. Beaumont, M. N. Badminton, G. H. Elder, A. Holme, A. V. Anstey, M. Parker, A. V. Corrigall, P. N. Meissner, R. J. Hift, J. T. Marsden, Y. Ma, G. Mieli-Vergani, J. C. Deybach, and H. Puy, Am. J. Hum. Genet. **83**, 408–414 (2008).
[12] M. Lecha, H. Puy, and J. C. Deybach, Orphanet J. Rare Dis. **4**, 19 (2009).
[13] E. Zaider and D. R. Bickers, Clin. Dermatol. **16**, 277–293 (1998).
[14] H. Puy, L. Gouya, and J. C. Deybach, Lancet **375**, 924–937 (2010).
[15] A. A. Lamola and T. Yamane, Science **186**, 936–938 (1974).
[16] V. Karacic, D. Prpicmajic, and S. Telisman, Int. Arch. Occup. Environ. Health **47**, 165–177 (1980).
[17] A. Schauder, A. Avital, and Z. Malik, J. Environ. Pathol. Toxicol. Oncol. **29**, 137–158 (2010).
[18] M. D. Fleming, Hematology/the Education Program of the American Society of Hematology. American Society of Hematology. Education Program **2011**, 525–531 (2011).
[19] A. Iolascon, L. De Falco, and C. Beaumont, Haematologica **94**, 395–408 (2009).
[20] G. Fauaz, A. R. Miranda, C. Z. Gomes, L. C. Courrol, F. R. Silva, F. G. Rocha, N. Schor, and M. H. Bellini, Appl. Spectrosc. **64**, 391–395 (2010).
[21] B. Kaul, G. Slavin, and B. Davidow, Clin. Chem. **29**, 1467–1470 (1983).
[22] E. Rossi and P. Garcia-Webb, Biomed. Chromatogr. **1**, 163–168 (1986).
[23] D. Hart and S. Piomelli, Clin. Chem. **27**, 220–222 (1981).
[24] G. G. Bailey and L. L. Needham, Clin. Chem. **32**, 2137–2142 (1986).
[25] H. Sato, K. Ido, and K. Kimura, Clin. Chem. **40**, 1239–1244 (1994).
[26] G. Kufner, H. Schlegel, and R. Jager, Clin. Chem. Lab. Med. **43**, 183–191 (2005).
[27] Q. Chen and R. E. Hirsch, Free Radic. Res. **40**, 285–294 (2006).
[28] P. C. Zhou, W. Huang, R. B. Zhang, Z. X. Zou, H. D. Luo, A. A. Falih, and Y. Q. Li, Appl. Spectrosc. **62**, 1268–1273 (2008).
[29] Q. Liu, W. Huang, A. A. F. Shindi, and Y. Q. Li, Talanta **88**, 663–668 (2012).
[30] W. E. Blumberg, J. Eisinger, A. A. Lamola, and D. M. Zuckerman, Clin. Chem. **23**, 270–274 (1977).
[31] R. E. Hirsch, M. J. Lin, and C. M. Park, Biochemistry **28**, 1851–1855 (1989).
[32] Food Nutr. Bull. **28**, S621–S627 (2007).

[33] R. J. Stoltzfus, R. Heidkamp, D. Kenkel, and J. P. Habicht, Food Nutr. Bull. **28**, S572–S584 (2007).
[34] E. Buhrmann, W. C. Mentzer, and B. H. Lubin, J. Lab. Clin. Med. **91**, 710–716 (1978).
[35] P. Grandjean and J. Lintrup, Scand. J. Work. Environ. Health **7**, 311–312 (1981).
[36] J. Hastka, J. J. Lasserre, A. Schwarzbeck, M. Strauch, and R. Hehlmann, Clin. Chem. **38**, 2184–2189 (1992).
[37] R. F. Labbe, A. Dewanji, and K. McLaughlin, Clin. Chem. **45**, 146–148 (1999).
[38] R. Gorodetsky, Z. Fuks, T. Peretz, and H. Ginsburg, Clin. Biochem. **18**, 362–368 (1985).
[39] R. B. Schifman and P. R. Finley, Clin. Chem. **27**, 153–156 (1981).
[40] P. J. Parsons, N. V. Stanton, E. W. Gunter, D. Huff, J. R. Meola, and A. A. Reilly, Clin. Chem. **35**, 2059–2065 (1989).
[41] S. A. Prahl, http://omlc.ogi.edu/spectra/hemoglobin/index.html (1999), retrieved 27.04.2010.
[42] S. Sandberg and A. Brun, J. Clin. Invest. **70**, 693–698 (1982).
[43] I. Pavlova, C. R. Weber, R. A. Schwarz, M. Williams, A. El-Naggar, A. Gillenwater, and R. Richards-Kortum, J. Biomed. Opt. **13**, 064012 (2008).
[44] C. Ran and A. Moore, Mol. Imaging Biol. **14**, 293–300 (2012).
[45] J. J. Leonard, T. Yonetani, and J. B. Callis, Biochemistry **13**, 1460–1464 (1974).
[46] Immundiagnostik AG, http://www.immundiagnostik.-com/fileadmin/pdf/Zink-Protoporphyrin_KC2700.pdf (2011), retrieved 20.08.2012.
[47] M. C. Van Beekvelt, W. N. Colier, R. A. Wevers, and B. G. Van Engelen, J. Appl. Physiol. **90**, 511–519 (2001).
[48] S. Sandberg, I. Talstad, G. Hovding, and N. Bjelland, Blood **62**, 846–851 (1983).
[49] M. Sassaroli, R. daCosta, H. Vaananen, and J. Eisinger, Cytometry **13**, 339–345 (1992).

PHOTOBLEACHING-BASED METHOD TO INDIVIDUALIZE IRRADIATION TIME DURING INTERSTITIAL 5-AMINOLEVULINIC ACID PHOTODYNAMIC THERAPY

GEORG HENNIG, HERBERT STEPP UND ANN JOHANSSON

Photodiagnosis and Photodynamic Therapy **8 (3)**, 275–281 (2011)

Photodiagnosis and Photodynamic Therapy (2011) **8**, 275—281

available at www.sciencedirect.com

ScienceDirect

journal homepage: www.elsevier.com/locate/pdpdt

Photobleaching-based method to individualize irradiation time during interstitial 5-aminolevulinic acid photodynamic therapy

Georg Hennig Dipl Phys*, Herbert Stepp, Ann Johansson

Laser-Forschungslabor, LIFE Center, University Hospital of Munich, Marchioninistraße 23, 81377 Munich, Germany
Available online 2 April 2011

PACS
42.62.Be (biological and medical applications);
87.50.wp (therapeutic applications);
87.50.wj (dosimetry/exposure assessment);
87.10.Kn (finite element calculations);
87.64.Cc (scattering of visible, uv, and infrared radiation);
87.64.kv (fluorescence)

KEYWORDS
Interstitial photodynamic therapy;
Brain PDT;
Fluorescence;
Finite element method;
Dosimetry

Summary Interstitial photodynamic therapy (iPDT) is being investigated for the treatment of high-grade human brain malignancies. In recent clinical studies, fluorescence monitoring during iPDT of glioblastoma multiforme has revealed patient-specific accumulation of photosensitizer (aminolevulinic acid (ALA) induced protoporphyrin IX, PpIX) and its photobleaching kinetics. As photosensitizer degradation, also referred to as photobleaching, and tissue damage are caused by the same underlying processes, the photobleaching kinetics might provide a tool for real-time treatment supervision. Here, we show with computer simulations that varying optical properties have a strong influence on the irradiation time required to fully bleach the photosensitizer. We propose a method to potentially determine the time point during iPDT, when the photosensitizer within the target volume has been largely photobleached. Simulations show that it is possible to determine this time point by continuously monitoring the ratio of the fluorescence intensities at two time points during irradiation. We show that this method works for a large range of optical properties, different photobleaching rates and varying inter-fibre distances. In conclusion, the relative fluorescence method offers the potential to individualize irradiation times to consume the photosensitizer within the target tissue during iPDT.

* Corresponding author. Tel.: +49 8970954867; fax: +49 8970954864.
E-mail address: georg.hennig@med.uni-muenchen.de (G. Hennig).

1572-1000/$ — see front matter © 2011 Elsevier B.V. All rights reserved.
doi:10.1016/j.pdpdt.2011.03.338

Introduction

Photodynamic therapy (PDT) is being investigated as an alternative treatment option for local treatment of various human malignancies such as prostate, bladder, head and neck, liver and brain tumours. PDT relies on the light-induced activation of a photosensitizer and the subsequent formation of different radicals and oxygen species, which in turn cause cellular damage. Presently, we are investigating interstitial PDT (iPDT) for the treatment of human high-grade brain malignancies [1—3]. The clinical protocol relies on the oral administration of 5-aminolevulinic acid (ALA, Gliolan®, medac GmbH, Wedel, Germany), which induces a highly tumour-selective uptake of the actual photosensitizer, protoporphyrin IX (PpIX). Subsequently, therapeutic light delivery of a pre-defined light dose is performed via 4—6 optical cylindrical diffusors, that have been stereotactically positioned within the tumour mass. ALA-mediated iPDT of recurrent glioblastoma multiforme (GBM) resulted in a median survival of 15 months [2] and some intriguing long-term survivors [4]. Reasons for the large differences in treatment response might be inter-patient variability in light distribution, photosensitizer accumulation [3], synergism between PDT and host immune response [5] and PDT-induced changes in tissue oxygenation and blood flow [6]. Clinical (brain)-PDT is currently performed with standardized light and photosensitizer doses, meaning that the patient-specificity as well as the spatial- and time-dependency of these parameters are neglected. The true potential of treatment supervision and feedback to individualize therapy is still relatively unexploited for brain-PDT.

With the aim to implement real-time, patient-individualized monitoring for PDT, different dosimetry models have been proposed. For example, in the explicit dosimetry model some or all of the parameters relevant for the PDT reaction, i.e. light, photosensitizer and oxygen, are incorporated, see for example [7—10]. Comprehensive theoretical models relying on the rate equations describing the processes from light absorption to PDT-induced singlet oxygen production and tissue damage have been investigated [11—13]. In the direct dosimetry model, the production of singlet oxygen is monitored via its weak, infrared luminescence, showing good correlation between total singlet oxygen amount and treatment efficacy [14]. The clinical usefulness of these technically complex approaches for PDT of large-volume target tissue is still limited. On the other hand, the implicit dosimetry model has been proposed to constitute a simpler and more robust approach where one single parameter implicitly contains information on the total PDT dose, independent of parameters such as varying photosensitizer levels, tissue optical properties and irradiation conditions [8]. A commonly employed dose metric relies on the photosensitizer photobleaching kinetics where it is assumed that PDT-induced singlet oxygen causes tissue damage as well as photodegradation of the photosensitizer. Rapid photobleaching has thus been shown to correlate with improved treatment outcome [15—19].

Here, we propose a method to monitor spatial-dependent photobleaching based on the photobleaching kinetics to individualize iPDT in real-time. This approach, hereafter referred to as the relative fluorescence method, aims at evaluating the time point at which the photosensitizer midway between therapeutic light sources is largely photobleached. It is emphasized, that the method differs from common dosimetry models in that it does not intend to predict the phototoxic dose, but rather — as the essential information (see below) — the time point at which the photosensitizer is largely photobleached. The method is, however, similar to the implicit dosimetry model [8] in that it employs the photobleaching kinetics for early treatment monitoring. The relative fluorescence method, however, relies on continuously monitoring the ratio of the detected PpIX fluorescence to the fluorescence detected at an earlier time point during therapeutic irradiation. We show by means of theoretical modelling of the diffuse light distribution of excitation and fluorescence light, that this ratio displays a unique connection to the time point at which the photosensitizer midway between therapeutic light sources is largely (e.g. to $1/e$ of the initial concentration) photobleached. As the fluence rate of the excitation light is expected to be minimal midway between the light sources, photobleaching is expected to be slowest at this position, too. Therefore, if the photosensitizer is largely consumed at this position, it is assumed, that the photosensitizer is even more consumed at all other locations. Due to the high tumour selectivity of the PpIX-accumulation, there is little to no risk in using very high irradiation as described in Johansson et al. [1]. Therefore, for real-time treatment supervision, it is essential to gather information about the progress of photobleaching distant from the irradiation fibres, which can be achieved by the relative fluorescence method. It can be assumed that the photosensitizer is even more consumed closer to the irradiation fibres.

The approach proposed in this study relies on an interstitial set-up, resembling the clinical setting where the same optical fibres are employed for both therapeutic light delivery and dosimetric measurements. Hence, the fluorescence measurements constitute no additional invasiveness or risk to the patient. The validity of the relative fluorescence method is investigated for varying tissue optical properties, photobleaching rates, initial photosensitizer concentration and inter-fibre separations. The relative fluorescence method might be employed to adjust total irradiation times to largely photobleach the photosensitizer present within the target volume without introducing excessively long treatment duration.

Materials and methods

The local fluence rate, Φ, was modelled by solving the steady-state diffusion equation, Eq. (1), via the Finite Element Method (FEM, Comsol Multiphysics GmbH, Göttingen Germany).

$$-\nabla \cdot [D\nabla\Phi(r,t)] + \mu_a\Phi(r,t) = S(r,t) \quad (1)$$

Here, the diffusion coefficient $D = [3\ (\mu_a + \mu_s')]^{-1}$ and μ_a and μ_s' are the wavelength-dependent absorption and reduced scattering coefficients, respectively. Eq. (2) was employed to describe the PpIX distribution and photodegradation, $C(r,t)$, during irradiation at 635 nm.

$$C(r,t) = C(t=0)e^{-\beta\Phi_{635\,\mathrm{nm}}(r)t} \quad (2)$$

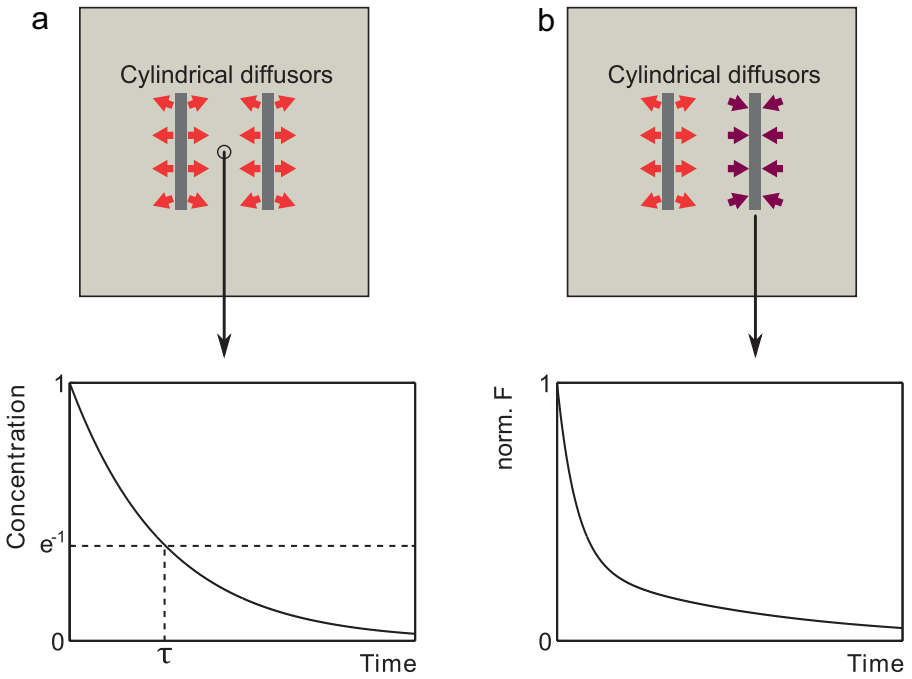

Figure 1 (a) Simulations' therapy mode. The spatially dependent concentration decay of the photosensitizer under irradiation at 635 nm is simulated. At the position r_c the time τ, at which the photosensitizer concentration drops below $1/e$ is evaluated. (b) Simulations' measurement mode. Only one diffusor is used as an excitation light source, the other one as detector. The evaluation of the fluorescent light at 700 nm incident on the non-emitting diffusor yields the photobleaching kinetics $F(t)$.

Here, $\Phi_{635\,nm}(r)$ is the time-independent light distribution at 635 nm as obtained from Eq. (1), $C(r,t)$ is the molar PpIX concentration and $\beta = 5\,mm^2/J$ is a fit parameter obtained from experimental measurements of the intrinsic PpIX photobleaching in brain tumours [20]. Following the simulation of $\Phi_{635\,nm}(r)$ and $C(r,t)$, Eq. (1) was employed to model the distribution of the 700-nm fluorescence, $\Phi_{700\,nm}(r,t)$, with the source term described by Eq. (3). The extinction coefficient of PpIX at 635 nm, ε_{PpIX}, was $600\,M^{-1}\,mm^{-1}$ [21] and the fluorescence yield, γ, was arbitrarily set to 1.

$$S(r,t) = \Phi_{635\,nm}(r)\varepsilon_{PpIX}\gamma C(r,t) \quad (3)$$

In the FEM solver, a cube with 10 cm side length was used to model the ''infinitely'' large tissue block with spatially independent μ_a, μ_s' and initial PpIX concentration, $C(t=0)$. The influence of photosensitizer on the light distribution, e.g. self-shielding [22], was disregarded due to the low extinction coefficient at 635 nm (μ_a(PpIX) $\leq 0.0014\,mm^{-1}$ at 635 nm with $C(t=0) = 1\,\mu M$) compared to overall absorption levels in the tissue-simulating situation. Simulations were performed for $\mu_a = 0.015$–$0.2\,mm^{-1}$ and $\mu_s' = 0.5$–$4.0\,mm^{-1}$. Two 20 mm long, 1.6-mm diameter cylindrical diffusors were implemented 10 mm apart. Both diffusors were assumed non-absorbing but with a reduced scattering coefficient equal to that of the surrounding tissue. The mesh of the FEM solver consisted of approximately 22,000 elements and was more detailed closer to the diffusors. Two settings were simulated:

(1) Therapy mode and simulation of $\Phi_{635\,nm}(r)$ and $C(r,t)$: the time-independent source term, $S(r)$, consisted of the two cylindrical diffusors with 25, 50 or 100 mW/cm output power each at 635 nm. Following this steady-state simulation, the time and spatially dependent PpIX concentration was modelled by Eq. (2) for $t = 0$–3600 s. In particular, the 635-nm fluence rate midway between the cylindrical diffusors, i.e. at the spatial position r_c, was employed to calculate the time τ according to Eq. (2) at which $C(r_c,\tau) = C(r_c,t=0) \times e^{-1}$. Fig. 1a shows a sketch of the therapy mode with evaluation of the photosensitizer's concentration decay and determination of τ.

(2) Measurement mode and simulation of $\Phi_{700\,nm}(r,t)$: the time-independent source term, $S(r)$, consisted of only one of the cylindrical diffusors with 25, 50 or 100 mW/cm output power at 635 nm. The obtained fluence rate at 635 nm and the PpIX distribution as calculated in therapy mode were used to simulate the 700-nm fluorescence for $t = 0$–3600 s by solving Eq. (1) with $S(r,t)$ according to Eq. (3). Here, $\mu_a(700\,nm) = 0.95 \times \mu_a(635\,nm)$ and $\mu_s'(700\,nm) = 0.80 \times \mu_s'(635\,nm)$. The 700-nm fluorescence incident at the surface of the second, non-emitting cylindrical diffusor was used to quantify the photobleaching kinetics. Fig. 1b shows a sketch of the measurement mode and the evaluation of the photobleaching kinetics.

Monte Carlo simulations (TracePro® 5.0, Lambda Research Corporation) with the same simulated source and detector geometry were performed for a selection from the same range of optical properties, especially for high absorption and low scattering coefficients, and compared to photobleaching kinetics simulated using diffusion theory.

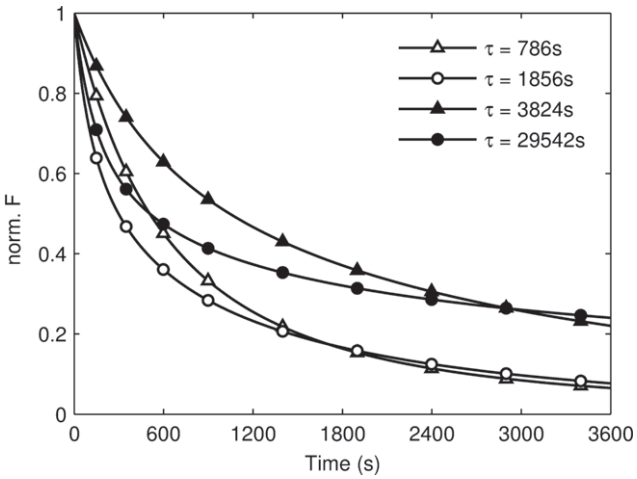

Figure 2 The normalized fluorescence for four sets of optical properties illustrating the concept of the relative fluorescence dosimetry model. Irradiation at 25 mW/cm via two 20-mm cylindrical diffusors with 10 mm separation was simulated. One of the diffusors, in off mode, was employed for detection at various time points during the simulated treatment. A low absorption coefficient leads to a more pronounced photobleaching as $t \to \infty$. For a given absorption level, a higher reduced scattering coefficient causes a higher initial photobleaching rate. △: $\mu_a = 0.06\,\mathrm{mm}^{-1}$ and $\mu_s' = 0.5\,\mathrm{mm}^{-1}$, ○: $\mu_a = 0.06\,\mathrm{mm}^{-1}$ and $\mu_s' = 4.0\,\mathrm{mm}^{-1}$, ▲: $\mu_a = 0.20\,\mathrm{mm}^{-1}$ and $\mu_s' = 0.5\,\mathrm{mm}^{-1}$, ●: $\mu_a = 0.20\,\mathrm{mm}^{-1}$ and $\mu_s' = 4.0\,\mathrm{mm}^{-1}$.

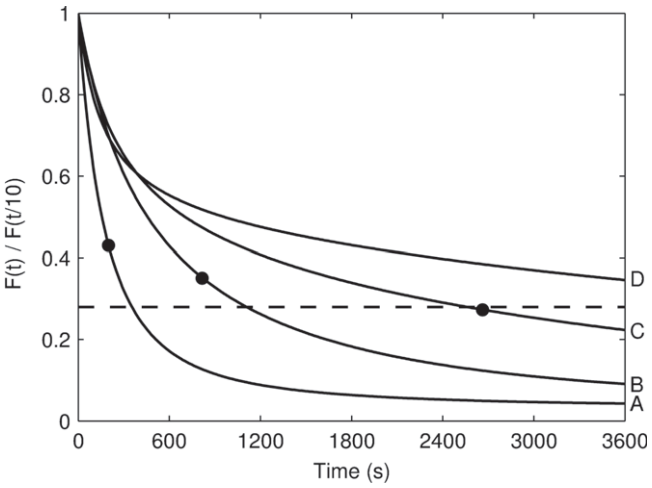

Figure 3 The ratio $R(t)$ with $\rho = 10$ according to Eq. (4) for simulations with different optical parameters (for reasons of clarity with different optical parameters compared to Fig. 2). Irradiation at 25 mW/cm via two 20-mm cylindrical diffusors with 10 mm separation was simulated. Dots (●) denote τ_{real}, the time points, at which the photosensitizer is bleached to $1/e$ midway between the cylindrical diffusors. The dashed line shows a threshold arbitrarily set to 0.28. Points of intersection yield $\tau_{threshold}$, a prediction of τ from photobleaching kinetics. A: $\mu_a = 0.015\,\mathrm{mm}^{-1}$, $\mu_s' = 2.0\,\mathrm{mm}^{-1}$, $\tau_{real} = 199$ s, $\tau_{threshold} = 360$ s; B: $\mu_a = 0.06\,\mathrm{mm}^{-1}$, $\mu_s' = 1.0\,\mathrm{mm}^{-1}$, $\tau_{real} = 816$ s, $\tau_{threshold} = 1110$ s; C: $\mu_a = 0.10\,\mathrm{mm}^{-1}$, $\mu_s' = 1.0\,\mathrm{mm}^{-1}$, $\tau_{real} = 2662$ s, $\tau_{threshold} = 2560$ s; D: $\mu_a = 0.10\,\mathrm{mm}^{-1}$, $\mu_s' = 2.0\,\mathrm{mm}^{-1}$, $\tau_{real} = 5858$ s (outside simulated time span), $\tau_{threshold} > 3600$ s (no point of intersection).

The overall relative residual was less than 15%, confirming the validity of the simulations using diffusion theory.

Results

Fig. 2 shows the modelled photobleaching induced by irradiation via both cylindrical diffusors and detected by one of the diffusors (switched off, i.e. not employed as source, during simulated detection) for four sets of optical properties. The fluorescence decay curves have been normalized to their respective initial level. The time points τ, at which the photosensitizer is bleached to $1/e$ midway between the cylindrical diffusors, are also indicated. By simply monitoring the fluorescence decay, possibly wrong predictions for τ might be made: an observed fast fluorescence decay (for example, in Fig. 2: open circles compared to open triangles) does not necessarily imply fast bleaching at the critical location midway between the irradiation fibres (open circles: $\tau = 1856$ s, open triangles: $\tau = 786$ s). But we observed that the progression of the ratio

$$R(t) = \frac{F(t)}{F(t/\rho)} \tag{4}$$

where $\rho = \text{const.} > 1$ and thus t/ρ denotes an early and t a later time point, is connected to the photobleaching efficacy within the target volume and correlated with τ. This observation and the temporal shape of the photobleaching kinetics in Fig. 2 can be explained by the following argumentation: As the fluence rate near the sources is dominated by scattering, and the fluence rate is correlated with bleaching according to Eq. (2), the photobleaching kinetics is dominated by scattering at early time points: High scattering yields fast bleaching in the beginning (circles), low scattering the opposite (triangles). At late time points the detected fluorescence comes from regions distant from the source fibres. For these longer photon paths, both absorption and reduced scattering coefficient determine the induced and detected fluorescence intensity and hence determine whether photosensitizer within distant regions can actually be photobleached. Therefore, most complete bleaching distant from the sources is achieved, when combining a low reduced scattering coefficient, responsible for slow photobleaching kinetics at early time points, and a low absorption coefficient, resulting in a most complete decay of the photobleaching kinetics at late time points (open triangles). As a consequence, the ratio in Eq. (4) can be used to determine the speed of photobleaching at locations distant from the sources.

In Fig. 3, the concept is demonstrated, showing $R(t)$ for $\rho = 10$ for simulations employing four different sets of optical properties. τ_{real} is indicated as well as $\tau_{threshold}$, a prediction of τ, that was determined by the time point, when $R(t)$ drops below a threshold of 0.28.

Fig. 4 shows the correlation of $\tau_{threshold}$ with τ_{real}, using $R(t)$ with $\rho = 10$ and a threshold of 0.28. Simulation results for a large range of optical properties, $\mu_a = 0.015$–$0.2\,\mathrm{mm}^{-1}$ and $\mu_s' = 0.5$–$4.0\,\mathrm{mm}^{-1}$ (including the parameters used to calculate Figs. 2 and 3), are shown as well as different output powers, 25, 50 or 100 mW/cm, and varying inter-fibre

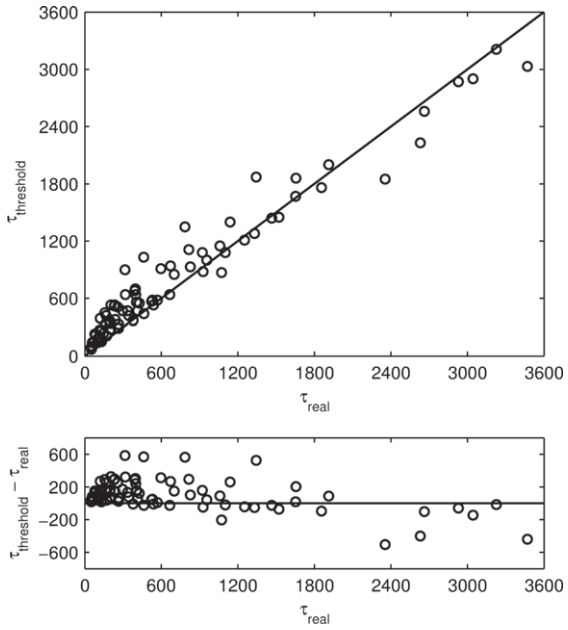

Figure 4 In the upper panel, $\tau_{threshold}$ vs. τ_{real} is shown for different sets of optical properties, $\mu_a = 0.015—0.2\,mm^{-1}$ and $\mu_s' = 0.5—4.0\,mm^{-1}$, different output powers, 25, 50 and 100 mW/cm, and varying inter-fibre separations, i.e. ±2 mm. The dashed line shows perfect agreement between $\tau_{threshold}$ and τ_{real}. In the lower panel, the residual, $\tau_{threshold}—\tau_{real}$, is shown. 13 cases with $\tau_{real} > 3600$ s were correctly identified with $\tau_{threshold} > 3600$ s, one case with $\tau_{real} > 3600$ s was incorrectly identified as $\tau_{threshold} < 3600$ s.

separations, i.e. 10 ± 2 mm. For 14 simulations, $\tau_{real} > 3600$ s, of which 13 were identified correctly by $\tau_{threshold} > 3600$ s, and one false positive ($\mu_a = 0.20\,mm^{-1}$, $\mu_s' = 4.0\,mm^{-1}$, output power 50 mW/cm, fibre separation 8 mm). The residual $\tau_{threshold}—\tau_{real}$ was ±600 s. Varying the initial photosensitizer concentration or bleaching rate β cannot be discriminated from changing fibre output power in the simulations and therefore did not alter agreement between $\tau_{threshold}$ and τ_{real}. $\rho = 10$ was chosen, because for a too low $\rho \to 1$, the ratio $R(t) \to 1$, and $R(t)$ for different optical parameters cannot be easily distinguished. If ρ is too high, $F(t < 1\,s)$ must be observed even for late time points during treatment, which seems impossible in the clinical setting. The threshold needs to be calibrated accordingly. As Fig. 4 shows, by continuous monitoring the relative fluorescence intensity, it is possible to predict the time point at which the photosensitizer is photobleached to $1/e$ of its initial level midway between the therapeutic light sources. This possibility offers the potential to shorten total treatment times in situations where light distribution and photobleaching result in a rapid degradation of the photosensitizer within the target tissue, or to identify situations, where unfavourable optical properties lead to an excessive irradiation time, that would be necessary to fully bleach the photosensitizer.

Discussion

Interstitial photodynamic therapy (iPDT) is being investigated for the treatment of high-grade human brain malignancies. It has previously been observed that oral ALA-administration leads to highly tumour-selective PpIX accumulation. However, absolute PpIX concentrations are highly heterogeneous and patient-specific [3]. This observation implies the need for and usefulness of *in vivo* monitoring of PpIX fluorescence intensity and photobleaching kinetics as tools for real-time treatment monitoring during brain-iPDT. Due to the good tumour-selective PpIX-distribution, it should be possible to relax the requirement on an accurate light dosimetry and to apply high fluence to completely consume the photosensitizer in the target volume as outlined by Johansson et al. [1]. Here, we propose a dosimetric approach, referred to as the relative fluorescence method that employs continuously monitoring the ratio of the detected 700-nm fluorescence to the fluorescence detected at an early time point during therapeutic irradiation. This ratio is related to the time point at which the photosensitizer is photodegraded to $1/e$ of its initial level within the inter-fibre spacing. These simple fluorescence measurements can be employed to adjust the therapeutic irradiation so as to fully consume the photosensitizer within the target volume without introducing excessive treatment duration. Via simulations of the diffuse light, we could show that the relative fluorescence method works for a large range of optical properties and for the set-up employed in the clinical setting [2]. Additionally, simulations indicated the validity of our approach for varying bleaching rates, inter-fibre distances and photosensitizer concentrations. The ability to predict τ, i.e. the time point at which the photosensitizer has been reduced to $1/e$ of its initial level midway between therapeutic light sources, with an accuracy of ±600 s constitutes an improvement in relation to the current clinical protocol where a standardized irradiation time of 3600 s is employed. For the clinical relevance, it is interesting to know whether the natural variation of the tissue optical properties of human malignant brain tissue induces such variations in τ that patient-individualized irradiation times are required. We have previously observed significant variations of the optical properties of *in vivo* human brain tissues [23], where, for example, the effective attenuation coefficient, μ_{eff}, was $0.84 \pm 0.35\,mm^{-1}$. In our current work, simulations have shown that τ depends on the optical properties and at high scattering levels τ varies linearly with μ_a. A patient-individualized dosimetric concept, possibly relying on fluorescence-based monitoring, with adaptation of irradiation times during brain-iPDT is thus of clinical interest. The relative fluorescence method also provides the possibility to identify cases where the optical properties hinder sufficient light penetration and an effective PDT. Such a case is displayed in Fig. 2 for the highest absorption and reduced scattering coefficients, yielding an un-realizable $\tau > 8$ h. Hence, possible non-responders might be identified at an early stage and referred to repeated PDT or alternative treatment options.

The herein proposed relative fluorescence method is related to the implicit dosimetry concept proposed by Wilson et al. [8] as a rapid and efficient photobleaching implies a low fluorescence ratio, $R(t)$. In agreement with our approach, previous studies have also employed the photobleaching degree for determining PDT efficacy. For example, Vollet-Filho et al. observed a correlation between the photodegradation and the depth of necrosis in rat liver following

superficial irradiation and fluorescence detection [24]. Farrell et al. were able to predict the depth of photobleaching for the case of pencil beam irradiation via spatially resolved fluorescence measurements at the air − phantom interface [25]. The validity of that dosimetry model could be shown for varying optical properties and for non-single exponential intrinsic photobleaching kinetics but not for arbitrary initial photosensitizer concentration. In contrast to these studies, we have investigated the interstitial irradiation and detection geometry as clinically employed during brain-iPDT. Furthermore, a slightly different end-point was attempted via the use of the time point at which PpIX has bleached away completely in the inter-fibre volume instead of trying to correlate fluorescence decay to depth of PDT damage. In contrast to the dose model proposed by Farrell et al. [25], our simulations showed that the relative fluorescence method worked for arbitrary initial photosensitizer concentration. As PpIX levels are known to display pronounced inter-tumoural variations [3] and the PpIX accumulation cannot easily be adjusted shortly prior to therapy, different initial photosensitizer levels are to expect. The relative fluorescence method constitutes a more realistic approach as it is applicable for varying $C(r,t=0)$. On the other hand, a sufficient PpIX concentration is crucial for successful PDT, but it cannot be assessed by the relative fluorescence method. Therefore, it must be measured separately to ensure sufficient PpIX accumulation. This measurement could be done during a pre PDT biopsy with preceding ALA administration: either absolute fluorescence intensity could be measured *in vivo* by a fibre probe or *ex vivo* using an extraction method or fluorescence measurements. Still, the influence of spatially dependent PpIX distributions [26,27] needs to be further investigated.

The intrinsic photobleaching kinetics is difficult to assess and remains unknown for most photosensitizers. First-order photobleaching kinetics has been employed to describe the observed photosensitizer decay [25,28]. However, as the detected fluorescence intensity is affected by the tissue optical properties [29,30], the excitation − detection geometry [31], the appearance of photodegradable photoproducts and photosensitizer re-localisation [32], the fluorescence signal detected during PDT most often does not follow a single exponential decay. Other models employ the second-order photosensitizer decay under the assumption of constant, non-limiting oxygen supply [33], being oxygen or irradiance dependent [18,34], or rely on explicitly solving the rate equations describing the light-induced energy transfer, photobleaching, oxygen diffusion and singlet oxygen production [11—13]. Here, we did not intend to model these biological processes in detail, but rather focus on the effects of unknown patient-specific optical properties. The fluorescence ratio $R(t)$, Eq. (4), is connected to the optical properties, that influence the time point τ, at which the photosensitizer is largely photobleached distant from the source fibres. This connection still exists even if we assume β to be irradiance or oxygen dependent. In this case, we expect it to be necessary to define the threshold value accordingly, compare Fig. 3. However, if the irradiance dependence of β is patient-specific or if unknown spatial inhomogeneities in β exist, it might be difficult to define a reliable threshold value. *In vivo* studies are warranted to confirm the proposed dosimetric concept in a realistic biological surrounding. Currently, we are able to monitor PpIX photobleaching kinetics during human brain-iPDT without any extra invasiveness or risk to the patient. Future work will elucidate whether fitting *in vivo* data to simulations can be employed to determine the intrinsic photobleaching kinetics in malignant brain tissue. The possibly time-, oxygen- or irradiance-dependent intrinsic photobleaching kinetics and the spatially varying photosensitizer distribution present the major challenges in implementing the proposed dosimetry model in the clinical setting.

In summary, we have proposed a dosimetric approach for iPDT where the photobleaching kinetics is employed to assess the time point at which the photosensitizer within the target volume is completely photobleached. This dosimetry method, referred to as the relative fluorescence method, might hence be employed to adjust total irradiation times to the patient-specific photosensitizer level and photobleaching kinetics. The dose metric has been shown to be independent of tissue optical properties, intrinsic photobleaching rate, initial photosensitizer level and inter-fibre spacing. The measurements required for the relative fluorescence method are easily implemented into our clinical protocol for brain-iPDT and introduce no additional invasiveness or risk to the patient.

Acknowledgements

This work was supported by the German Ministry of Education and Research (project Neurotax, grant 13N10172) and by Photonamic GmbH (Wedel, Germany). A. Johansson gratefully acknowledges the Alexander von Humboldt Foundation for its financial support.

References

[1] Johansson A, Kreth FW, Stummer W, Stepp H. Interstitial photodynamic therapy of brain tumors. IEEE J Sel Topics in Quantum Electron 2010;16(4):841—53.
[2] Beck TJ, Kreth FW, Beyer W, et al. Interstitial photodynamic therapy of nonresectable malignant glioma recurrences using 5-aminolevulinic acid induced protoporphyrin IX. Lasers Surg Med 2007;39(5):386—93.
[3] Johansson A, Palte G, Schnell O, Herms J, Stepp H. 5-Aminolaevulinic acid-induced protoporphyrin IX levels in tissue of human malignant brain tumours. Photochem Photobiol 2010;86(6):1373—8.
[4] Stummer W, Beck T, Beyer W, et al. Long-sustaining response in a patient with non-resectable, distant recurrence of glioblastoma multiforme treated by interstitial photodynamic therapy using 5-ALA: case report. J Neurooncol 2008;87(1):103—9.
[5] Castano AP, Mroz P, Hamblin MR. Photodynamic therapy and anti-tumour immunity. Nat Rev Cancer 2006;6(7):535—45.
[6] Fingar VH. Vascular effects of photodynamic therapy. J Clin Laser Med Surg 1996;14(5):323—8.
[7] Zhu TC, Finlay JC, Hahn SM. Determination of the distribution of light, optical properties, drug concentration, and tissue oxygenation in-vivo in human prostate during motexafin lutetium-mediated photodynamic therapy. J Photochem Photobiol B 2005;79(3):231—41.
[8] Wilson BC, Patterson MS, Lilge L. Implicit and explicit dosimetry in photodynamic therapy. Lasers Med Sci 1997;12:182—99.

[9] Weersink RA, Bogaards A, Gertner M, et al. Techniques for delivery and monitoring of TOOKAD (WST09)-mediated photodynamic therapy of the prostate: clinical experience and practicalities. J Photochem Photobiol B 2005;79(3):211—22.
[10] Johansson A, Axelsson J, Andersson-Engels S, Swartling J. Realtime light dosimetry software tools for interstitial photodynamic therapy of the human prostate. Med Phys 2007;34(11):4309—21.
[11] Finlay JC, Mitra S, Patterson MS, Foster TH. Photobleaching kinetics of Photofrin in vivo and in multicell tumour spheroids indicate two simultaneous bleaching mechanisms. Phys Med Biol 2004;49(21):4837—60.
[12] Wang KK, Mitra S, Foster TH. A comprehensive mathematical model of microscopic dose deposition in photodynamic therapy. Med Phys 2007;34(1):282—93.
[13] Wang KK, Finlay JC, Busch TM, Hahn SM, Zhu TC. Explicit dosimetry for photodynamic therapy: macroscopic singlet oxygen modeling. J Biophotonics 2010;3(5—6):304—18.
[14] Jarvi MT, Niedre MJ, Patterson MS, Wilson BC. Singlet oxygen luminescence dosimetry (SOLD) for photodynamic therapy: current status, challenges and future prospects. Photochem Photobiol 2006;82(5):1198—210.
[15] Dysart JS, Singh G, Patterson MS. Calculation of singlet oxygen dose from photosensitizer fluorescence and photobleaching during mTHPC photodynamic therapy of MLL cells. Photochem Photobiol 2005;81(1):196—205.
[16] Robinson DJ, de Bruijn HS, van der Veen N, Stringer MR, Brown SB, Star WM. Protoporphyrin IX fluorescence photobleaching during ALA-mediated photodynamic therapy of UVB-induced tumors in hairless mouse skin. Photochem Photobiol 1999;69(1):61—70.
[17] Ericson MB, Sandberg C, Stenquist B, et al. Photodynamic therapy of actinic keratosis at varying fluence rates: assessment of photobleaching, pain and primary clinical outcome. Br J Dermatol 2004;151(6):1204—12.
[18] Cottrell WJ, Paquette AD, Keymel KR, Foster TH, Oseroff AR. Irradiance-dependent photobleaching and pain in delta-aminolevulinic acid-photodynamic therapy of superficial basal cell carcinomas. Clin Cancer Res 2008;14(14):4475—83.
[19] Sheng C, Hoopes PJ, Hasan T, Pogue BW. Photobleaching-based dosimetry predicts deposited dose in ALA-PpIX PDT of rodent esophagus. Photochem Photobiol 2007;83(3):738—48.
[20] Stepp H, Beck T, Pongratz T, et al. ALA and malignant glioma: fluorescence-guided resection and photodynamic treatment. J Environ Pathol Toxicol Oncol 2007;26(2):157—64.
[21] Lavi A, Weitman H, Holmes RT, Smith KM, Ehrenberg B. The depth of porphyrin in a membrane and the membrane's physical properties affect the photosensitizing efficiency. Biophys J 2002;82(4):2101—10.
[22] Patterson MS, Wilson BC. A theoretical study of the influence of sensitizer photobleaching on depth of necrosis in photodynamic therapy. Proc SPIE 1994;2133:208—19.
[23] Beck TJ, Beyer W, Pongratz T, et al. Clinical determination of tissue optical properties in vivo by spatially resolved reflectance measurements. Proc SPIE 2003;5138:96—105.
[24] Vollet-Filho JD, Menez PFC, Moriyama LT, et al. Possibility for a full optical determination of photodynamic therapy outcome. J Appl Phys 2009;105:102038.
[25] Farrell TJ, Hawkes RP, Patterson MS, Wilson BC. Modeling of photosensitizer fluorescence emission and photobleaching for photodynamic therapy dosimetry. Appl Opt 1998;37(31):7168—83.
[26] Eleouet S, Rousset N, Carre J, et al. Heterogeneity of delta-aminolevulinic acid-induced protoporphyrin IX fluorescence in human glioma cells and leukemic lymphocytes. Neurol Res 2000;22(4):361—8.
[27] Madsen SJ, Angell-Petersen E, Spetalen S, Carper SW, Ziegler SA, Hirschberg H. Photodynamic therapy of newly implanted glioma cells in the rat brain. Lasers Surg Med 2006;38(5):540—8.
[28] Jacques SL, Joseph R, Gofstein G. How photobleaching affects dosimetry and fluorescence monitoring of PDT in turbid media. Proc SPIE 1993;1881:168—79.
[29] Jongen AJ, Sterenborg HJ. Mathematical description of photobleaching in vivo describing the influence of tissue optics on measured fluorescence signals. Phys Med Biol 1997;42(9):1701—16.
[30] Müller MG, Georgakoudi I, Zhang Q, Wu J, Feld MS. Intrinsic fluorescence spectroscopy in turbid media: disentangling effects of scattering and absorption. Appl Opt 2001;40(25):4633—46.
[31] Jacques SL. Light distributions from point, line and plane sources for photochemical reactions and fluorescence in turbid biological tissues. Photochem Photobiol 1998;67(1):23—32.
[32] Moan J, Streckyte G, Bagdonas S, Bech O, Berg K. Photobleaching of protoporphyrin IX in cells incubated with 5-aminolevulinic acid. Int J Cancer 1997;70(1):90—7.
[33] Forrer M, Glanzmann T, Mizeret J, et al. Fluorescence excitation and emission spectra of ALA induced protoporphyrin IX in normal and tumoral tissue of the human bladder. In: Cubeddu R, Marchesini R, Mordon SR, Svanberg K, Rinneberg HH, Wagnières G, editors. Optical biopsy and fluorescence spectroscopy and imaging. Lille, France: Proc. SPIE; 1994. p. 84—8.
[34] Wang KK, Cottrell WJ, Mitra S, Oseroff AR, Foster TH. Simulations of measured photobleaching kinetics in human basal cell carcinomas suggest blood flow reductions during ALA-PDT. Lasers Surg Med 2009;41(9):686—96.

DANKSAGUNG

Hiermit danke ich allen, die mich bei meiner Doktorarbeit mit Rat und Tat unterstützt haben.

Ich danke meinem Doktorvater, Prof. Michael Vogeser, für seine tatkräftige Unterstützung bei Probenselektion, Durchführung der klinischen Messungen und Verfassen der Manuskripte, sowie Klärung medizinischer Fragen, die ansonsten unbeantwortet geblieben wären.

Prof. Gary M. Brittenham danke ich für die vielfachen motivierenden Gespräche und für seine Unterstützung beim Verfassen der Manuskripte. Außerdem ist er mit der Problemstellung der nichtinvasiven Quantifizierung von Zink-Protoporphyrin IX an uns herangetreten und unter anderem seinem Einsatz ist die Projektförderung zu verdanken.

Für die finanzielle Unterstützung während eines Teils meiner Doktorarbeit danke ich dem Nestlé Research Center, Nestec Ltd., besonders Dr. Nadia Khaled. Dank ihrer Begeisterung für das Projekt konnte trotz einiger Hürden die Geräteentwicklung von der Idee bis hin zum klinisch erprobten Prototyp erfolgen.

Besonderer Dank gilt Dr. Herbert Stepp, der trotz seiner vielfachen Verpflichtungen immer genügend Zeit gefunden hat, Fortschritte zu diskutieren, Verbesserungsvorschläge zu machen oder Manuskripte zu lesen. Besonders hervorheben möchte ich seinen unermüdlichen Kampf mit allen formalen Hürden, die ein Projekt mit klinischer Studie mit sich bringt und die er erfolgreich von mir fernzuhalten wusste. Ohne ihn wäre das Projekt nicht durchführbar gewesen.

Weiterhin danke ich unserem Laborleiter Dr. Ronald Sroka, der immer eine offene Tür hatte und mich fortwährend in meiner Arbeit bestärkte, und Dr. Wolfgang Beyer für Rat und Tat insbesondere bei allen Fragen zu Computersimulationen. Außerdem danke ich allen anderen Mitarbeitern im Laser-Forschungslabor für die angenehme Arbeitsatmosphäre, die es auch erlaubt hat, neben der Arbeit ein wenig rechts und links zu schauen, vor allem Frau Gesa Kniebühler, die mit mir jahrelang das Büro geteilt und mich immer wieder motiviert hat, und Frau Katharina Thomsen, die mich bei allen Fragen bzgl. Optik und Abläufen im Labor tatkräftig unterstützt hat.

Zu guter Letzt danke ich meiner Familie, vor allem meiner Frau Andrea, dass sie mir in den vergangenen Jahren geduldig zur Seite standen.

In memoriam Dr. Ann Johansson, von der ich viel zu kurz lernen durfte.

Eidesstattliche Versicherung

Hennig, Georg

Name, Vorname

Ich erkläre hiermit an Eides statt,

dass ich die vorliegende Dissertation mit dem Thema

Fluoreszenz von Porphyrinen zur klinischen Anwendung in Diagnostik und Therapie

selbständig verfasst, mich außer der angegebenen keiner weiteren Hilfsmittel bedient und alle Erkenntnisse, die aus dem Schrifttum ganz oder annähernd übernommen sind, als solche kenntlich gemacht und nach ihrer Herkunft unter Bezeichnung der Fundstelle einzeln nachgewiesen habe.

Ich erkläre des Weiteren, dass die hier vorgelegte Dissertation nicht in gleicher oder in ähnlicher Form bei einer anderen Stelle zur Erlangung eines akademischen Grades eingereicht wurde.

München, 04.04.14

Ort, Datum

Unterschrift Doktorandin/Doktorand